論文 / 著書情報
Article / Book Information

題目(和文)	銀河合体系列に沿った近傍高光度赤外線銀河の分子ガスと星形成
Title(English)	Molecular Gas and Star Formation along the Merger Sequence in Local Luminous Infrared Galaxies
著者(和文)	山下拓時
Author(English)	Takuji Yamashita
出典(和文)	学位:博士（理学）, 学位授与機関:東京工業大学, 報告番号:甲第9706号, 授与年月日:2015年3月26日, 学位の種別:課程博士, 審査員:松原　英雄,河合　誠之,宗宮　健太郎,堂谷　忠靖,野村　英子,久野　成夫
Citation(English)	Degree:, Conferring organization: Tokyo Institute of Technology, Report number:甲第9706号, Conferred date:2015/3/26, Degree Type:Course doctor, Examiner:,,,,,
学位種別(和文)	博士論文
Type(English)	Doctoral Thesis

Tokyo Institute of Technology

Doctoral Thesis

Molecular Gas and Star Formation along the Merger Sequence in Luminous Infrared Galaxies

---

Takuji Yamashita

A thesis submitted in fulfilment of the requirements
for the degree of Doctor of Science

in the

Department of Physics

February 2015

Abstract

In this thesis, molecular gas and star formation in local Luminous Infrared Galaxies (LIRGs) are studied along the stage of a galaxy merger sequence. Most local LIRGs are starbursting and are involved with galaxy-galaxy interactions or mergers. The direct trigger and the evolution of the merger-driven starburst are not clear observationally, although there are several theoretical explanations. In order to reveal these issues, information of the molecular gas, which is traced by carbon monoxide emission (^{12}CO $J = 1 - 0$), of an unbiased LIRG sample is required. To this end, a survey of CO emission from 79 galaxies in 62 LIRG systems were conducted with the Nobeyama 45 m telescope, resulting in the largest CO dataset to date. A new method is presented to estimate the extent of CO gas in galaxies using combinations of single aperture telescopes. The CO extent is found to possibly decrease from the early stage to the late stage of the merger. The molecular gas mass in the central several kiloparsecs is constant throughout the merger sequence. This statistically supports a theoretically predicted scenario where global gas inflow towards the galaxy center is common in merging LIRGs. The inflowing gas may come from the outer disk. Along the merger sequence, the molecular gas mass and the star formation rate (SFR) of the merging LIRGs are found to be nearly constant. From the estimation that the gas depletion timescale of LIRGs is as short as 10^{7-8} yr, the merging LIRGs are short-lived luminous starburst phases on the merger sequence. At the late stage, LIRGs are coexistent with ULIRGs and have lower SFR than ULIRGs. This suggests that the LIRGs at the late stage are galaxies prior to or immediately after the short ULIRG phase. Merging LIRGs are located between normal spirals and ULIRGs on the Kennicutt-Schmidt relation. I propose an evolutionary sequence from the gas-rich spirals, LIRGs to ULIRGs and again back to LIRGs. The efficiencies of the star formation are found to be constant and as high as the starburst sequence throughout all merger stages, suggesting that the conversion from gas to stars is driven by a common relation regardless of merger stage.

Contents

List of Figures

List of Tables

Chapter 1

Introduction

1.1 Luminous Infrared Galaxies

1.1.1 Overview

The IRAS[1] satellite succeeded in the first all-sky survey in the infrared (IR) wavelength in 1983 and discovered numerous IR-luminous galaxies in the local universe ($z \lesssim 0.3$). Among them, Luminous Infrared Galaxies (LIRGs) are defined to be galaxies with IR luminosity $L_{\rm IR}(\lambda = 8 - 1000\mu{\rm m}) \geqslant 10^{11}\,L_{\odot}$ (see Sanders & Mirabel, 1996). In particular, the most luminous sub-sample ($L_{\rm IR} \geqslant 10^{12}\,L_{\odot}$) of LIRGs are called Ultraluminous Infrared Galaxies (ULIRGs). U/LIRGs powerfully radiate the bulk of their bolometric energy at the IR wavelength, which is due to the rich interstellar dust heated by UV radiation. Since the discovery of many U/LIRGs in the local universe by the IRAS survey, important questions have arisen for U/LIRGs: what is the source of their power?, what is the mechanism responsible for their extreme IR radiation? In the last two decades, attention from astronomers was drawn not so much to local LIRGs but local ULIRGs due to their extraordinary IR radiations. Recently, however, some researchers have begun to focus on local LIRGs.

The power sources in LIRGs were considered to be violent star formation activity (starburst or SB) and/or Active Galactic Nuclei (AGN). Recent studies of the energy sources in local LIRGs using large samples show that local LIRGs are generally starburst-dominated galaxies and have little contribution ($\lesssim 15\,\%$) to their IR luminosity from the AGNs (Petric et al. 2011 for $z < 0.088$; Alonso-Herrero et al. 2012a for $z < 0.018$). The AGN contribution increases with the IR luminosity to 35 % – 40 % in local ULIRGs (Veilleux et al., 2009). The number fraction of AGN in local LIRGs also increases with the IR luminosity from $\sim 10\,\%$ in LIRGs to ~ 35 – $60\,\%$ in ULIRGs (Veilleux et al., 1995; Alonso-Herrero et al., 2012a).

A significant number of local LIRGs and most ULIRGs show signs of galaxy-galaxy interactions or galaxy mergers. Interactions/mergers can induce nuclear starbursts by efficiently transporting gas towards galactic center(Barnes & Hernquist, 1996; Mihos & Hernquist, 1996). Therefore interactions/mergers may be causally related to starburst in local U/LIRGs. Most ULIRGs appear to be at the advanced stage of a merger (e.g., Murphy et al., 2001). On the other hand, LIRGs

[1]The Infrared Astronomical Satellite (Neugebauer et al., 1984).

in the local universe are observed at all stages of interactions/mergers including non-interacting galaxies (Haan et al., 2011; Petric et al., 2011; Stierwalt et al., 2013). This might imply, therefore, an evolutionary connection from LIRGs to ULIRGs on the merger sequence, which shows the enhancement of the IR luminosity at late stages of a merger. However, the evolution of local LIRGs along the merger sequence from the beginning to the end of a merger is observationally unrevealed.

Taken together, local LIRGs are mostly starbursting and found at all stages of a merger. Therefore, LIRGs are the key sample to address and answer the outstanding issues regarding the star formation on merger events. A large, comprehensive study by using complete sample of local LIRGs is required to infer on the general characteristics of local LIRGs.

1.1.2 GOALS: The Great Observatories All-sky LIRG Survey

The Great Observatories All-sky LIRG Survey (GOALS[2], Armus et al. 2009) is a project to comprehensively study the issues concerned with the local LIRGs. The GOALS targets an unbiased sample of 202 LIRGs in the local universe ($z < 0.088$), which is composed of 180 LIRGs and 22 ULIRGs. The sample comprise a complete sub-set of the IRAS Revised Bright Galaxy Sample (RBGS, Sanders et al., 2003), which is a flux-limited sample of all 629 extragalaxies with 60 μm flux densities above 5.24 Jy, and Galactic latitudes above five degree. The GOALS combines multi-wavelength data from Spitzer[3] (IR), Chandra[4] (X-ray), HST[5] (UV and optical), GALEX[6] (UV), AKARI[7] (IR), Herschel[8] (IR and sub-mm), and ground-based telescopes.

The GOALS sample covers the full range of the merger stages: first approach stage, post-first encounter stage, mid-stage and late stage, and also non-interactions. The nuclear spectra span various types in the optical emission line

[2]See also the website for the details, `http://goals.ipac.caltech.edu/`.
[3]The Spitzer Space Telescope (Gehrz et al., 2007).
[4]The Chandra X-ray Observatory.
[5]The Hubble Space Telescope.
[6]The Galaxy Evolution Explorer.
[7]AKARI Infrared Astronomy Satellite (Murakami et al., 2007).
[8]The Herschel Space Observatory (Pilbratt et al., 2010).

diagnostic diagram, type-1 AGN, type-2 AGN, LINER (low-ionization nuclear emission-line regions, see Ho 2008) and starburst. The source distance ranges from 18 Mpc ($z = 0.003$) to 400 Mpc ($z = 0.088$) with a median value of 94 Mpc ($z = 0.021$). The GOALS provide multi-wavelength dataset of local LIRGs with a variety of merger and nuclear activity and aim to provide intellect on the evolution and formation of local LIRGs. Now much of the imaging and spectroscopy data are available. The observations and catalogs provided by the GOALS project are tabulated in Table 1.1. Below I review the studies by the GOALS.

General Information

Armus et al. (2009) give an overview of GOALS and the sample, and demonstrated a multi-wavelength study of VV 340 which is a paired galaxy system composed of an IR-luminous galaxy with a buried AGN identified by Spitzer/IRS and Chandra and an UV-luminous star-forming galaxy. Taking advantage of the multi-wavelength surveys of the GOALS, U et al. (2012) presented the broad spectral energy distributions (SFDs) from X-ray to radio for 64 LIRGs. They also calculated and provided basic quantities including the total IR luminosity, the dust temperature, the dust mass, the stellar mass and the SFR.

Spitzer observations provided images from the near-IR (NRI) to far-IR (FIR), and mid-IR (MIR) spectra for the full GOALS sample. Inami et al. (2013) diagnosed the physical properties and chemical abundances using the MIR fine structure emission lines and starburst models. They estimated starburst ages of 1 Myr to 4.5 Myr and metallicities of $1 \lesssim Z\,[\mathrm{Z}_\odot] \lesssim 2$. Díaz-Santos et al. (2010, 2011) examined the extent of MIR features in the Spitzer/IRS spectra. They found three types of MIR distributions: one with extended star formation, one with high nuclear activity and quiescent star formation in the disk, and one with obscured AGN. While the MIR core size is on average 2.6 kpc, highly-luminous galaxies with $L_{\mathrm{IR}} > 10^{11.8}\,L_\odot$ have an unresolved core (< 1.5 kpc). The MIR extent is compact in galaxies at the final stage of merger or in galaxies with AGN. The MIR features of the core are very diverse and characterize local LIRGs, while the extra-nuclear region are similar to local star-forming galaxies and ULIRGs at $z \sim 2$.

Interaction and Merger

The optical and NIR observations conducted by HST towards more luminous LIRGs ($L_{\rm IR} \geqslant 10^{11.4}\,L_{\odot}$) provide detailed structural properties. Haan et al. (2011, 2013) addressed the formation and evolution of the nuclear structure with the H-band images. They found that $\sim 70\,\%$ of the sub-sample possess multiple nuclei and that the relics of nuclear starburst in 76 % of the sources are resolved. They also calculated the dynamical time until the nuclei merge, showing that the majority is either at the first passage of interaction, or at the final nuclear coalescence. Kim et al. (2013) decomposed the galactic structures into the disk, the bulge, elliptical-like property and the bar using I-band images. They showed that the disk+bulge system is the dominant structure in both LIRGs and ULIRGs. They also showed the mass ratio in the GOALS pair systems and that the most of the galaxies are major mergers. Howell et al. (2010) found that more luminous merging galaxies with high specific SFR (sSFR: ratio of SFR to stellar mass) are more heavily obscured by dust, and proposed an evolutionary picture of the transition from LIRGs to ULIRGs through major merger events. The merger stages of the GOALS LIRGs are morphologically classified and provided by Stierwalt et al. (2013) for the full sample using IRAC 3.6 μm images and also by Haan et al. (2011) for the limited sample using the HST images.

Sub-millimeter observations were conducted for two local LIRGs, NGC 0034 (a late-stage major merger, Xu et al., 2014) and NGC 1614 (a late-stage minor merger, Xu et al., 2015), in the GOALS project using ALMA[9]. For NGC 0034, the CO $J = 6{-}5$ emission line and 435 μm dust continuum emission were resolved. The morphology and kinematics of the CO and the dust emission suggest a compact rotating disk with high density gas ($\gtrsim 10^4\,M_{\odot}{\rm pc}^{-2}$) and a compact size ($r \lesssim 100\,{\rm pc}$), which is spatially consistent with the nuclear starburst. A circumnuclear ring in NGC 1614 was resolved in the CO $J = 6 - 5$ emission line. The ring has knots associated with star forming regions with a star formation density of $100\,M_{\odot}{\rm yr}^{-1}$ and a gas density of $10^4\,M_{\odot}{\rm pc}^{-2}$. They showed that the star forming regions in NGC 1614 on the scale of $\sim 100\,{\rm pc}$ strongly deviate from the standard Kennicutt-Schmidt law.

Medling et al. (2014) presented integral field spectroscopy with ground based telescopes for 17 LIRGs which are on-going mergers. They showed nuclear disks

[9]Atacama Large Millimeter/submillimeter Array

of gas and stars in almost all their merging LIRGs. The formation of nuclear disks may be common in gas-rich mergers.

AGN

Iwasawa et al. (2009, 2011) presented X-ray data observed with Chandra for 44 LIRGs with $L_{\rm IR} \geqslant 10^{11.73-12.57}\,L_{\odot}$. AGNs are found in 16 galaxies out of the total sample based on the hard X-ray color and the 6.4 keV Fe K line. They clearly detected a double AGN only in NGC 6240. The presence of the AGN in galaxies is also assessed using the MIR emission of [NeV], [OIV] and [NeII], the 6.2 μm polycyclic aromatic hydrocarbon (PAH) and the shape of the MIR continuum. The majority of the GOALS LIRGs are starburst-dominated galaxies (Petric et al., 2011), but the fraction of the starburst-dominated galaxies is declining as the merger progresses (Stierwalt et al., 2013).

Table 1.1: The GOALS observations and the published catalogs.

Facility	Wavelength	Method	Literature
Chandra	X-ray	Imaging/ Spectroscopy	Iwasawa et al. 2009, 2011
GALEX	UV	Imaging	Howell et al. 2010
Keck/OSIRIS	NIR	IFS	Medling et al. 2014
HST	optical	Imaging	Kim et al. 2013,
	NIR	Imaging	Haan et al. 2011, 2013
AKARI/IRC	MIR	Spectroscopy	Inami et al. in prep.
Spitzer/IRS	MIR	Spectroscopy	Díaz-Santos et al. 2010, 2011, Inami et al. 2013, Stierwalt et al. 2013, 2014,
Spitzer/IRAC, MIPS	MIR	Imaging	Mazzarela et al. in prep.
IRAS	MIR, FIR	Photometry	Sanders et al. 2003, Armus et al. 2009
Herschel	FIR, Sub-mm	Spectroscopy	Zhao et al. 2013, Díaz-Santos et al. 2013
(e)VLA	Radio	Imaging	Leroy et al. 2011, Vardoulaki et al. 2014
combined	X-ray to Radio	Photometry	U et al. 2012

1.2 Galaxy-galaxy Interaction and Merger

1.2.1 Overview

Galaxy-galaxy interaction and subsequent merger deform the morphology of galaxies, and, in some cases, promote the formation of stars, and reshape the galaxies. The interaction and merger, therefore, are the main drives due to which galaxies evolve and form. On the hierarchical cosmology model of galaxy formation, merger is a fundamental process to assemble the galaxy mass (Lacey & Cole, 1993). Half of the total stellar mass in local massive galaxies are estimated to be created through mergers at an epoch between $0.3 < z < 3.0$ (Ownsworth et al., 2014). In the frame of the cosmic star formation history, mergers between galaxies is one of the candidate factors regulating star formation evolution, although the contribution to the star formation is as low as a few 10 % at $z \sim 2$ (Kaviraj et al., 2013).

Morphology, star formation, dynamical timescale and remnants of mergers are depending on the total mass and the gas mass in colliding galaxies (Cox et al., 2008; Lotz et al., 2010b,a). Merger is often broken into two types from the mass ratio of two colliding galaxies: "major merger" is the collision between two galaxies with the comparable masses ($0.25-0.3 <$ massratio $< 3-4$), and "minor merger" is the collision between two galaxies with the large mass ratio (massratio $< 0.25-0.3$ or massratio $> 3-4$). Additionally based on the gas contents of the galaxies, merger is further classified into the "wet merger" for gas-rich galaxies and the "dry merger" for gas-poor galaxies.

The major merger of gas-rich spiral galaxies is generally believed to trigger the starburst in galaxies during the merger sequence. Local LIRGs and ULIRGs are mostly involved with interactions or mergers and have abundant molecular gas (e.g., Sanders et al., 1991; Solomon et al., 1997). Many numerical simulations of merging galaxies demonstrate that gas-rich major merger can become starbursting galaxies during the merger and can be observed as LIRGs or ULIRGs (Mihos & Hernquist, 1996; Barnes & Hernquist, 1996; Cox et al., 2006). Interactions and mergers are key processes on the evolution of LIRGs.

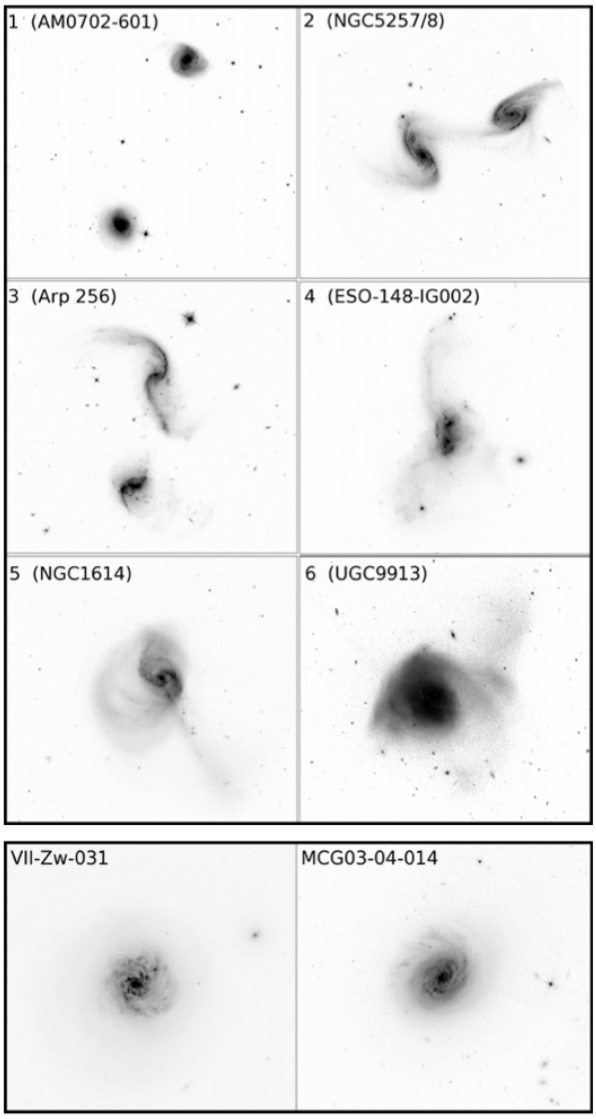

FIGURE 1.1: The stage classification of the merging galaxies. This figure is taken from Haan et al. (2011) who classify of the GOALS LIRGs with $L_{\rm IR} \geqslant 10^{11.4}\,L_{\odot}$ into six merger stages based on the morphologies in the HST images. Our classification is corresponding to stage 1 for the first approach stage, stage 2 and 3 for the early stage merger, stage 4 for the mid stage merger and stage 5 and 6 for the late stage merger, respectively.

1.2.2 Merger Sequence and Star Formation

Interactions and mergers dramatically change the structure of the interiors of galaxies over time. The stellar and gas disks deform, and the consequent star-forming activity also vary. For star formation in merging galaxies, gas plays an

important role. The gas is subject to dissipation of energy and angular momentum in contrast to stars which are collisionless. Gas which loses angular momentum is transported into the galactic center, commonly referred to as "gas inflow", and then centrally concentrates. The factors responsible for the gas inflow are mainly the gravitational torque from the companion galaxy and the non-axisymmetric potential produced by the distorted disk in the host galaxy. As a result, the gas fuels nuclear activities, the nuclear starburst and/or AGN (Mihos & Hernquist, 1996; Barnes & Hernquist, 1996).

The intensity of the induced starburst, i.e., the SFR, in merging galaxies varies along the merger sequence. Simulations predict that the maximum SFR emerges after the first encounter and during the final coalescence (Mihos & Hernquist, 1996; Cox et al., 2006, 2008). This star formation history during the merger processes depend on many parameters: the geometry and trajectory of collision, the relative mass, the inner structure and the gas distribution in each galaxies. Numerical simulations can predict how these parameters affect star formation in the galaxies. Galaxies in a retrograde orbit (the opposite directions of the angular momentum of the galaxy rotations) have elevated SFR at the final merger stage compared to the direct-collision mergers (Di Matteo et al., 2007). Major mergers efficiently enhance the relative SFR during the merger compared to minor mergers (Cox et al., 2008). The presence of a massive bulge delays the onset of the initial starburst compared to the bulgeless galaxies (Mihos & Hernquist, 1994, 1996; Cox et al., 2008). The initial density distribution of the gas controls the starburst efficiency (Cox et al., 2008). The starburst activity at the early stage might determine the amount of the available gas for star formation at the late stage, and consequently affect the intensity and the timing of the star formation at the late stage. Therefore star formation at the early stage is likely to govern the evolution from LIRGs phase to ULIRGs phase.

Numerical simulations succeed in reproducing the deformed morphologies and the peculiar features such as amorphous disks, tidal tails, bridge between galaxies, nearby companions, or double cores which are observed in merging galaxies (e.g., Surace, 1998; Privon et al., 2013). Based on the consistency of the distorted morphologies between the observation and the theory, the merging galaxies can be classified into four to six stages judged by the presence of the peculiar features or the separation between two nuclei (e.g., Stierwalt et al., 2013; Petric et al., 2011; Yuan et al., 2010). Here I separate mergers into four stages based on

the scheme by Surace (1998) and describe the characteristic properties at the each stage in the following sections. The HST images of galaxies at the each stage are shown in Figure 1.1.

1.2.2.1 First approach stage

The first approach stage is the earliest stage of interacting pairs which are approaching each other for the first encounter. The galaxies at this stage show no signature of tidal tails or bridges and still maintains an undisturbed disk. These galaxies are not found in the ULIRG sample and the QSO sample (Surace, 1998), but $\sim 20\,\%$ of the GOALS LIRG sample are at this stage (Stierwalt et al., 2013). This may mean the existence of a limit in the ultraluminous infrared luminosity or the SFR at the first approach stage (Surace, 1998). The experiments of numerical simulations of merging galaxies do not show enhancements in the SFR before the perigalactic passage (e.g., Di Matteo et al., 2007). These galaxies without interacting features in the GOALS LIRGs with $L_{\rm IR} \geqslant 10^{11.4}\,L_{\odot}$ tend to have a bulge with large luminosity, large radius, large Sersic index and small luminosity surface density of bulge compared to the LIRGs in on-going merger stages (Haan et al., 2011). This stage corresponds the stage 1 in Figure 1.1.

1.2.2.2 Early Stage Merger

("First contact stage" and early "Pre-merger stage")[10] After pericentric passage, galaxies show bridges connecting both galaxies and prominent tidal tails which are stretched along the direction of the other galaxy. Galaxies are affected by the strong gravitational torque from companion galaxy. The gas within the co-rotation radius is forced by the negative torque and then loses its angular momentum while the gas outside the co-rotation radius gains angular momentum. Moreover, the stellar components largely distort and stellar bar forms in the inner disk. The distorted stellar disk produces a non-axisymmetric potential which force the torque to the gas. Consequently, the gas in the disk inflows towards the galactic center while the outside gas is ejected from the galaxy and forms tidal features. This is the beginning of the first starburst. The intensity and timing of the maximum SFR depends on the initial conditions. The timescale of

[10]The original names given in Surace (1998) are referred in the parentheses.

the starburst during this stage is estimated to be $\sim$ 500 Myr for major mergers, which is relatively longer than at the final stage which is $\sim$ 300 Myr (Cox et al., 2008). Many GOALS LIRGs and some ULIRGs are located in this early stage merger with accompanying companions (Haan et al., 2011; Murphy et al., 2001; Dinh-V-Trung et al., 2001). The galaxies at this stage are also referred to as paired galaxies or galaxy pairs. This stage corresponds the stage 2 and 3 in Figure 1.1.

1.2.2.3 Mid Stage Merger

(late "Pre-merger stage")[10] At the mid stage, where galaxies have experienced the first close passage, return from the maximum separation and then head for the nuclear merger. The two nuclei are still identified, but within a common amorphous envelope. The galaxies show tidal tails and strongly distorted morphologies. The rapidly varying gravitational potential further prompts the gas inflow. In galaxies at this stage, irregular features concerned with star formation can be found, such as possible off-nuclear starburst found in the mid-stage merger II Zw 096 (Inami et al., 2010). Extended star-forming regions are found along the filament structure between two merging galaxies, IC 1623A and B (Iono et al., 2013). This stage corresponds the stage 4 in Figure 1.1.

1.2.2.4 Late Stage Merger

("Merger stage")[10] The two nuclei in two galaxies finally coalesce into one nucleus which is mostly obscured in the optical. The gravitational torques from the host galaxies are dominant against the gas, and most of the gas exists in the central regions at high density. In this stage, galaxies undergo a final maximum starburst using the available gas in the central region. The timescale is $\sim$ 300 Myr which is shorter than at the early stage (Cox et al., 2008). The almost all of the local ULIRGs are observed as the systems of the late stage merger. The second peak in the distribution of the merger-age of the GOALS LIRGs occurs at this late stage (Haan et al., 2011). The star formation activities consume $\sim$ 70 – 80 % of the initial gas in a galaxy until merger completes (Mihos & Hernquist, 1996; Cox et al., 2008). After this, the galaxies head to be the remnant galaxies. This stage corresponds the stage 5 and 6 in Figure 1.1.

1.3 Cold Molecular Gas

Formation of massive stars take place in giant molecular clouds (GMC) composed of cold molecular gas. Here, I introduce the tracer of total molecular gas, the emission from cold CO molecules, and the technique to estimate the total molecular gas mass, which is used in this thesis. Previous large surveys of cold CO molecule in local LIRGs are also reviewed.

1.3.1 CO Molecule as a Tracer of Total Molecular Gas

The primary molecular constituent in molecular clouds is the hydrogen molecule, H_2. However, H_2 is a homonuclear diatomic molecule and possesses no electric dipole moment and therefore no transition of dipolar rotations. Thus the lowest energy transition of H_2 is the rotational quadrupole transition in MIR wavelength $\lambda = 28\,\mu$m with $h\nu/k = 514\,$K. This prohibits us from observing cold molecular gas in GMCs, whose temperature is typically only 10–20 K.

Fortunately, carbon monoxide ($^{12}C^{16}O$) can be excited above $h\nu/k = 5.53\,$K and is abundant in GMCs, following H_2. It is easy to excite the transition from the ground state $J = 0 \rightarrow 1$ of CO even in cold GMCs. CO has a weak permanent dipole moment of 0.11 debye, so the critical density to excite of $J = 0 \rightarrow 1$ is as low as $n_{\rm H} \sim 10^3\,{\rm cm}^{-3}$. Thus the emission of CO ($J = 1 \rightarrow 0$) is a good tracer to estimate the "total" molecular gas mass. This transition is at $\lambda = 2.6$ mm ($\nu = 115.27$ GHz). This is a emission in millimeter wavelength, which is not affected by extinction of dust in ISM.

The total molecular gas mass $M_{\rm H_2}$ is estimated from observations of $^{12}C^{16}O$ emission of the transition $J = 1 - 0$ (hereafter simply CO ($J = 1 - 0$) or CO) by multiplying CO luminosity $L'_{\rm CO}$ by a CO-H_2 conversion factor $\alpha_{\rm CO}$ as follows,

$$M_{\rm H_2}[M_\odot] = \alpha_{\rm CO}[M_\odot({\rm Kkms^{-1}pc^2})^{-1}]\, L'_{\rm CO}[{\rm Kkms^{-1}pc^2}] \tag{1.1}$$

The CO-H_2 conversion factor is generally considered to be different between types of galaxies (see the review by Bolatto et al., 2013). This problem is summarized in the following section. Here, $L'_{\rm CO}$ is calculated using the following equation in

Solomon & Vanden Bout (2005),

$$L'_{\rm CO} = 3.25 \times 10^7 S_{\rm CO}\Delta v \nu_{\rm obs}^{-2} D_L^2 (1+z)^{-3} \tag{1.2}$$

where $S_{\rm CO}\Delta v$ is the observed velocity-integrated flux in Jykms^{-1} and z and D_L are the redshift and the luminosity distance in Mpc, respectively. The $L'_{\rm CO}$ can also be represented using the velocity-integrated CO intensity $I_{\rm CO}$ as follows,

$$L'_{\rm CO} = 23.5 \Omega_{s*b} D_L^2 I_{\rm CO} (1+z)^{-3} \tag{1.3}$$

where Ω_{s*b} is the solid angle of the source convolved with the telescope beam.

1.3.2 CO-H_2 Conversion Factor

Here I discuss the theoretical interpretation of the CO-H_2 conversion factor. Since the CO ($J = 1 - 0$) emission is optically thick in GMCs, we observe the flux from the surfaces of the GMCs to as far as $\tau_{\rm CO} = 1$, not the total CO flux. However the CO intensity and the CO luminosity are proportional to the number of clouds and approximately the molecular gas mass in the telescope beam, when simple assumptions are applied, that is,

- The molecular clouds are self-gravitating, i.e., virialized (e.g., Solomon et al., 1987)
- Negligible magnetic energy
- Obey an empirical relation between velocity dispersion and cloud size (e.g., Larson, 1981; Scoville et al., 1987; Solomon et al., 1987), or clouds are supported by turbulence.
- Molecular clouds are clumps with low volume densities in extragalaxies. The $L'_{\rm CO}$ is an ensemble of emission from non-overlapping clouds (the mist model, Dickman et al., 1986). Here, the individual properties of each cloud are averaged by the dominant population.

Thus the CO luminosity is a good tracer of the total molecular gas mass through certain $\alpha_{\rm CO}$.

For the Milky Way and extragalaxies, $\alpha_{\rm CO}$ is determined by observational methodologies: the measurement of virial mass of clouds (Solomon et al., 1987), the indirect measurements of the column density of the hydrogen molecule in GMCs through dust extinction (Pineda et al., 2008), dust column density (Dame et al., 2001), CO isotopologues (Goldsmith et al., 2008) or the gamma ray (Strong & Mattox, 1996), and the modeling of the spectral lines in GMCs (Israel et al., 2006). The Galactic value of $\alpha_{\rm CO}$ is typically $\sim 4.3\,M_{\odot}{\rm Kkms^{-1}pc^2}$ (e.g., Bolatto et al., 2013). However, metallicity, surface gas density and dust temperature in galaxies could affect $\alpha_{\rm CO}$ (e.g., Tacconi et al., 2008; Genzel et al., 2012; Magnelli et al., 2012). The LIRGs and ULIRGs are merging and starbursting, and therefore possibly have dense, hot molecular gas. It is known that starburst galaxies, LIRGs and ULIRGs have lower $\alpha_{\rm CO}$. For example, Downes & Solomon (1998) find $\alpha_{\rm CO}$ of $0.8\,M_{\odot}{\rm Kkms^{-1}pc^2}$ in local ULIRGs. Narayanan et al. (2011) investigate a variation in the CO-H_2 conversion factor along the merger sequence, and find that the CO-H_2 conversion factor decreases at a starburst phase with an enhanced SFR. They attribute this increases in the gas velocity dispersion and the gas temperature at the starburst phase of a merger.

In this thesis, an $\alpha_{\rm CO}$ of 0.6 ${\rm Kkms^{-1}pc^2}$ (Papadopoulos et al., 2012) is used throughout all sources in our sample. This value is taken from Papadopoulos et al. (2012) who performed a one-phase radiative transfer analysis using global ^{12}CO and ^{13}CO emission of local ULIRGs and LIRGs. We perform no correction of $\alpha_{\rm CO}$ for each individual galaxies, although large values in local LIRGs similar to the Galaxy cannot be ruled out (Papadopoulos et al., 2012).

Within a single population of the local LIRGs the dynamic range of the parameters such as metallicity, surface gas density and dust temperature are expected to be relatively small. For instance, the dust temperature of LIRGs is located in a narrow range of 30 – 40 K (Casey, 2012; U et al., 2012), which corresponds to a variation of a factor of 3 on the relation between the dust temperature and $\alpha_{\rm CO}$ by Magnelli et al. (2012). Also, the dispersion of the observed CO intensities is as small as ~ 0.5 dex in our sample, which provides a small variation of less than a factor of 2 based on the correlation between the total surface density and $\alpha_{\rm CO}$ (Bolatto et al., 2013) assuming that local LIRGs have a same gas fraction. Inami et al. (2013) showed a constraint of metallicities of the GOALS LIRGs to $1 \lesssim Z(Z_{\odot}) \lesssim 2$. This metallicity range corresponds to the nearly constant $\alpha_{\rm CO}$ accorinding to the predictions in Bolatto et al. (2013) using the models by Glover

& Mac Low (2011) and Wolfire et al. (2010). Therefore these parameters are likely to be ineffective in changing the $\alpha_{\rm CO}$ in our LIRG sample. We do not consider the variation of $\alpha_{\rm CO}$ within galaxies because only the central regions are observed.

1.3.3 The previous CO Survey

Motivated by the mystery of the energy source of strong IR radiation and fueling in local LIRGs and ULIRGs, many researchers have conducted CO surveys towards local LIRGs and ULIRGs for the last three decades. These vigorous observations found that local LIRGs and ULIRGs are extremely gas-rich galaxies with $M_{\rm H_2} \sim 10^{9-10}\,M_\odot$. Early works were performed with the Five College Radio Astronomical Observatory (FCRAO) 14 m and the National Radio Astronomy Observatory (NRAO) 12 m telescopes by J. S. Young and D. B. Sanders, separately. The pioneering CO surveys following the launch of the IRAS is found in papers by Young et al. (1984) and Sanders & Mirabel (1985). Young et al. (1984) detected CO emission from two LIRGs and found a global correlation between CO luminosity and 100 μm luminosity. Sanders & Mirabel (1985) found that $L_{\rm FIR}/M_{\rm H_2}$ ratio in local LIRGs is 3–20 times higher compared to the ensemble of molecular clouds in the Milky Way, suggesting efficient transformation from gas to stars in galaxies. After this work, many CO surveys were conducted: Sanders et al. (1986), Young et al. (1986b), Young et al. (1986a), Young et al. (1989), Mirabel et al. (1990), Sanders et al. (1991), Mazzarella et al. (1993), Downes et al. (1993), Young et al. (1995), Elfhag et al. (1996), Solomon et al. (1997), Curran et al. (2000), Yao et al. (2003), Gao & Solomon (2004a,b), Saintonge et al. (2011) and García-Burillo et al. (2012). Young et al. (1986a) found that interacting/merging galaxies have significantly high $L_{\rm FIR}/M_{\rm H_2}$ ratios and flux ratios of 60 μm to 100 μm compared to isolated galaxies of comparable molecular gas mass. Sanders et al. (1991) conducted a large CO survey of 60 LIRGs. Combined with sub-LIRGs, they found that advanced mergers have high $L_{\rm FIR}/M_{\rm H_2}$ ratio. These studies evidently suggest enhanced star formation by interactions/mergers. Sanders et al. (1991) also pointed out the presence of the AGN contribution to FIR in galaxies with the highest $L_{\rm FIR}/M_{\rm H_2}$ ratio. Gao & Solomon (2004a,b) conducted a survey of CO and HCN as a dense gas tracer for normal galaxies, LIRGs and ULIRGs. They found a correlation between $L_{\rm IR}/L_{\rm CO}$ ratio and $L_{\rm HCN}/L_{\rm CO}$ ratio (dense gas

fraction) and that $L_{\rm HCN}/L_{\rm CO}$ ratio distinctly divide normal galaxies and LIRGs-ULIRGs. $L_{\rm IR}$ tightly correlates with $L_{\rm HCN}$ from normal galaxies to ULIRGs, and thus they suggest that star formation is the power source in LIRGs and ULIRGs.

Although numerous observations exists to date, it is meaningful to observe the cold CO emission from local LIRGs now again using up-to-date instruments and to study the gas properties in new and wide parameter space constructed by the GOALS observations. Moreover, despite many previous observations, the sample selection criteria of these surveys have prevented obtaining a homogeneous CO dataset of local LIRGs (e.g., Gao & Solomon, 2004a), which is required to infer on the general characteristics of LIRGs concerning cold molecular gas and star formation, in an unbiased manner.

1.4 This Thesis

In this thesis, I present the new CO data of 62 local LIRGs and ULIRGs with the 45 m telescope at the Nobeyama Radio Observatory to infer the amount of the molecular gas of the central region of several kpc scale in local LIRGs. I examine the transportation of the molecular gas and the star formation in interacting/merging LIRGs. The thesis consist of the following parts:

First, I present the sample, the observational method and the data reduction of this new CO survey in Chapter 2. Second, in Chapter 3, I propose a new method to estimate the CO extent in galaxies, which uses two telescopes with different beam sizes. Using the CO extent and the observed molecular gas mass in the central regions, I investigate whether the molecular gas inflow towards the galactic center is a common phenomenon in the interacting/merging LIRGs. Finally, the star formation of local LIRGs and the AGN contribution to the IR luminosity are discussed in Chapter 4.

Chapter 2

CO(J=1-0) Observation

2.1 The Sample

Here I describe the sample of the CO survey in this thesis. The GOALS sample as the parent population is depicted in Section 1.1.2. In this section, the sample selection and the comparison of the sample with the other CO survey samples.

2.1.1 CO Survey Sample

Of the 202 full GOALS LIRGs (Armus et al., 2009), 161 systems have declination of above – 35 degrees (I dub as the Northern GOALS LIRGs), making it observable from the the Nobeyama 45 m telescope[1] (NRO45). Out of this sample, we have observed 79 galaxies in 62 systems (54 LIRGs and 8 ULIRGs), based solely on source availability at the assigned LST range and weather conditions.

The IR luminosities of the 62 systems range from $L_{\rm IR} = 1.10\times10^{11}\,L_{\odot}$–$3.72\times10^{12}\,L_{\odot}$ (see Figure 2.1). We use the IR luminosity for the GOALS sources given in Armus et al. (2009), which calculated the IR luminosity using four IRAS bands from 12 μm to 100 μm, and the derivation in Sanders & Mirabel (1996). Some LIRGs are known to be groups of two or more galaxies. Our sample includes CO observed individually towards 33 galaxies in 16 systems. For the resolved galaxies, the individual IR luminosities are taken from Díaz-Santos et al. (2010) and Howell et al. (2010) who allocated the IR luminosities using the MIR flux density ratios. For those without any available the individual IR luminosities (pairs of NGC 1797, IRAS F10173+0828, NGC 4418 and MCG +04-48-002), we estimate the individual IR luminosities in the same method using MIPS 24 μm flux density ratios. Fifteen sources have the individual IR luminosity of lower than $\log(L_{\rm IR}/L_{\odot}) = 11.0$ and drop out to "sub-LIRGs" Howell et al. (2010). Using the conversion factor of Kennicutt (1998a) from the IR luminosity to the star formation rate (SFR), the individual SFR are $0.07 - 630\,M_{\odot}{\rm yr}^{-1}$ and the median value is $36\,M_{\odot}{\rm yr}^{-1}$ for all sources. For sources with $\log(L_{\rm IR}/L_{\odot}) \geqslant 11.0$, the SFR are $18 - 630\,M_{\odot}{\rm yr}^{-1}$ and the median value is $44\,M_{\odot}{\rm yr}^{-1}$.

The galaxies in the sample are classified by the merger stage and the nuclear energy source using the classifications by Stierwalt et al. (2013) (hereafter ST13

[1]Nobeyama Radio Observatory is a branch of the National Astronomical Observatory of Japan, National Institutes of Natural Sciences.

), who categorize the GOALS LIRGs into five stages of merger: non-mergers with no sign of merger activity or massive neighbors, pre-mergers which are pair galaxies prior to its first encounter, early-stage mergers which show symmetric disks but tidal tails, mid-stage mergers showing amorphous disks and tidal tails, and late-stage mergers with two nuclei in a common envelope (see ST13 for details). The nuclear energy sources are categorized into SB-dominated galaxies, AGN-dominated galaxies and composite galaxies, in a manner identical to Petric et al. (2011), using the 6.2 μm PAH EQW in ST13. Our sample span the full range of merger stage from non-merger to the late-stage merger and the all of the nuclear energy sources (Figure 2.3, 2.4). The sample is tabulated in Table 2.1 with their properties and the observing coordinates.

The heliocentric velocity and the luminosity distance of the sample is taken from Armus et al. (2009). The luminosity distance ranges from 37 Mpc to 400 Mpc ($z = 0.007 - 0.087$), and the median value is 94 Mpc (Figure 2.2).

2.1.2 Comparison of the Sample with the Previous Survey Sample

In order to characterize our sample, the sample is compared with the full GOALS sample and two previous large CO studies, Sanders et al. (1991) (hereafter SSS91) and Gao & Solomon (2004a) (hereafter GS04).

Figure 2.1 shows the number distribution of the systems of this sample with a bin of $\Delta \log (L_{\rm IR}/L_{\odot}) = 0.2$. The distribution of our sample is 11 - 66 % of the full GOALS sources in each bin. The samples in SSS91 and GS04 have peaks of $L_{\rm IR}$ distributions at higher $L_{\rm IR}$ than the full GOALS sample, whereas our sample covers the low IR luminosity range ($\log (L_{\rm IR}/L_{\odot}) < 11.5$), possessing distribution characteristics which are similar to a simple scaling of the full GOALS or northern GOALS sources, with no apparent selection bias on the IR luminosity.

The sample is also not biased towards specific phases of galactic interaction/merger or the dominant source of energy (SB or AGN). Figure 2.3 shows that our sample includes all the stages of the merger process, with a distribution similar to the full GOALS sample, while the LIRGs and ULIRGs in GS04 are biased towards the last stage of a merger and non-interacting galaxies. Figure 2.4 shows that the dominant nuclear energy source of our sample is also similar to

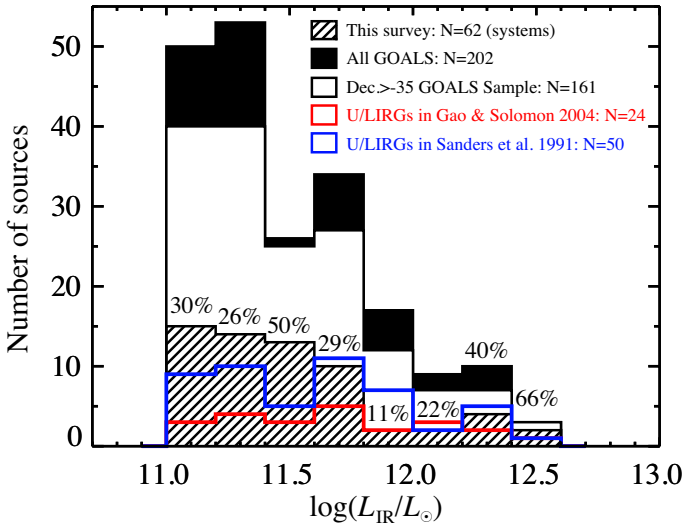

FIGURE 2.1: The distribution of IR luminosities in the systems of the sample (shaded) and references: the full GOALS LIRGs (filled), the northern GOALS LIRGs (filled), the LIRGs and ULIRGs in GS04 (red) and the LIRGs and ULIRGs in SSS91 (blue). The IR luminosity is one in whole galaxy system, and is calculated from the IRAS four bands Armus et al. (2009). The numbers on the bars of our sample mean the fractions of our sources in the full GOALS sources within a bin.

the GOALS sample and U/LIRGs in SSS91, and also to GS04 which is limited in sample size.

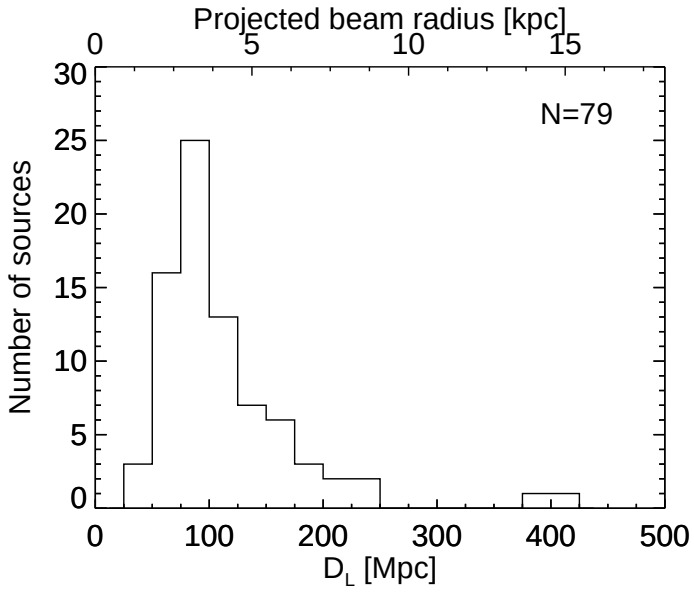

FIGURE 2.2: The luminosity distances and the projected beam radii of $\theta_{\rm mb} = 15''$ by NRO45 for the 79 individual sources. The distance ranges from 37 Mpc to 400 Mpc, corresponding to the beam radius of from 1.3 kpc to 15 kpc. The median distance is 94 Mpc, whose beam diameter is 3.4 kpc.

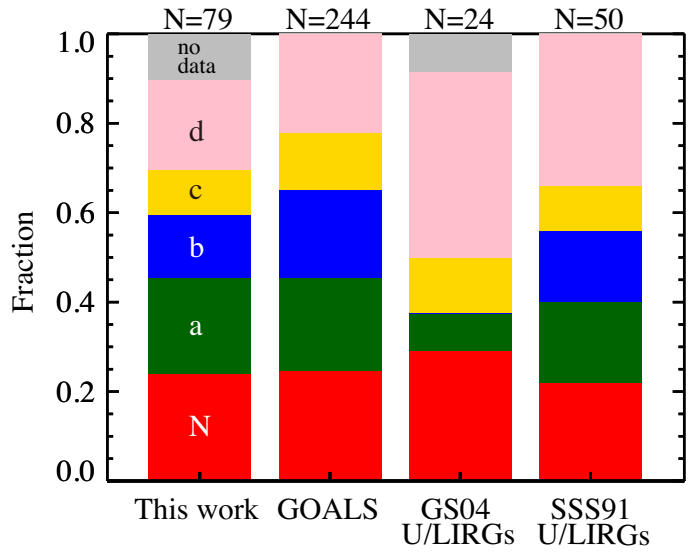

FIGURE 2.3: Merger stage distribution for our sample (individual sources), the GOALS sample (individual sources), GS04 LIRGs and ULIRGs, and SSS91 LIRGs and ULIRGs. The sources of the GOALS sample are cited from ST13. The stages of merger are: N = non-merger (red), a = pre-merger (green), b = early stage merger (blue), c = mid-stage merger (yellow), d = late stage merger (pink), as described in ST13. "no data" means no data of merger stage because of the companion sources not included in ST13 or non-GOALS sources.

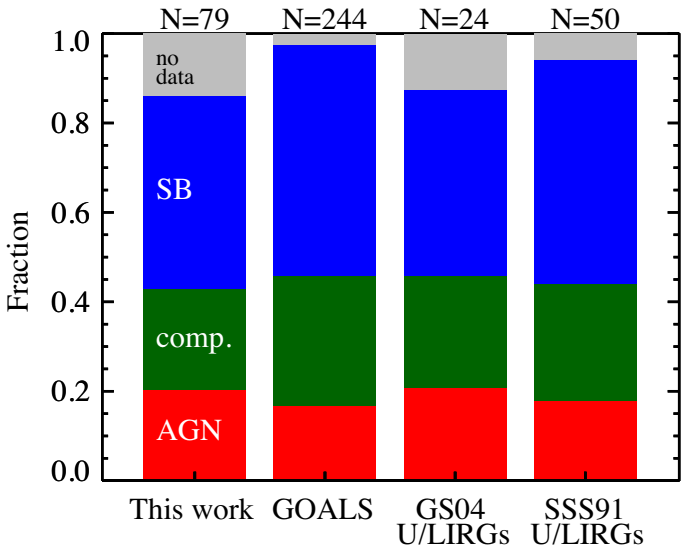

FIGURE 2.4: The distribution of nuclear energy sources for our sample (individual sources), the GOALS sample (individual sources), GS04 LIRGs and ULIRGs, and SSS91 LIRGs and ULIRGs. The energy sources are distinguished according to the 6.2 μm PAH EQW in ST13 using a threshold employed by Petric et al. (2011) into 3 groups: AGN (red), SB (blue) and composites of both (green). "no data" indicates sources with double nuclei within the NRO45 beam in addition to the same reason as Figure 2.3.

Table 2.1: The target sources of the CO observation

Galaxies	R.A.(J2000)	Dec.(J2000)	Velocity (kms^{-1})	D_L (Mpc)	$\log(L_{\mathrm{IR}}/L_{\odot})$
(1)	(2)	(3)	(4)	(5)	(6)
NGC 0034S	$00^{\mathrm{h}}11^{\mathrm{m}}06.55^{\mathrm{s}}$	$-12°06'27.8''$	5881	84.1	11.34^{D}
NGC 0034N	$00^{\mathrm{h}}11^{\mathrm{m}}10.42^{\mathrm{s}}$	$-12°01'16.1''$	5881	84.1	10.57^{D}
MCG -02-01-051	$00^{\mathrm{h}}18^{\mathrm{m}}50.86^{\mathrm{s}}$	$-10°22'37.5''$	8159	117.5	11.48
NGC 0232S	$00^{\mathrm{h}}42^{\mathrm{m}}45.82^{\mathrm{s}}$	$-23°33'41.7''$	6647	95.2	11.28^{D}
NGC 0232N	$00^{\mathrm{h}}42^{\mathrm{m}}52.82^{\mathrm{s}}$	$-23°32'28.5''$	6647	95.2	10.93^{D}
MCG +12-02-001	$00^{\mathrm{h}}54^{\mathrm{m}}03.88^{\mathrm{s}}$	$+73°05'05.6''$	4706	69.8	11.50
IC 1623AB	$01^{\mathrm{h}}07^{\mathrm{m}}47.43^{\mathrm{s}}$	$-17°30'25.1''$	6016	85.5	11.71
MCG -03-04-014	$01^{\mathrm{h}}10^{\mathrm{m}}08.93^{\mathrm{s}}$	$-16°51'11.1''$	10040	144	11.65
CGCG 436-030	$01^{\mathrm{h}}20^{\mathrm{m}}02.59^{\mathrm{s}}$	$+14°21'42.5''$	9362	134	11.69
IRAS F01417+1651	$01^{\mathrm{h}}44^{\mathrm{m}}30.53^{\mathrm{s}}$	$+17°06'08.9''$	8375	119	11.64
NGC 0695	$01^{\mathrm{h}}51^{\mathrm{m}}14.29^{\mathrm{s}}$	$+22°34'55.2''$	9735	139	11.68
UGC 01385	$01^{\mathrm{h}}54^{\mathrm{m}}53.76^{\mathrm{s}}$	$+36°55'04.5''$	5621	79.8	11.05
UGC 01845	$02^{\mathrm{h}}24^{\mathrm{m}}07.89^{\mathrm{s}}$	$+47°58'11.3''$	4679	67	11.12
NGC 0992	$02^{\mathrm{h}}37^{\mathrm{m}}25.50^{\mathrm{s}}$	$+21°06'03.9''$	4141	58	11.07
UGC 02238	$02^{\mathrm{h}}46^{\mathrm{m}}17.50^{\mathrm{s}}$	$+13°05'44.9''$	6560	92.4	11.33
IRAS F02437+2122	$02^{\mathrm{h}}46^{\mathrm{m}}39.13^{\mathrm{s}}$	$+21°35'10.5''$	6987	98.8	11.16
UGC 02369	$02^{\mathrm{h}}54^{\mathrm{m}}01.81^{\mathrm{s}}$	$+14°58'14.3''$	9558	136	11.67
UGC 02608	$03^{\mathrm{h}}15^{\mathrm{m}}01.25^{\mathrm{s}}$	$+42°02'09.2''$	6998	100	11.41
NGC 1275	$03^{\mathrm{h}}19^{\mathrm{m}}48.18^{\mathrm{s}}$	$+41°30'42.2''$	5264	75	11.26
IRAS F03359+1523	$03^{\mathrm{h}}38^{\mathrm{m}}47.02^{\mathrm{s}}$	$+15°32'53.1''$	10613	152	11.55
CGCG 465-012N	$03^{\mathrm{h}}54^{\mathrm{m}}07.64^{\mathrm{s}}$	$+15°59'24.7''$	6662	94.3	10.54^{D}
CGCG 465-012S	$03^{\mathrm{h}}54^{\mathrm{m}}15.97^{\mathrm{s}}$	$+15°55'43.8''$	6662	94.3	11.09^{D}
IRAS 03582+6012	$04^{\mathrm{h}}02^{\mathrm{m}}32.55^{\mathrm{s}}$	$+60°20'39.7''$	8997	131	11.43
IRAS 04271+3849	$04^{\mathrm{h}}30^{\mathrm{m}}33.10^{\mathrm{s}}$	$+38°55'48.4''$	5640	80.8	11.11
NGC 1797F	$05^{\mathrm{h}}07^{\mathrm{m}}44.56^{\mathrm{s}}$	$-07°58'09.8''$	4441	63.4	9.20^{D}
NGC 1797	$05^{\mathrm{h}}07^{\mathrm{m}}44.82^{\mathrm{s}}$	$-08°01'08.6''$	4441	63.4	11.03^{D}
CGCG 468-002S	$05^{\mathrm{h}}08^{\mathrm{m}}19.67^{\mathrm{s}}$	$+17°21'47.7''$	5454	77.9	10.92^{D}
CGCG 468-002N	$05^{\mathrm{h}}08^{\mathrm{m}}21.19^{\mathrm{s}}$	$+17°22'08.2''$	5454	77.9	10.92^{D}
IRAS 05083+2441	$05^{\mathrm{h}}11^{\mathrm{m}}25.83^{\mathrm{s}}$	$+24°45'18.7''$	6915	99.2	11.26
IRAS 05129+5128	$05^{\mathrm{h}}16^{\mathrm{m}}55.94^{\mathrm{s}}$	$+51°31'57.0''$	8224	120	11.42
IRAS F05187-1017	$05^{\mathrm{h}}21^{\mathrm{m}}06.52^{\mathrm{s}}$	$-10°14'45.6''$	8474	122	11.3
IRAS 05223+1908	$05^{\mathrm{h}}25^{\mathrm{m}}16.65^{\mathrm{s}}$	$+19°10'48.5''$	8867	128	11.65
MCG +08-11-002	$05^{\mathrm{h}}40^{\mathrm{m}}43.66^{\mathrm{s}}$	$+49°41'41.8''$	5743	83.7	11.46
UGC 03351	$05^{\mathrm{h}}45^{\mathrm{m}}48.01^{\mathrm{s}}$	$+58°42'03.7''$	4455	65.8	11.28
IRAS 05442+1732	$05^{\mathrm{h}}47^{\mathrm{m}}11.16^{\mathrm{s}}$	$+17°33'47.2''$	5582	80.5	11.30
UGC 03410N	$06^{\mathrm{h}}13^{\mathrm{m}}58.14^{\mathrm{s}}$	$+80°28'34.5''$	3921	59.7	10.29^{D}
UGC 03410S	$06^{\mathrm{h}}14^{\mathrm{m}}29.64^{\mathrm{s}}$	$+80°26'59.4''$	3921	59.7	11.03^{D}
IRAS 07251-0248	$07^{\mathrm{h}}27^{\mathrm{m}}37.53^{\mathrm{s}}$	$-02°54'54.2''$	26249	400	12.39

Galaxies	R.A.(J2000)	Dec.(J2000)	Velocity (kms^{-1})	D_L (Mpc)	$\log(L_{\mathrm{IR}}/L_{\odot})$
(1)	(2)	(3)	(4)	(5)	(6)
NGC 2623	$08^{\mathrm{h}}38^{\mathrm{m}}24.14^{\mathrm{s}}$	$+25°45'16.7''$	5549	84.1	11.60
IRAS F09111-1007W	$09^{\mathrm{h}}13^{\mathrm{m}}36.42^{\mathrm{s}}$	$-10°19'29.8''$	16231	246	11.86^{D}
IRAS F09111-1007E	$09^{\mathrm{h}}13^{\mathrm{m}}38.82^{\mathrm{s}}$	$-10°19'20.0''$	16231	246	11.62^{D}
UGC 05101	$09^{\mathrm{h}}35^{\mathrm{m}}51.66^{\mathrm{s}}$	$+61°21'11.5''$	11802	177	12.01
MCG +08-18-013S	$09^{\mathrm{h}}36^{\mathrm{m}}30.87^{\mathrm{s}}$	$+48°28'10.1''$	7777	117	9.93^{D}
MCG +08-18-013N	$09^{\mathrm{h}}36^{\mathrm{m}}37.16^{\mathrm{s}}$	$+48°28'28.2''$	7777	117	11.32^{D}
IRAS F10173+0828	$10^{\mathrm{h}}20^{\mathrm{m}}00.19^{\mathrm{s}}$	$+08°13'33.9''$	14716	224	11.86^{D}
IRAS F10173+0828F	$10^{\mathrm{h}}20^{\mathrm{m}}01.41^{\mathrm{s}}$	$+08°11'31.7''$	14716	224	9.60^{D}
CGCG 011-076F	$11^{\mathrm{h}}21^{\mathrm{m}}08.34^{\mathrm{s}}$	$-02°59'38.0''$	7464	117	10.02^{D}
CGCG 011-076	$11^{\mathrm{h}}21^{\mathrm{m}}12.24^{\mathrm{s}}$	$-02°59'01.9''$	7464	117	11.41^{D}
IC 2810W	$11^{\mathrm{h}}25^{\mathrm{m}}45.00^{\mathrm{s}}$	$+14°40'36.4''$	10192	157	11.45^{D}
IC 2810E	$11^{\mathrm{h}}25^{\mathrm{m}}49.48^{\mathrm{s}}$	$+14°40'06.7''$	10192	157	11.20^{D}
NGC 4194	$12^{\mathrm{h}}14^{\mathrm{m}}09.64^{\mathrm{s}}$	$+54°31'36.1''$	2501	43	11.10
IRAS F12224-0624	$12^{\mathrm{h}}25^{\mathrm{m}}03.95^{\mathrm{s}}$	$-06°40'52.9''$	7902	125	11.36
NGC 4418	$12^{\mathrm{h}}26^{\mathrm{m}}54.66^{\mathrm{s}}$	$-00°52'39.5''$	2179	36.5	11.19^{D}
NGC 4418F	$12^{\mathrm{h}}27^{\mathrm{m}}04.96^{\mathrm{s}}$	$-00°54'25.8''$	2179	36.5	8.59^{D}
Mrk 231	$12^{\mathrm{h}}56^{\mathrm{m}}14.10^{\mathrm{s}}$	$+56°52'25.7''$	12642	192	12.57
UGC 08387	$13^{\mathrm{h}}20^{\mathrm{m}}35.31^{\mathrm{s}}$	$+34°08'22.7''$	6985	110	11.73
Mrk 273	$13^{\mathrm{h}}44^{\mathrm{m}}42.14^{\mathrm{s}}$	$+55°53'13.9''$	11326	173	12.21
CGCG 247-020	$14^{\mathrm{h}}19^{\mathrm{m}}43.35^{\mathrm{s}}$	$+49°14'11.5''$	7716	120	11.39
IRAS F14348-1447	$14^{\mathrm{h}}37^{\mathrm{m}}38.32^{\mathrm{s}}$	$-15°00'22.7''$	24802	387	12.39
CGCG 049-057	$15^{\mathrm{h}}13^{\mathrm{m}}13.07^{\mathrm{s}}$	$+07°13'32.3''$	3897	65.4	11.35
Arp 220	$15^{\mathrm{h}}34^{\mathrm{m}}57.25^{\mathrm{s}}$	$+23°30'11.1''$	5434	87.9	12.28
IRAS F17207-0014	$17^{\mathrm{h}}23^{\mathrm{m}}21.98^{\mathrm{s}}$	$-00°17'00.6''$	12834	198	12.46
UGC 11041	$17^{\mathrm{h}}54^{\mathrm{m}}51.82^{\mathrm{s}}$	$+34°46'34.3''$	4881	77.5	11.11
CGCG 141-034	$17^{\mathrm{h}}56^{\mathrm{m}}56.61^{\mathrm{s}}$	$+24°01'02.0''$	5944	93.4	11.20
CGCG 142-034S	$18^{\mathrm{h}}16^{\mathrm{m}}33.84^{\mathrm{s}}$	$+22°06'38.4''$	5599	88.1	10.64^{D}
CGCG 142-034N	$18^{\mathrm{h}}16^{\mathrm{m}}40.69^{\mathrm{s}}$	$+22°06'46.2''$	5599	88.1	11.03^{D}
MCG +04-48-002S	$20^{\mathrm{h}}28^{\mathrm{m}}28.85^{\mathrm{s}}$	$+25°43'24.6''$	4167	64.2	10.68^{D}
MCG +04-48-002N	$20^{\mathrm{h}}28^{\mathrm{m}}35.03^{\mathrm{s}}$	$+25°44'00.6''$	4167	64.2	11.06^{D}
IRAS 20351+2521	$20^{\mathrm{h}}37^{\mathrm{m}}17.72^{\mathrm{s}}$	$+25°31'38.0''$	10102	151	11.61
CGCG 448-020	$20^{\mathrm{h}}57^{\mathrm{m}}24.33^{\mathrm{s}}$	$+17°07'38.3''$	10822	161	11.94
ESO 602-G025	$22^{\mathrm{h}}31^{\mathrm{m}}25.44^{\mathrm{s}}$	$-19°02'03.9''$	7507	110	11.34
UGC 12150	$22^{\mathrm{h}}41^{\mathrm{m}}12.20^{\mathrm{s}}$	$+34°14'56.2''$	6413	93.5	11.35
IC 5298	$23^{\mathrm{h}}16^{\mathrm{m}}00.65^{\mathrm{s}}$	$+25°33'23.7''$	8221	119	11.60
NGC 7752S	$23^{\mathrm{h}}46^{\mathrm{m}}58.48^{\mathrm{s}}$	$+29°27'31.8''$	5120	73.6	11.07^{D}
NGC 7752N	$23^{\mathrm{h}}47^{\mathrm{m}}04.74^{\mathrm{s}}$	$+29°29'00.2''$	5120	73.6	11.07^{D}
NGC 7771N	$23^{\mathrm{h}}51^{\mathrm{m}}03.90^{\mathrm{s}}$	$+20°09'00.8''$	4277	61.2	10.74^{D}
NGC 7771S2	$23^{\mathrm{h}}51^{\mathrm{m}}22.43^{\mathrm{s}}$	$+20°05'46.9''$	4277	61.2	10.67^{D}
NGC 7771S1	$23^{\mathrm{h}}51^{\mathrm{m}}24.79^{\mathrm{s}}$	$+20°06'41.7''$	4277	61.2	11.17^{D}
Mrk 331	$23^{\mathrm{h}}51^{\mathrm{m}}26.72^{\mathrm{s}}$	$+20°35'09.5''$	5541	79.3	11.50

Galaxies	R.A.(J2000)	Dec.(J2000)	Velocity (kms^{-1})	D_L (Mpc)	$\log(L_{\mathrm{IR}}/L_{\odot})$
(1)	(2)	(3)	(4)	(5)	(6)

The columns are as follows: Col. (1): The galaxy name, expressly the interacting galaxies are labeled by "N", "E", "S" and "W" in pair galaxies. Col. (2), (3): The observing coordinates, which is the brightest position in 24 μm image from MIPS/*Spitzer*. Col. (4), (5) and (6): The heliocentric velocity of galaxies, the luminosity distance and the IR luminosity taken from Armus et al. (2009). For resolved galaxies, the individual IR luminosities are shown, which are taken from Howell et al. (2010) (H) and Díaz-Santos et al. (2010) (D), or are estimated by us (X) (see text for details).

2.2 CO Observation and Analysis

2.2.1 Observation

The $^{12}\mathrm{CO}(J = 1 - 0)$ line emission was observed using the NRO45 over four semesters from January 2010 to February 2013. CO emission from the sources were measured with the single beam at the coordinates of the brightest point in their 24 μm of MIPS/Spitzer images. The frequency of $^{12}\mathrm{CO}(J = 1 - 0)$ emission is 115.27 GHz. The main beam size of the telescope at 115 GHz is $15''$. The projected beam radius ranges 1.3 – 15 kpc (see Figure 2.2) and the median value is 3.4 kpc at the median distance of the sample, 94 Mpc. Almost all of the sources ($\sim 80\,\%$) have the projected radius of less than 5 kpc.

The observations employed two types of dual- polarization two sideband-separating SIS mixer systems, T100H/V Nakajima et al. (2008) and TZ Nakajima et al. (2013), as a frontend, depending on availability. As the backend spectrometer in the first run, the wide-band-mode acoustooptical spectrometer (AOS-W) and the digital autocorrelator (AC45) were employed. AOS-W and AC45 have the frequency bandwidths of 250 MHz and 512 MHz, corresponding to ~ 652 kms^{-1} and 1336 kms^{-1} velocity bandwidths at 115 GHz, respectively. The frequency resolutions are 250 kHz and 910 kHz, corresponding to a velocity resolutions 0.652 kms^{-1} and 2.37 kms^{-1}, for AOS-W and AC45 respectively. From the second run to the fourth we utilized a broad bandwidth spectrometer, SAM45 Kamazaki et al. (2012), which enables us to obtain spectra in a broader bandwidth than those in the previous run. SAM45 was employed in the mode of a frequency coverage of 2 GHz ($= 5217\,\mathrm{kms}^{-1}$) and a frequency resolution of 488 kHz ($= 1.27\,\mathrm{kms}^{-1}$). For

some galaxies whose spectra were obtained with several spectrometers, the one with the higher signal-to-noise ratio (S/N) is used for analysis.

Flux of the obtained spectra were calibrated with the chopper wheel method and by observing standard sources. System noise temperatures, throughout all the observations, was typically 150–250 K on the antenna temperature scale (T_A^*) at the observed frequency. The pointing of the telescope was regularly checked every 30–60 minutes by observing SiO masers, with typical r.m.s. errors of $\sim 3''$. The spectra of observed CO emissions are shown in Figure 2.5 with the observed position of the CO beam, superposed on the near-IR images and MIR contours.

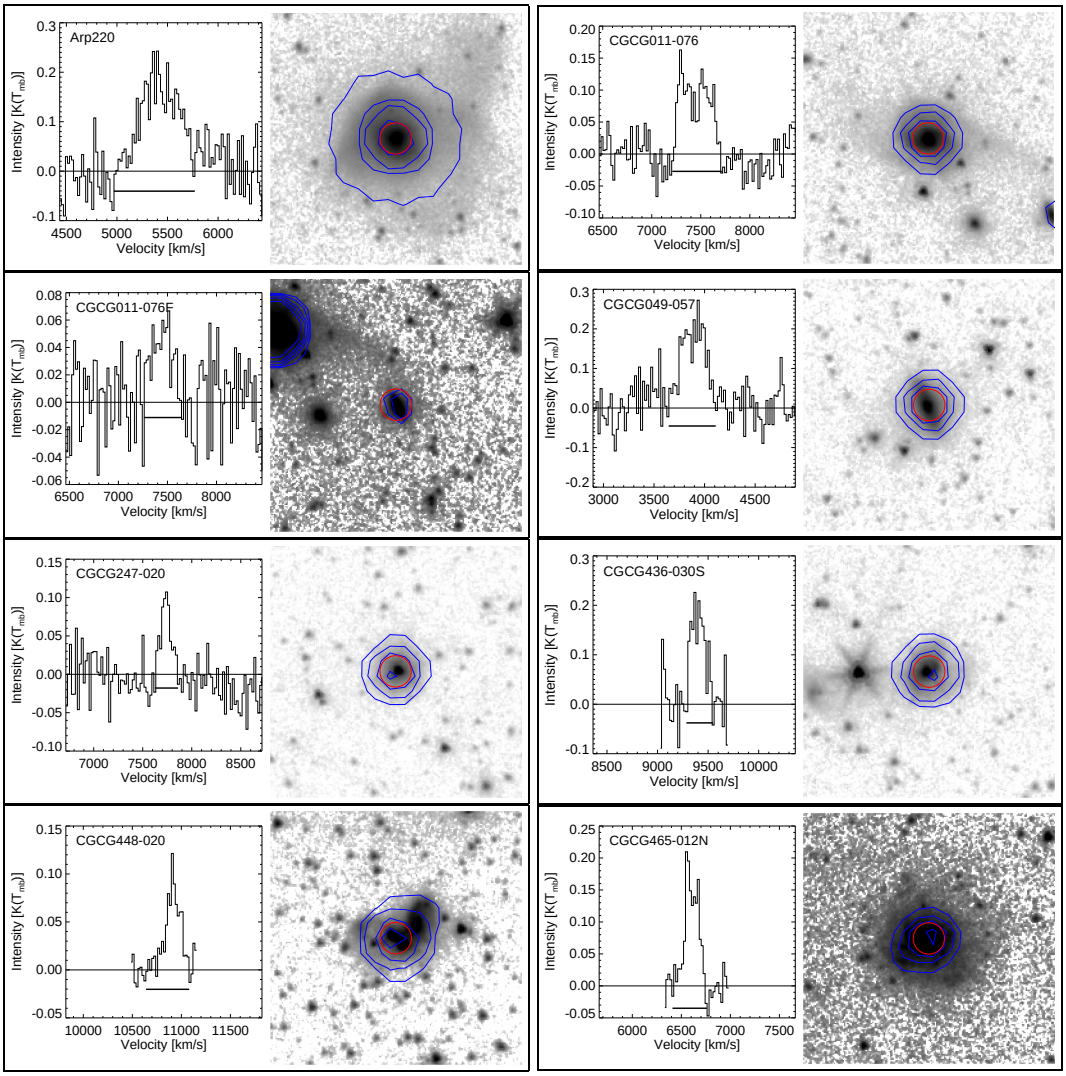

FIGURE 2.5: The CO spectrum and the 3.6 μm image (*Spitzer*/IRAC) for the sample. The intensity is in the temperature scale of the main beam temperature, $T_{\rm mb}$. The velocity range on x-axis is 2000 kms^{-1}. The solid bar under the spectrum represents the integral range to derive the integral intensity. The beam with the diameter of 15″ (red circle) and *Spitzer*/MIPS 24 μm (blue contour) are overlaid on the 3.6 μm image (half tone). The contour levels are 0.2, 0.4, 0.6 and 0.8 of the peak intensity in logarithmic scale. The image covers an area of 2′ × 2′ on the sky.

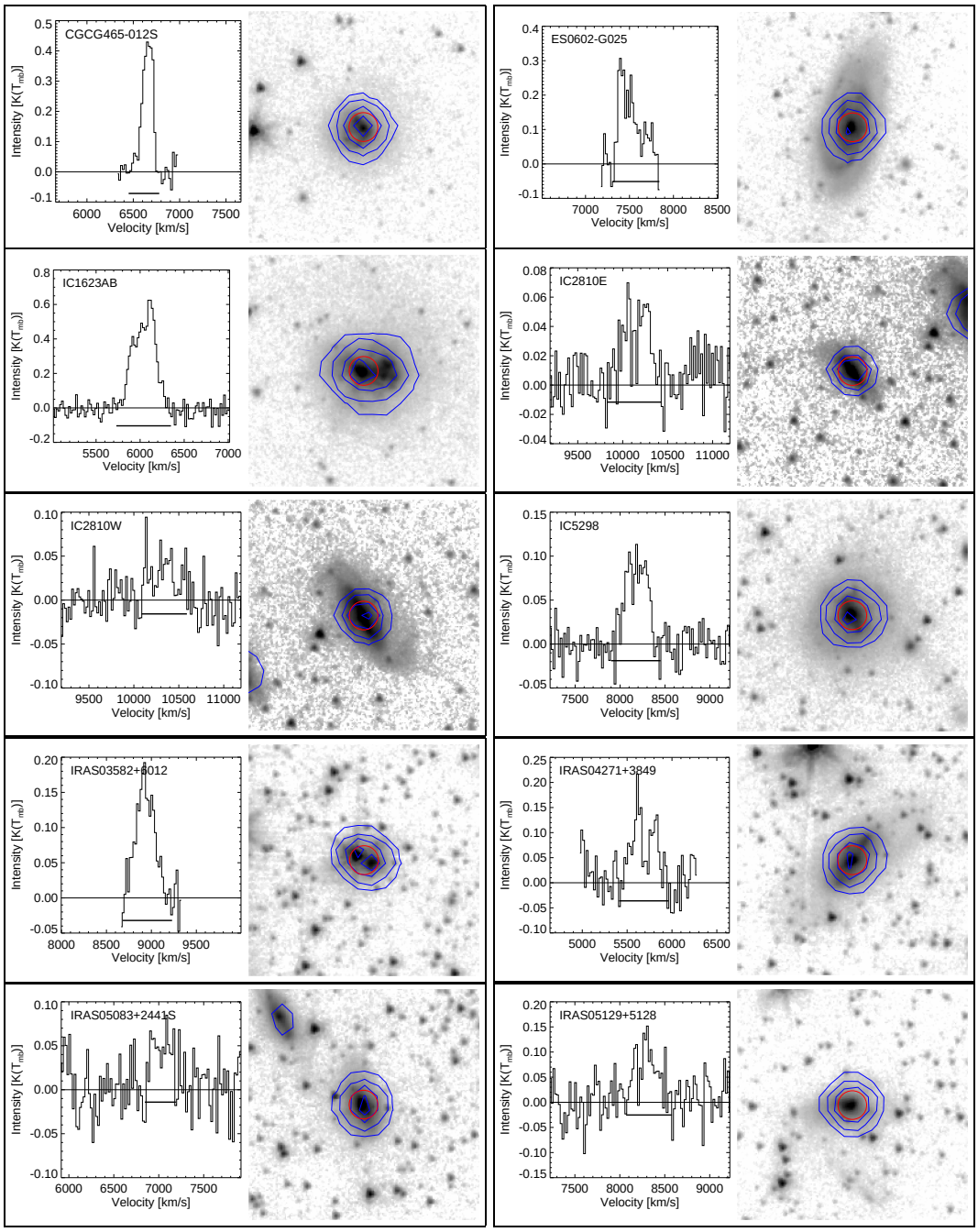

FIGURE 2.5: *Continued.*

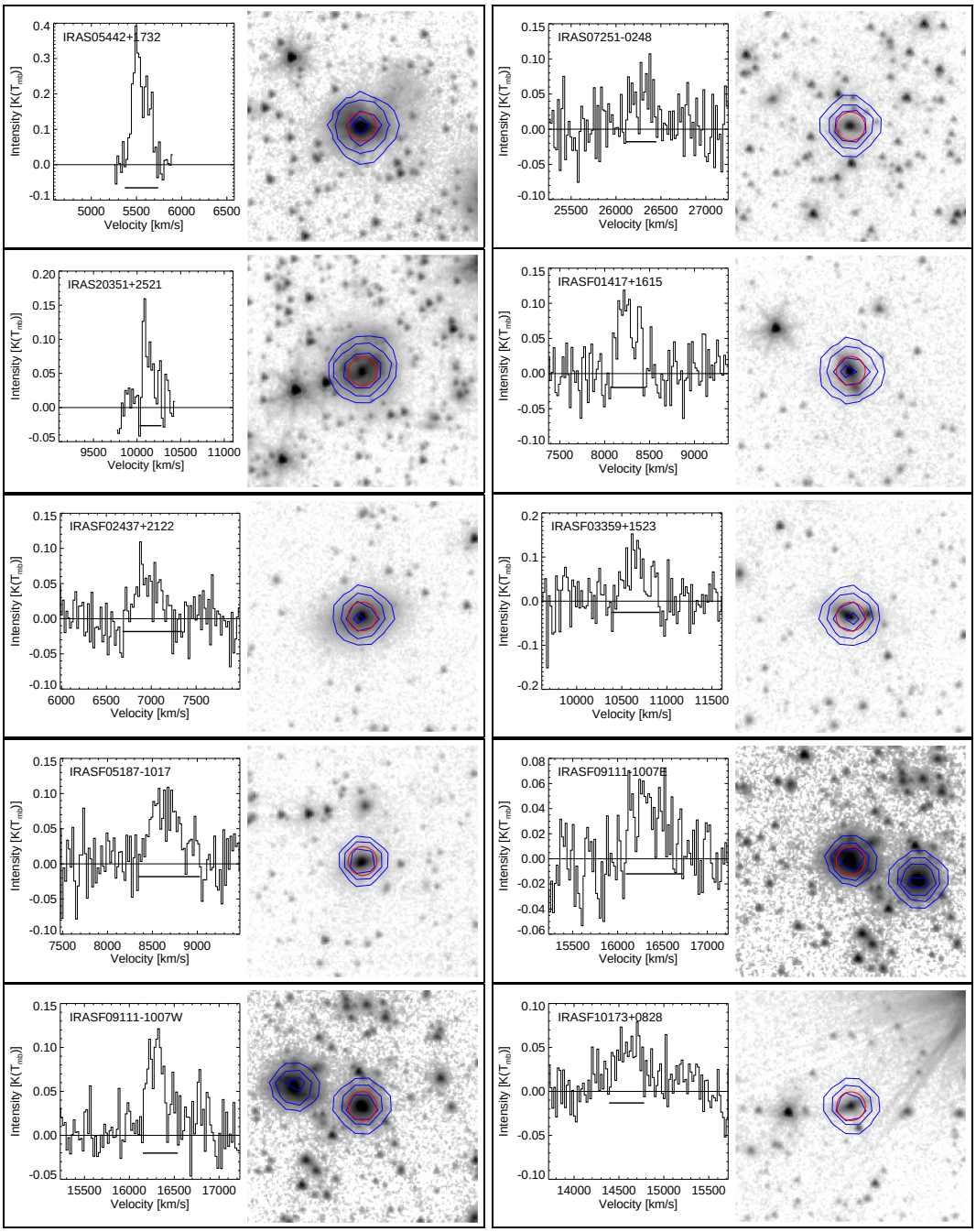

FIGURE 2.5: *Continued.*

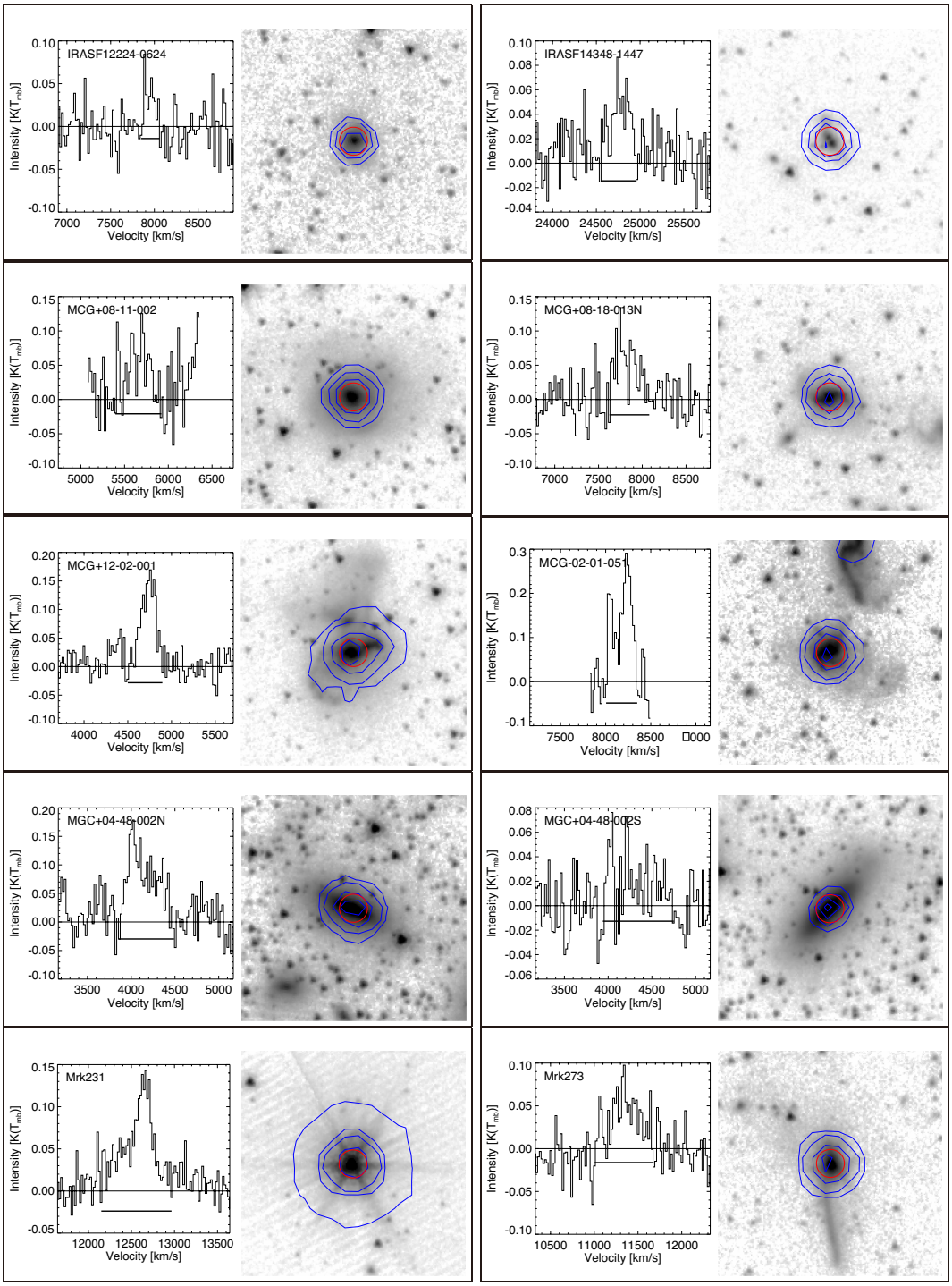

FIGURE 2.5: *Continued.* but the 4.5 μm image (*Spitzer*/IRAC) of NGC 0034N is used because of no 3.6 μm image.

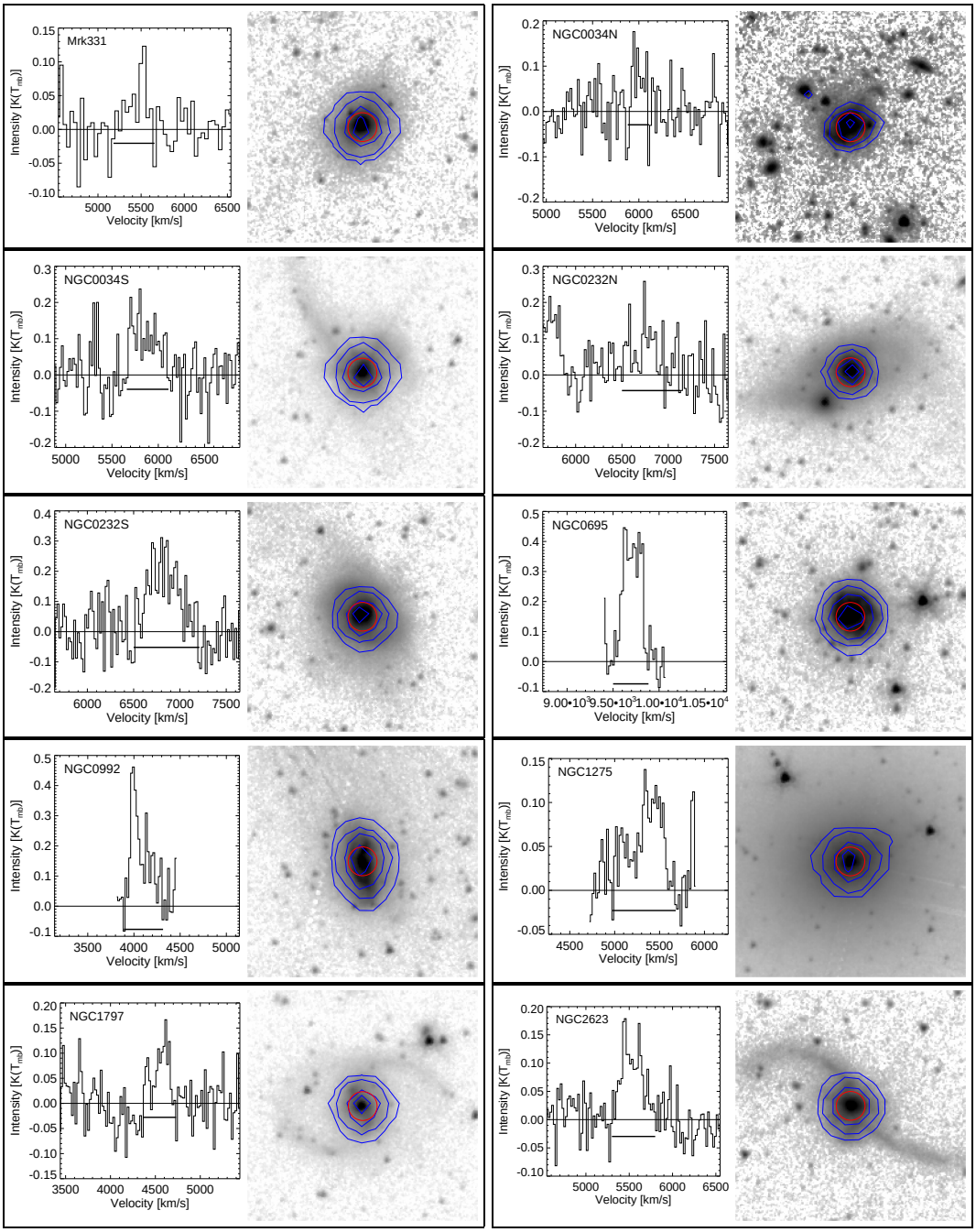

FIGURE 2.5: *Continued.* but no *Spitzer*/MIPS 24 μm contour of NGC 4194 is used because it is not available.

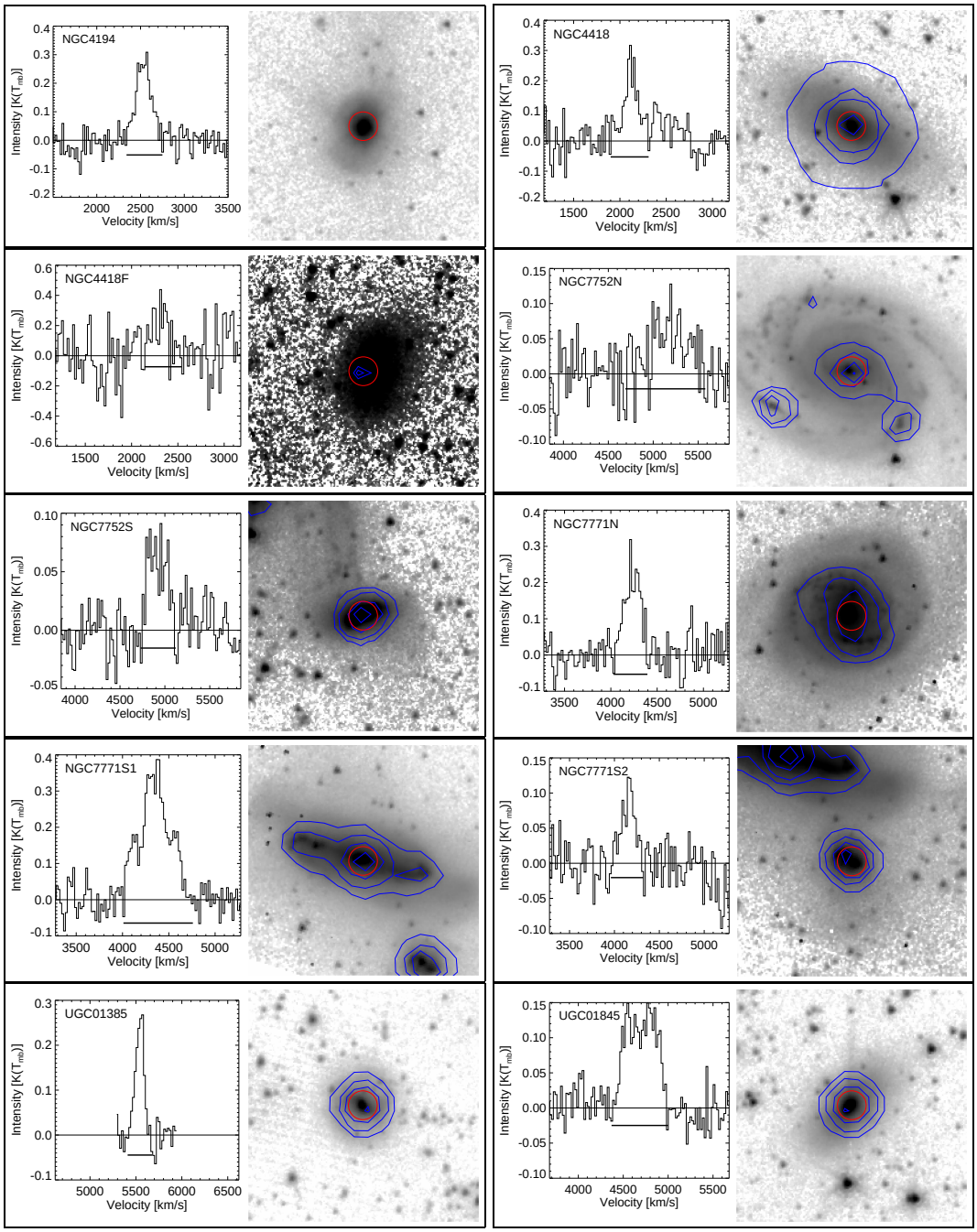

FIGURE 2.5: *Continued.*

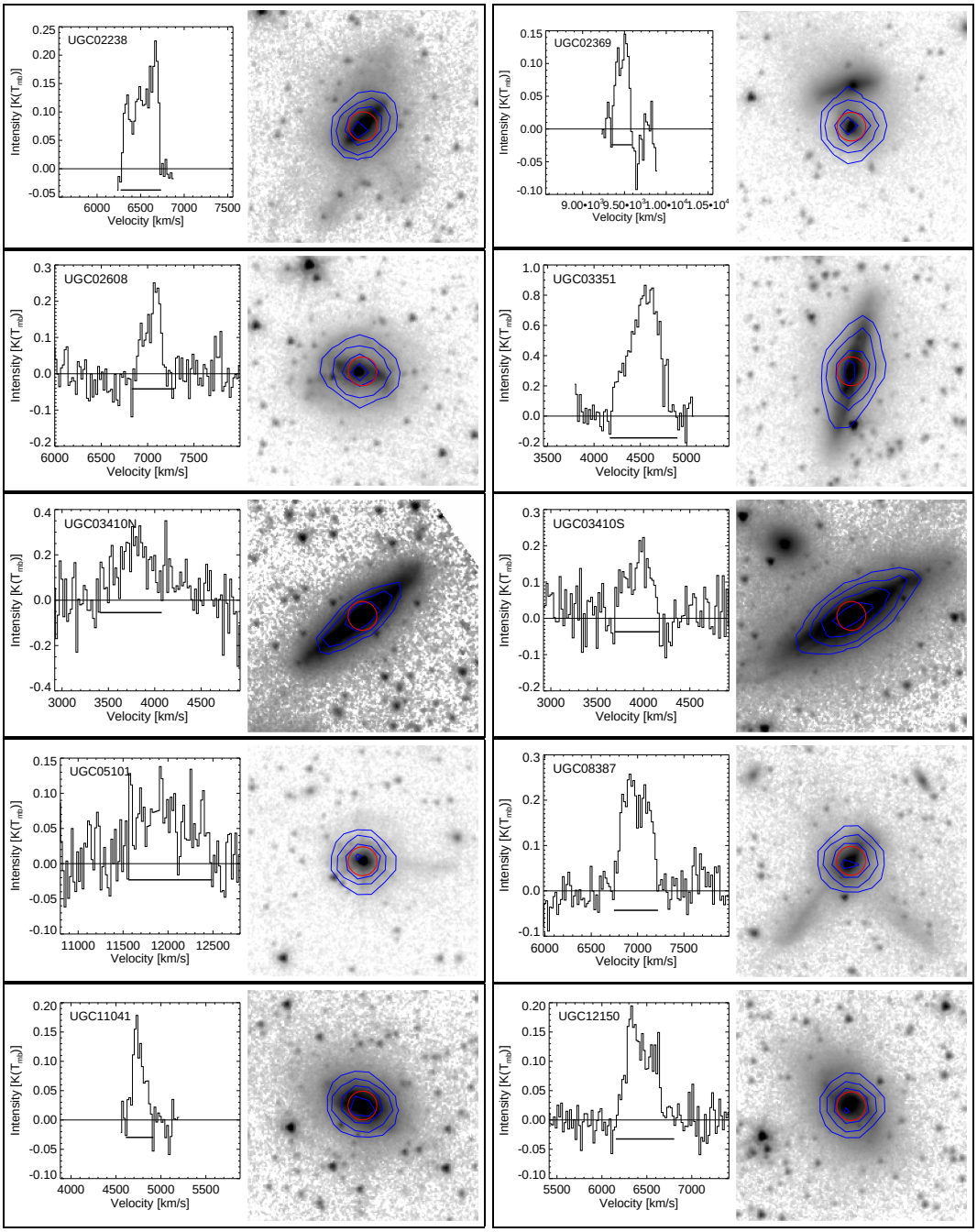

FIGURE 2.5: *Continued.*

2.2.2 Data Reduction and Analysis

The primary data reduction is performed by *NEWSTAR*, a software distributed by NRO. After subtraction of the reference position spectra, baselines are fitted with polynomial functions of order 1, but we use second to third orders in limited cases with baseline fluctuations. Averaging was done using weights of $1/\mathrm{rms}^2$. The spectra are then smoothed to a velocity resolution of 20 kms^{-1} with a box function in order to improve the S/N, except for IRAS F12224-0624 smoothed to a bin of 60 kms^{-1} and Mrk 331 to a bin of 40 kms^{-1}. The CO velocity-integrated intensity is derived from the main beam temperature and the full velocity width and is represented as follows:

$$I_{\mathrm{CO}} = \int T_{\mathrm{mb}}\, dV = \int \frac{T_{\mathrm{A}}^{*}}{\eta_{\mathrm{mb}}}\, dV\,, \tag{2.1}$$

where I_{CO} is in a unit of K kms^{-1}, T_{mb} is the main beam temperature in K and η_{mb} is the main beam efficiency which is 0.38, 0.36, 0.31 and 0.282 in the first, second, third and fourth runs, respectively. The performed integral range is indicated by a horizontal solid line below the spectrum in Figure 2.5. In order to look for systematic calibration uncertainties, we further calibrate the integrated intensity using observations of a standard source, NGC 7538, IRC +10210 and W51. The calibration factor is determined for each observing days and ranges from 0.838 to 2.80. The median is 1.14. The standard sources were not observed in the first run, so were bootstrapped to sources which were observed over several runs. The uncertainties in I_{CO} which is estimated from variations of fluxes of standard sources are typically about 13 %.

Of the 79 observed sources, 68 sources were detected, giving a detection rate of 86 %. Five out of 11 non-detection sources are companions with fainter IR luminosity in a paired system, which is expected to have a little molecular gas. The other sources may be actually deficient in molecular gas. For 11 sources not detected, 3 σ upper limits of their integrated CO intensity are estimated on the assumption that the sources have a Gaussian-shaped spectrum with a velocity width corresponding to the average over all detected sources, $\sim 300\,\mathrm{kms}^{-1}$.

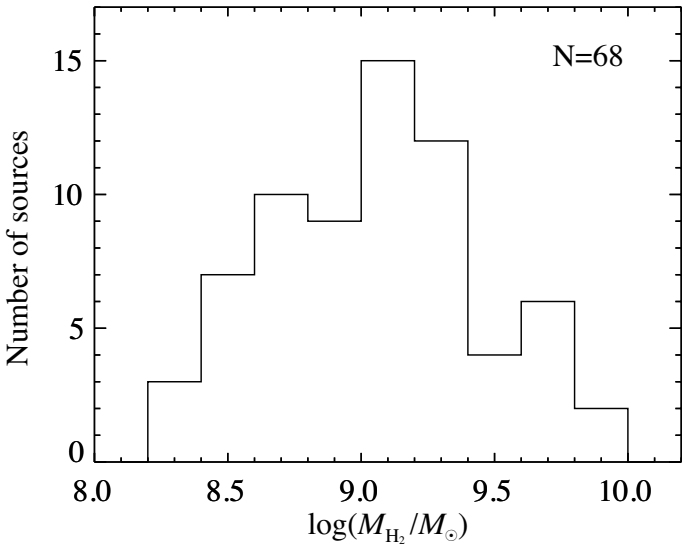

FIGURE 2.6: The histogram of the observed molecular gas mass of the sample. The average is $1.70 \times 10^9\,M_\odot$, the median value is $1.22 \times 10^9\,M_\odot$ of UGC 02608, the minimum is $2.15 \times 10^8\,M_\odot$ of MCG +04-48-002S, and the maximum is $6.96 \times 10^9\,M_\odot$ of IRAS 07251-0248.

2.3 Observational Results

2.3.1 Molecular Gas Mass

The CO luminosity is calculated using Equation 1.3, where $\Omega_{s*b} = \theta^2_{\rm mb}$. The molecular gas mass $M_{\rm H_2}$ is calculated using Equation 1.1 and the CO-H_2 conversion factor $\alpha_{\rm CO} = 0.6 \pm 0.2\,M_\odot({\rm Kkms^{-1}pc^{-2}})^{-1}$ (Papadopoulos et al. (2012); see also discussion about $\alpha_{\rm CO}$ in Section 1.3.2) for all sources in the sample. The calculated CO luminosity and molecular gas mass are shown in Table 2.2. The $M_{\rm H_2}$ ranges from $2.15 \times 10^8\,M_\odot$ to $6.96 \times 10^9\,M_\odot$, and the histogram of $M_{\rm H_2}$ of the sample is shown in Figure 2.6.

2.3.2 Velocity Width

The full width at half maximum (FWHM) of the velocity width, $\Delta V_{\rm FWHM}$, of the CO line of all detected sources are derived. The error in the $\Delta V_{\rm FWHM}$ is estimated by its variation depending on the peak intensity uncertainty, and is $\sim$

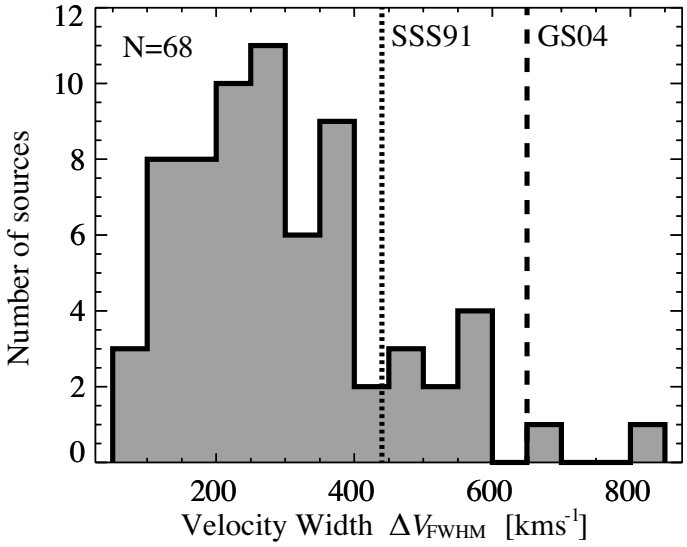

FIGURE 2.7: The histogram of the velocity width $\Delta V_{\rm FWHM}$ of CO line. The average value is 300 kms^{-1}. The maximum is 840 kms^{-1} of UGC 05101. A vertical dotted line and a dashed line represent maximum values observed by SSS91 and GS04, respectively.

35 % on average. The calculated FWHMs of some sources which have available literature spectra are compared with the literature $\Delta V_{\rm FWHM}$ and tend to be somewhat larger than the literature values. This is due to its shape of a spectrum. The full width at zero intensities and the line profiles are similar to those of the literature.

Figure 2.7 shows the distribution of $\Delta V_{\rm FWHM}$, indicating that $\Delta V_{\rm FWHM}$ is $\sim$ 300 kms^{-1} on average, ranging from 80 kms^{-1} to 840 kms^{-1}. The maximum value of $\Delta V_{\rm FWHM}$ observed by SSS91 and GS04 are also shown in Figure 2.7 and are 440 kms^{-1} and 650 kms^{-1}, respectively. Two galaxies, UGC 05101 and MCG +04-48-002S, have the high velocity-widths over the maximum width of GS04. Our observation using the broader spectrometer compared to those of the previous observations could capture components of gas with anomalous velocities. While the maximum velocity coverages of the employed spectrometer is $\sim$ 5200 kms^{-1} at 115 GHz, those in SSS91 and GS04 are 1330 kms^{-1} and 1560 kms^{-1}, respectively.

Table 2.2: Result of the single-point observation

Galaxies	Backend	ΔV_0 (kms^{-1})	ΔV_{FWHM} (kms^{-1})	I_{CO} (Kkms^{-1})	$S_{\mathrm{CO}}\Delta V$ (Jykms^{-1})	$S_{\mathrm{CO}}\Delta V$(ref) (Jykms^{-1})	L'_{CO} ($10^8\,L'$)	$M_{\mathrm{H_2}}$ ($10^8\,M_\odot$)
(1)	(2)	(3)	(4)	(5)	(6)	(7)	(8)	(9)
NGC 0034S	SAM45	420	293	46.13 ± 5.67	113.0 ± 13.9		18.4 ± 2.27	11.1 ± 1.36
NGC 0034N	SAM45	200	166	12.86 ± 3.63	31.50 ± 8.89		5.14 ± 1.45	3.08 ± 0.871
MCG -02-01-051	AOS	320	277	51.58 ± 2.43	126.4 ± 6.0		39.4 ± 1.86	23.6 ± 1.11
NGC 0232S	SAM45	680	436	89.24 ± 8.17	218.6 ± 20.0		45.4 ± 4.15	27.2 ± 2.49
NGC 0232N	SAM45	600	373	38.57 ± 5.97	94.50 ± 14.64		19.6 ± 3.04	11.8 ± 1.82
MCG +12-02-001	SAM45	395	178	30.79 ± 1.97	75.44 ± 4.84		8.58 ± 0.55	5.15 ± 0.33
IC 1623AB	SAM45	580	307	170.6 ± 4.1	418.1 ± 10.0	493.5[c]	70.4 ± 1.68	42.3 ± 1.01
MCG -03-04-014	AOS			< 29.33	< 71.86		< 33	< 19.8
CGCG 436-030	AOS	240	206	32.42 ± 1.92	79.43 ± 4.69		31.8 ± 1.88	19.1 ± 1.13
IRAS F01417+1651	SAM45	340	272	23.44 ± 2.50	57.44 ± 6.11	63.0[c]	18.3 ± 1.95	11 ± 1.17
NGC 0695	AOS	360	250	96.53 ± 2.80	236.5 ± 6.9	199.9[b]	102 ± 2.95	60.9 ± 1.77
UGC 01385	AOS	240	103	28.59 ± 0.80	70.04 ± 1.95		10.3 ± 0.287	6.19 ± 0.172
UGC 01845	SAM45	600	458	55.98 ± 1.80	137.2 ± 4.4		14.4 ± 0.461	8.62 ± 0.277
NGC 0992	AOS	400	187	71.47 ± 2.73	175.1 ± 6.7	207.9[c]	13.8 ± 0.527	8.3 ± 0.316
UGC 02238	AOS	440	382	53.22 ± 0.94	130.4 ± 2.3	210.0[c]	25.5 ± 0.452	15.3 ± 0.271
IRAS F02437+2122	SAM45	640	235	16.64 ± 2.72	40.76 ± 6.67		9.08 ± 1.49	5.45 ± 0.892
UGC 02369	AOS	220	173	20.55 ± 0.91	50.34 ± 2.23		20.7 ± 0.917	12.4 ± 0.55
UGC 02608	SAM45	420	223	36.30 ± 3.59	88.94 ± 8.80		20.3 ± 2.01	12.2 ± 1.21
NGC 1275	AC45	680	538	40.08 ± 1.83	98.21 ± 4.48	35.7[b]	12.8 ± 0.585	7.69 ± 0.351
IRAS F03359+1523	SAM45	500	318	28.36 ± 3.97	69.48 ± 9.73	133.0[c]	35.4 ± 4.95	21.2 ± 2.97

Table 2.2: Result of the single-point observation

Galaxies	Backend	ΔV_0	$\Delta V_{\rm FWHM}$	$I_{\rm CO}$	$S_{\rm CO}\Delta V$	$S_{\rm CO}\Delta V$(ref)	$L'_{\rm CO}$	$M_{\rm H_2}$
		(kms^{-1})	(kms^{-1})	(Kkms^{-1})	(Jykms^{-1})	(Jykms^{-1})	($10^8\,L'$)	($10^8\,M_\odot$)
(1)	(2)	(3)	(4)	(5)	(6)	(7)	(8)	(9)
CGCG 465-012N	AOS	320	148	28.29 ± 1.01	69.32 ± 2.48		14.1 ± 0.504	8.47 ± 0.302
CGCG 465-012S	AOS	300	136	60.63 ± 1.18	148.6 ± 2.9		30.2 ± 0.588	18.1 ± 0.353
IRAS 03582+6012	AOS	520	211	40.76 ± 1.01	99.86 ± 2.48		38.4 ± 0.951	23 ± 0.571
IRAS 04271+3849	AC45	520	255	35.37 ± 2.39	86.65 ± 5.85		13.1 ± 0.883	7.85 ± 0.53
NGC 1797F	SAM45			< 26.66	< 65.31		< 6.14	< 3.69
NGC 1797	SAM45	370	257	23.37 ± 3.17	57.27 ± 7.78		5.39 ± 0.732	3.23 ± 0.439
CGCG 468-002S	SAM45			< 24.53	< 60.10		< 8.45	< 5.07
CGCG 468-002N	AC45			< 24.33	< 59.60		< 8.38	< 5.03
IRAS 05083+2441S	SAM45	320	389	14.17 ± 2.03	34.72 ± 4.97		7.8 ± 1.12	4.68 ± 0.67
IRAS 05129+5128	SAM45	300	361	31.05 ± 2.90	76.08 ± 7.09		24.7 ± 2.3	14.8 ± 1.38
IRAS F05187-1017	SAM45	685	515	34.64 ± 3.22	84.87 ± 7.89		28.4 ± 2.64	17.1 ± 1.59
IRAS 05223+1908	SAM45			< 20.50	< 50.22		< 18.4	< 11.1
MCG +08-11-002	AC45	500	378	22.57 ± 2.36	55.29 ± 5.78		8.95 ± 0.935	5.37 ± 0.561
UGC 03351	AC45	700	334	310.6 ± 5.7	760.9 ± 14.0		77.1 ± 1.42	46.3 ± 0.853
IRAS 05442+1732	AOS	340	226	61.16 ± 2.06	149.84 ± 5.05		22.5 ± 0.758	13.5 ± 0.455
UGC 03410N	SAM45	665	586	108.3 ± 9.4	265.2 ± 22.9		22.2 ± 1.92	13.3 ± 1.15
UGC 03410S	SAM45	480	344	54.64 ± 5.87	133.9 ± 14.4		11.2 ± 1.21	6.73 ± 0.724
IRAS 07251-0248	SAM45	340	293	15.56 ± 2.00	38.12 ± 4.89		116 ± 14.9	69.6 ± 8.92
NGC 2623	SAM45	500	230	39.21 ± 2.86	96.07 ± 7.00	161.3[b]	15.7 ± 1.15	9.44 ± 0.687
IRAS F09111-1007W	SAM45	390	303	25.01 ± 1.65	61.28 ± 4.03		77.4 ± 5.1	46.5 ± 3.06
IRAS F09111-1007E	SAM45	635	596	20.88 ± 1.99	51.15 ± 4.87		64.6 ± 6.15	38.8 ± 3.69

Table 2.2: Result of the single-point observation

Galaxies	Backend	ΔV_0 (kms^{-1})	ΔV_{FWHM} (kms^{-1})	I_{CO} (Kkms^{-1})	$S_{\mathrm{CO}}\Delta V$ (Jykms^{-1})	$S_{\mathrm{CO}}\Delta V$(ref) (Jykms^{-1})	L'_{CO} ($10^8\,L'$)	$M_{\mathrm{H_2}}$ ($10^8\,M_\odot$)
(1)	(2)	(3)	(4)	(5)	(6)	(7)	(8)	(9)
UGC 05101	SAM45	930	839	57.71 ± 3.94	141.4 ± 9.7	75.5[a]	96.5 ± 6.59	57.9 ± 3.95
MCG +08-18-013S	SAM45			< 22.84	< 55.95		< 17.3	< 10.4
MCG +08-18-013N	SAM45	180	216	22.56 ± 1.59	55.26 ± 3.89		17.1 ± 1.21	10.3 ± 0.724
IRAS F10173+0828	SAM45	390	346	16.66 ± 1.70	40.83 ± 4.16	63.0[c]	43.4 ± 4.42	26 ± 2.65
IRAS F10173+0828F	SAM45			< 17.22	< 42.20		< 44.9	< 26.9
CGCG 011-076F	SAM45	390	286	13.56 ± 1.83	33.23 ± 4.47		10.3 ± 1.39	6.2 ± 0.835
CGCG 011-076	SAM45	480	389	39.84 ± 2.00	97.62 ± 4.90		30.4 ± 1.53	18.2 ± 0.915
IC 2810W	SAM45	505	460	15.88 ± 1.96	38.91 ± 4.81	101.5[c]	21.2 ± 2.62	12.7 ± 1.57
IC 2810E	SAM45	605	354	17.00 ± 1.65	41.65 ± 4.03		22.7 ± 2.2	13.6 ± 1.32
NGC 4194	SAM45	410	184	59.72 ± 3.11	146.3 ± 7.6	143.5[c]	6.45 ± 0.336	3.87 ± 0.202
IRAS F12224-0624	SAM45	210	142	6.76 ± 1.38	16.57 ± 3.39		5.86 ± 1.2	3.51 ± 0.719
NGC 4418	SAM45	410	120	48.39 ± 3.66	118.6 ± 9.0	164.5[c]	3.78 ± 0.286	2.27 ± 0.171
NGC 4418F	SAM45	400	210	60.08 ± 12.66	147.2 ± 31.0		4.69 ± 0.989	2.82 ± 0.593
Mrk 231	SAM45	815	194	45.24 ± 2.05	110.8 ± 5.0	56.0[c]	88.3 ± 4	53 ± 2.4
UGC 08387	SAM45	475	369	79.32 ± 2.66	194.3 ± 6.5	177.2[b]	53.7 ± 1.8	32.2 ± 1.08
Mrk 273	SAM45	675	591	24.46 ± 2.32	59.94 ± 5.68	80.5[c]	39.3 ± 3.72	23.6 ± 2.23
CGCG 247-020	SAM45	235	88	12.66 ± 1.69	31.03 ± 4.13		10.1 ± 1.35	6.08 ± 0.809
IRAS F14348-1447	SAM45	410	280	15.29 ± 1.46	37.45 ± 3.58	59.5[c]	108 ± 10.3	64.9 ± 6.19
CGCG 049-057	SAM45	465	288	61.34 ± 4.92	150.3 ± 12.0	119.0[c]	15.1 ± 1.21	9.07 ± 0.727
Arp 220	SAM45	760	468	84.64 ± 4.21	207.4 ± 10.3	329.0[c]	37.1 ± 1.85	22.3 ± 1.11
IRAS F17207-0014	SAM45			< 19.18	< 46.99	212.7[a]	< 39.7	< 23.8

Table 2.2: Result of the single-point observation

Galaxies	Backend	ΔV_0	$\Delta V_{\rm FWHM}$	$I_{\rm CO}$	$S_{\rm CO}\Delta V$	$S_{\rm CO}\Delta V$(ref)	$L'_{\rm CO}$	$M_{\rm H_2}$
		(kms^{-1})	(kms^{-1})	(Kkms^{-1})	(Jykms^{-1})	(Jykms^{-1})	($10^8\,L'$)	($10^8\,M_\odot$)
(1)	(2)	(3)	(4)	(5)	(6)	(7)	(8)	(9)
UGC 11041	AOS	280	106	20.49 ± 0.97	50.21 ± 2.38		7.03 ± 0.334	4.22 ± 0.2
CGCG 141-034	AOS			< 11.20	< 27.43		< 5.52	< 3.31
CGCG 142-034S	AOS			< 9.85	< 24.13		< 4.33	< 2.6
CGCG 142-034N	AC45			< 14.53	< 35.61		< 6.39	< 3.84
MCG +04-48-002S	SAM45	780	651	15.12 ± 2.38	37.06 ± 5.84	187.5[a]	3.58 ± 0.564	2.15 ± 0.339
MCG +04-48-002N	SAM45	600	402	48.02 ± 3.63	117.7 ± 8.9		11.4 ± 0.86	6.83 ± 0.516
IRAS 20351+2521	AOS	250	96	15.98 ± 0.87	39.15 ± 2.13		19.8 ± 1.07	11.9 ± 0.645
CGCG 448-020	AOS	440	104	16.33 ± 0.90	40.00 ± 2.21		22.8 ± 1.26	13.7 ± 0.757
ESO 602-G025	AOS	500	180	61.89 ± 2.51	151.64 ± 6.14		41.7 ± 1.69	25 ± 1.01
UGC 12150	SAM45	650	364	55.53 ± 2.48	136.06 ± 6.07		27.3 ± 1.22	16.4 ± 0.731
IC 5298	SAM45	519	281	26.01 ± 1.89	63.72 ± 4.63	84.0[c]	20.3 ± 1.48	12.2 ± 0.886
NGC 7752S	SAM45	360	260	17.46 ± 1.42	42.77 ± 3.49		5.39 ± 0.44	3.23 ± 0.264
NGC 7752N	SAM45	860	563	32.14 ± 3.74	78.74 ± 9.17		9.92 ± 1.15	5.95 ± 0.693
NGC 7771N	SAM45	340	136	47.64 ± 3.18	116.7 ± 7.8		10.2 ± 0.683	6.15 ± 0.41
NGC 7771S2	SAM45	320	153	18.91 ± 1.70	46.32 ± 4.17		4.07 ± 0.366	2.44 ± 0.22
NGC 7771S1	SAM45	720	239	132.0 ± 3.4	323.3 ± 8.4	380.5[b]	28.4 ± 0.74	17 ± 0.444
Mrk 331	SAM45	475	80	18.36 ± 3.58	44.99 ± 8.78	346.4[a]	6.55 ± 1.28	3.93 ± 0.767

The columns are as follows: Col. (1): Galaxy name. Col. (2): Spectrometer used in our CO observation. Col. (3): Full velocity width at zero intensity of the CO emission line. Col. (4): Full velocity width at half maximum of the CO line. Col. (5): CO intensity on the temperature scale of $T_{\rm mb}$. Col. (6): CO flux from the beam. A conversion factor from K to Jy is $2.45\,{\rm JyK}(T_{\rm mb})^{-1}$ per a beam. Col. (7): CO flux in the literatures, the superscript represents the

literature (a = GS04, b = Young et al. (1995) and c = SSS91). Conversion factors from K to Jy are 4.95 JyK$(T_{\rm mb})^{-1}$, 42 JyK$(T_A^*)^{-1}$ and 35 JyK$(T_R^*)^{-1}$ for the IRAM 30 m telescope, FCRAO 14 m telescope (Young et al., 1995) and NRAO 12 m telescope (the NRAO 12 m User's Manual 1990 edition, Fig. 14.), respectively. For 14 m observations in the T_R^* scale, 3.15 JyK(T_R^*) is used assuming $\eta_{\rm fss} = 0.75$. Col. (8): CO luminosity, Col. (9): Molecular gas mass. The symbol of '<' indicates the upper limit.

2.4 Comparison of Flux with the Previous Observations

Here we compare our observed CO flux with previous observations GS04, Solomon et al. (1997), Young et al. (1995) and Sanders et al. (1991), which used smaller diameter telescopes of 12 m, 14 m and 30m with beam sizes of 55″, 45″ and 22″, respectively. Twenty-four galaxies in our sample have a total of 43 entries in the literature. In case of multiple entries in the literature, we use values from smaller aperture telescopes, and in case more than one value is found for a telescope with the same aperture, we list the result from the most recent observation. For UGC 08387, the value from FCRAO 14 m (Young et al., 1995) is used as a reference instead of NRAO 12 m (SSS91) for the purpose of the CO size estimation in Chapter 3, as the 12 m measured a flux that was smaller than the 45 m measurement.

Figure 2.8 shows the comparison of the CO flux between this work and the references. The flux of this work are on average 16 ± 14 % lower than those of the NRAO 12m observations while are on average nearly equal to those of the IRAM 30m observations. The flux of our observation are on average 23 ± 14 % lower than those of the FCRAO 14 m observations if we exclude 3 ULIRGs and NGC 1275, whose $\Delta V_{\rm FWHM}$ is substantially different between 538 kms^{-1} of our observation and 70 kms^{-1} of Young et al. (1995). This systematic decrease is because of the difference of the projected beam sizes of the telescopes. The 12 m and 14 m telescopes capture the total flux of a galaxy. The projected radii are 13 kpc and 11 kpc at 97 Mpc for the 12 m and 14 m telescopes, respectively, and are enough large compared to the typical size of CO distributions in galaxies. The Galaxy has the extended CO distribution up to a radius of $\sim$ 10 kpc (Nakanishi & Sofue, 2006). The spiral galaxies in the Virgo cluster have the CO emitting regions of radii from 5.5 kpc to 13.3 kpc (Nakanishi, 2005). Thus the 12 m and 14 m telescopes capture the total flux of a galaxy. On the other hand, the NRO45 and the 30 m telescope observes flux from only the central region. The flux between NRAO 12m and FCRAO 14m are not significantly different. The flux ratio of our flux to the 12 m and 14 m observations are within errors. The difference between the averaged flux fractions, 16 % and 23 %, is due to sampling compared sources.

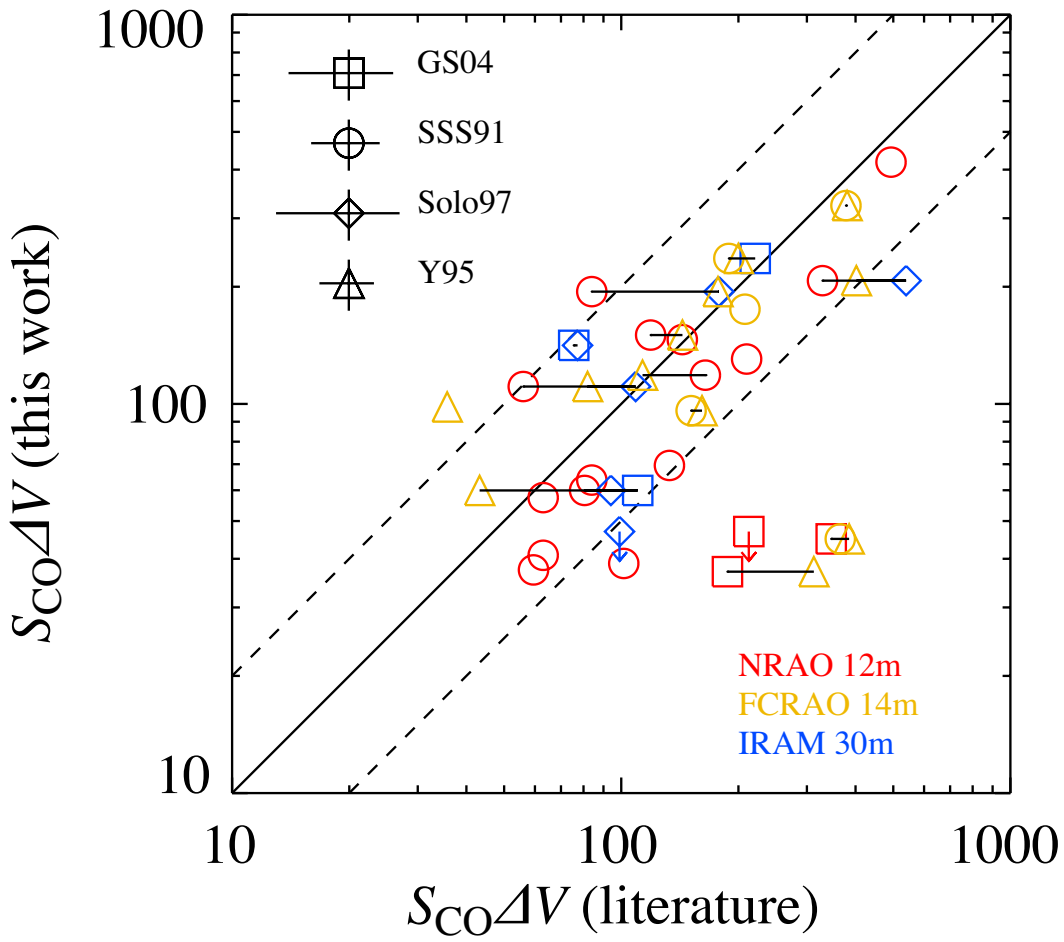

FIGURE 2.8: The comparison of the CO flux of this work with NRO45 and the literature values in GS04 (square), SSS91 (circle), Solomon et al. (1997) (diamond), and Young et al. (1995) (triangle). The color represents the employed telescope: NRAO 12 m (red), FCRAO 14 m (orange) and IRAM 30 m (blue). The typical errors in each observation are shown on the upper-left. The arrow means an upper limit of flux. The horizontal solid line is connecting each points of an identical galaxy but different observations. The solid and dotted lines represent where the flux of our observations is corresponding to the flux of the literatures and is shifted by a factor of 2, respectively.

Chapter 3

Merger-Driven Gas Inflow

3.1 Introduction

Mergers and interactions can efficiently drive radial gas flows towards the galactic center (Barnes & Hernquist, 1996; Mihos & Hernquist, 1996), and such fueling of gas into the central region is also important for igniting the SB or/and growth of the black-hole. Interferometric results show a concentrated molecular gas disk in the central sub-kpc region at advanced stages of interactions (Downes & Solomon, 1998; Bryant & Scoville, 1999; Xu et al., 2015, 2014). There are few direct observations of molecular gas inflow in interacting galaxies. Iono et al. (2004, 2005) observed velocity components of possibly indicating gas inflow in two interacting galaxies using CO position-velocity diagrams.

Numerical simulations of interacting/merging galaxies confirm that gas in the outer regions contribute little to the enhancement of the total star formation rate and efficiency in merging galaxies (Cox et al., 2008), and show that gas in the inner disk inflows towards the galactic center and then accumulates within a region of several kiloparsecs in scale (radius of 3.5 - 5.3 kpc) before the final coalescence (Iono et al., 2004).

Observationally, however, it is still uncertain whether radial gas inflow is a common phenomenon in merging LIRGs. To confirm this, spatially resolved information of gas on a large sample is required. Previous surveys exclusively employed small diameter telescopes with a large beam to derive the total flux of the whole galaxy, thus were unable to gain information on the spatial distribution of gas. Our selective measurement of gas in the central several kpcs in interacting/merging galaxies can provide information on gas that has undergone such inflow. The NRO45 has the the beam size of 15″ at the frequency of CO. It corresponds to a projected scale of 3.4 kpc radius at 94 Mpc which is a median distance of our sample.

3.2 Merger-driven Molecular Gas Inflow

3.2.1 The Molecular Gas Mass in the Central Region and Merger Process

Gao & Solomon (1999) find that *total* molecular gas mass of LIRGs and ULIRGs decrease with decreasing separation between the two nuclei. This decrease in mass is interpreted as the consumption of molecular gas by the interaction/merger induced starburst. This is consistent with theoretical predictions in which $\sim 70\,\%$ of the initial gas content is consumed in a major merger (Cox et al., 2008).

Our observations allow us to statistically investigate the supply and the consumption of the gas in the central region ($r \sim 3.4\,\mathrm{kpc}$, see Figure 2.2) along the merger process. While the total molecular gas in the whole galaxy decreases, if molecular gas inflow is common in our sample, we expect the molecular gas in the central region to either be constant or increasing, to sustain the high SFR during the interaction/merger.

We classify our sources into three stages of merger instead of the five stages in Section 2.1 in order to secure the number of sources at each stage. The original five stages are binned into the three stages as follows: the non-merger (N) remains as the non-merger (0), the original pre-merger (a) and early stage merger (b) are combined as early stage (1), and original mid-stage merger (c) and late stage merger (d) are also combined as late stage (2). Haan et al. (2011) investigated the merging timescales of a sub-sample in the GOALS sample and reported a timescale of 0.3 – 1.3 Gyr until the nuclei merge for interacting GOALS galaxies. Thus we can estimate the dynamical timescale between the early stage and late stage to be approximately 1 Gyr.

Figure 3.1 shows the molecular gas mass in the central region at each merger stage. In this diagram, we also plot the median values among sources detected in CO with $\log\left(L_{\mathrm{IR}}/L_{\odot}\right) \geq 11.0$. We find a constant trend of the molecular gas mass from the early stage to the late stage in our sample. The result of a Kolmogorov-Smirnov (K-S) test indicates a p-value of 0.66 between the distributions of the early stage and the late stage, and supports the constant molecular gas mass in the central region. Combined with the decline of the total molecular gas along the merger process, this can be interpreted as indicating a radial inflow of molecular gas which replenishes the molecular gas within the central kpc region, and that the supply balances the consumption by star formation over the timescale of the merger.

The observed constancy of molecular gas mass along the merger stage may be affected by a systematic bias in the the source distance as the function of the merger stage, as the area subtended by the telescope beam would thus be changed. Figure 3.2 shows the distribution of the projected radii at each stage. Almost all of the sources are within 2 kpc – 5 kpc, and no systematic dependence of the projected radii on the merger stage is present. Even if four sources with a particularly large projected radius of $\geq 7''$ are excluded from Figure 3.1, the median of the molecular gas mass is still constant.

A systematic dependence of $\alpha_{\rm CO}$ on the merger stage can also affect the molecular gas mass at each merger stage. In order for the $\alpha_{\rm CO}$ to account for the observed constant trend of molecular gas mass, $\alpha_{\rm CO}$ would have to change systematically by a factor of 4.5 from the early stage to the late stage, bringing down the median gas mass in the late stage below the 3σ spread of the early stage. Considering the discussion in Chapter 1.3.2, this large change in $\alpha_{\rm CO}$ is unlikely.

The unchanged molecular gas mass in the central region through the interaction/merger also means that this fueling process into the central several kpc regions runs at the same rate as the time-averaged SFR. Therefore we can roughly estimate the time-averaged rate of gas inflow $\langle \dot{M}_{\rm inflow} \rangle$ towards central several kpc regions from the time-averaged star formation rate $\langle {\rm SFR} \rangle$ over the interaction/merger timescale as,

$$\langle \dot{M}_{\rm inflow} \rangle \approx \langle {\rm SFR} \rangle. \tag{3.1}$$

Numerical simulations have predicted two starburst events during a merger (e.g., Mihos & Hernquist, 1996), which lasts $\sim 0.3 - 0.5$ Gyr each (Cox et al., 2008). Since the whole merger event lasts ~ 1 Gyr (Haan et al., 2011), we can estimate that the time-averaged SFR is on the order of the median value ($44\,M_{\odot}{\rm yr}^{-1}$) of the galaxies with $\log\left(L_{\rm IR}/L_{\odot}\right) \geq 11.0$ in our sample. Given large uncertainties, from Equation 3.1, we estimate $\langle \dot{M}_{\rm inflow} \rangle$ of $O(10)\,M_{\odot}{\rm yr}^{-1}$ in our sample. This rate is significantly larger than barred spiral galaxies $> 0.1 - 1\,M_{\odot}{\rm yr}^{-1}$ (Sakamoto et al., 1999). This implies that mergers efficiently transfer the molecular gas towards the central region compared to bars in spiral galaxies.

This estimate of the rate of merger-driven molecular gas inflow has large uncertainties because we do not know the true $\langle {\rm SFR} \rangle$. Moreover, other mechanisms involving flows of the molecular gas are possible, such as outflows by AGN (e.g., García-Burillo et al., 2014; Sakamoto et al., 2014; Cicone et al., 2014) or by the

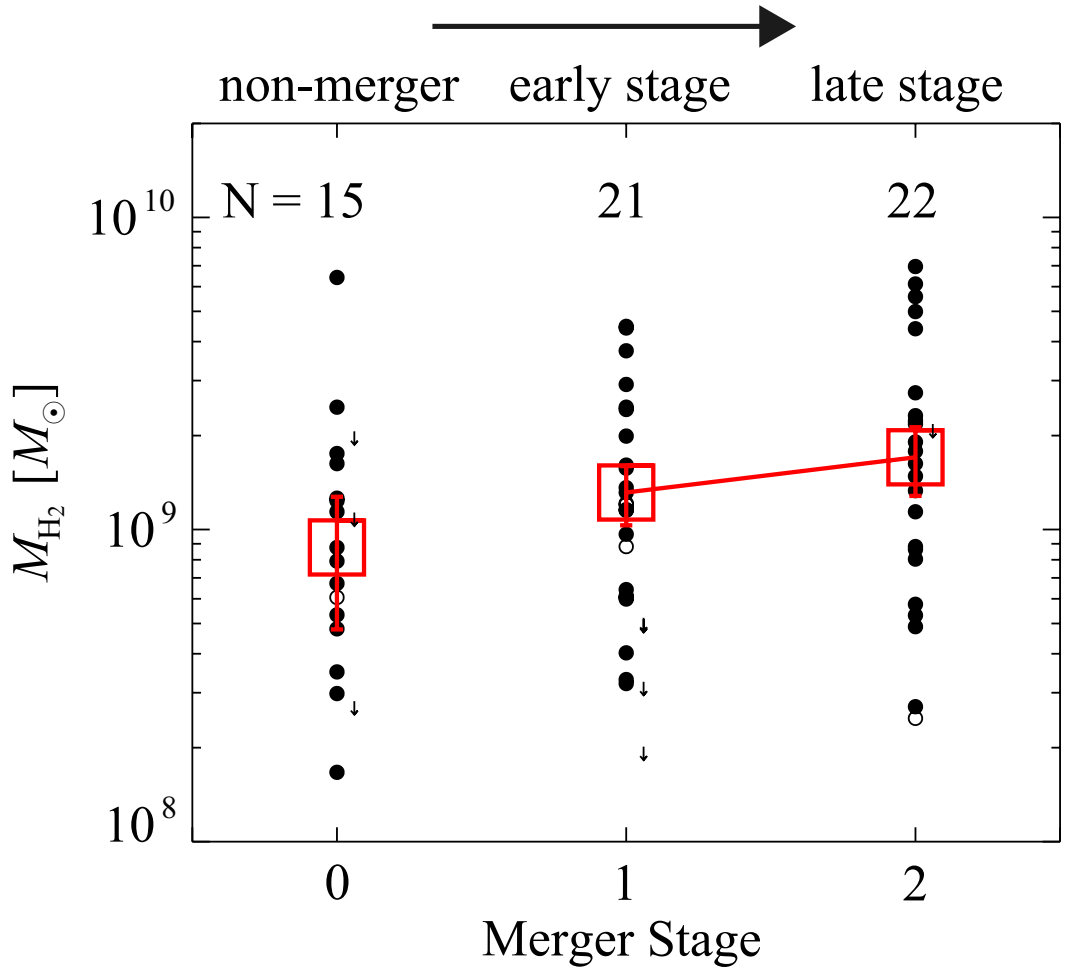

FIGURE 3.1: The molecular gas mass in the central region at each merger stages. The sources are grouped into 3 stages of merger: '0' = non-merger, '1' = early stage, '2' = late stage (see text for details). The filled and open circles mean the sources with $\log(L_{\rm IR}/L_\odot) \geq 11.0$ and $\log(L_{\rm IR}/L_\odot) < 11.0$, respectively. The arrows represent the non-detection sources with the upper limits of the molecular gas mass. The red squares indicate the median values of the detected sources with $\log(L_{\rm IR}/L_\odot) \geq 11.0$ at the each stages, whose numbers of sources are shown on the upside of the diagram.

large-scale wind by starburst (e.g., Walter et al., 2002; Cicone et al., 2014; Cazzoli et al., 2014), or the kinetic ejection due to interactions/mergers (Iono et al., 2004; Kapferer et al., 2005). The kinetic ejections hardly affect depletions of the molecular gas in the central region because it is effective mainly in the outer disk. The mass-loss rates by the AGN-driven outflow and the starburst outflow are estimated to be much more than the SFR, $> 50\,M_\odot{\rm yr}^{-1}$ (Cicone et al., 2014; García-Burillo

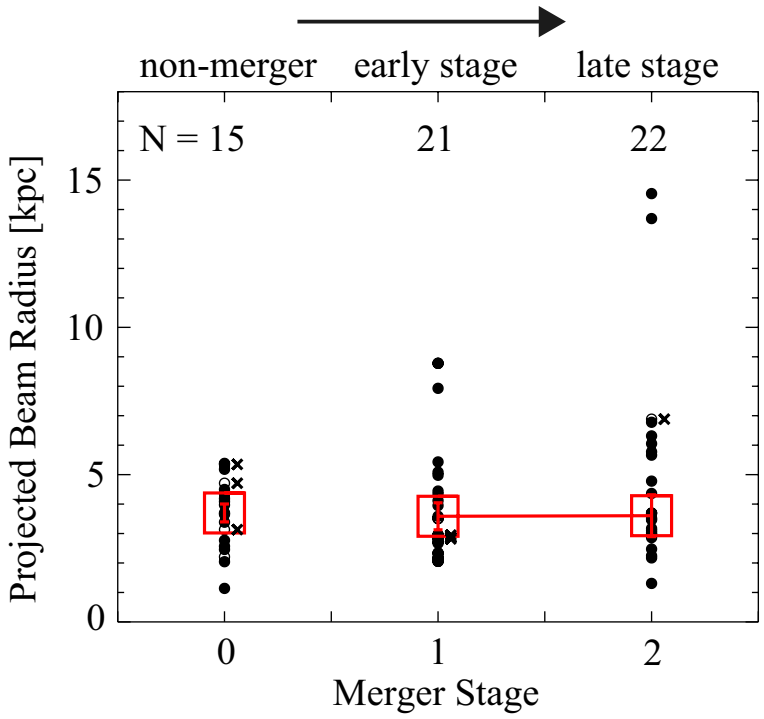

FIGURE 3.2: The projected beam radius of the sample at each merger stage. The symbols are the same as Figure 3.1 but the crosses indicate the non-detection sources.

et al., 2014; Sakamoto et al., 2014) on as large as its SFR (Cicone et al., 2014), respectively. Although the outflow could contribute to the reservoir decrease of the molecular gas, it is not clear if our local LIRGs have experienced the outflow and how long the outflow has continued in the merger timescale. However, AGN/starburst-driven outflows can, if any, remove the total molecular gas mass in gas depletion timescales of less than a few 100 Myr. The result in our study therefore means that on average there is more inflow to supply the molecular gas compared to the outflow, as well as the starburst, if the local LIRGs commonly experience outflows. In this case, the estimated value of the inflow rate indicates a lower limit.

3.3 CO Size and the Merger Stage

The distribution of molecular gas is a key to understanding the mechanism of star formation in interacting or merging galaxies. The gas inflow from the outer disk to the central region could downsize the extent of the CO distribution. Studies of molecular gas distribution in local LIRGs have been limited to interferometric observations, which report that almost all molecular gas is concentrated in the compact nuclear region (Downes & Solomon, 1998; Bryant & Scoville, 1999). Interferometers, however, can not retrieve extended components and may underestimate the extent of molecular gas. It is difficult to infer the gas distribution of local LIRGs by measurements of one single-dish telescope, since their beam sizes are normally large than the typical size scale of gas. In this section, we propose a new method to estimate the spatial extent of the CO distribution of our sources by comparing our flux to observations from the literature which used telescopes with different beam sizes. And the CO size of local LIRGs is examined at each stage of merger.

3.3.1 The Method to estimate the CO size

The size of the extent of the CO distribution, s, can be estimated by using the flux ratio of our flux at the NRO45 to the flux at the 12 m or 14 m telescope. The flux ratio is an observable value, and represents the ratio of the central flux convolved with the NRO45 beam to the total flux, because the flux from the 12 m or 14 m observations is considered to be the total flux of a galaxy due to their large beam sizes (see Chapter 2.4). The flux ratio of the flux within the 15″ beam to the flux within 55″ or 45″ beam is defined as,

$$R_{\rm CO} = \frac{S_{\rm CO}dV({\rm NRO45})}{S_{\rm CO}dV({\rm ref})} = \frac{\int I(\boldsymbol{r}, s) P_n(\boldsymbol{r})\, d\boldsymbol{r}}{\int I(\boldsymbol{r}, s)\, d\boldsymbol{r}}, \tag{3.2}$$

where $I(\boldsymbol{r}, s)$ is the radial CO intensity distribution which is characterized by the size s, $\boldsymbol{r}$ is the radius from the center of the galaxy on the sky, $P_n(\boldsymbol{r})$ is the normalized primary beam pattern of NRO45, and the integral is performed over whole a galaxy. The numerator is considered to be the total flux of the source. The denominator corresponds to the flux where the emitting region is convolved with $P_n(\boldsymbol{r})$ of the 15″ telescope beam. The $P_n(\boldsymbol{r})$ is approximated by a normalized axisymmetric Gaussian distribution with the beam size $\theta_{\rm mb} = 15''$ and is expressed

by,

$$P_n(\boldsymbol{r}) = \exp\left(-\frac{4\ln 2}{\theta_{\rm mb}^2} r^2\right). \tag{3.3}$$

The radial distribution of CO intensity can often be approximated by an exponential, Gaussian or uniform-disk distribution (e.g., Young et al., 1995; Nishiyama & Nakai, 2001). Here, we assume three intensity distribution profiles of the emitting region, the Gaussian distribution (Model A), the azimuthally symmetric exponential distribution (Model B), and the Uniform disk (Model C). These are represented as,

$$I_A(\boldsymbol{r}) = A\exp\left(-\frac{4\ln 2}{s_A^2} r^2\right), \tag{3.4}$$

$$I_B(\boldsymbol{r}) = A\exp\left(-\frac{\ln 2}{s_B} r\right), \tag{3.5}$$

$$I_C(\boldsymbol{r}) = A \quad (r < s_C, \text{ otherwise } 0), \tag{3.6}$$

where A is a constant. The s_A, s_B and s_C are the CO sizes for each model. For Model A and B, the CO sizes s_A and s_B are identical to the half width at the half maximum (HWHM). The s_C is the radius of the disk in Model C. As long as the center of the beam coincides with the center of the intensity distribution, that is, the observed position corresponds to the intensity peak, the flux ratio in Equation 3.2 is rewritten as,

$$R_{\rm CO} = \frac{\int_0^{2\pi}\int_0^{\infty} I_X(\boldsymbol{r}, s) P_n(\boldsymbol{r})\, r\, dr d\phi}{\int_0^{2\pi}\int_0^{\infty} I_X(\boldsymbol{r}, s)\, r\, dr d\phi} \tag{3.7}$$

where X is replaced by indices of Model A, B or C. By solving Equations 3.7 for s, we obtain the CO size. We can easily isolate s_A as follows,

$$s_A = 0.5\sqrt{\frac{1}{R_{\rm CO}} - 1}\,. \tag{3.8}$$

Model B and C cannot be solved analytically for s_B and s_C. We solve Model B and C numerically. The equations to be solved numerically are

Model B : (3.9)

$$R_{\rm CO} = \frac{(\ln 2)^2}{s_B^2} \exp\left(\frac{\theta_{\rm mb}\ln 2}{16 s_B^2}\right) \int_0^{\infty} \exp\left\{-\frac{4\ln 2}{\theta_{\rm mb}^2}\left(r + \frac{\theta_{\rm mb}^2}{8 s_B}\right)^2\right\} r\, dr \tag{3.10}$$

Model C : (3.11)

$$R_{\rm CO} = \frac{\theta_{\rm mb}^2}{4 s_C^2 \ln 2}\left\{1 - \exp\left(-\frac{2 s_C^2 \ln 2}{\theta_{\rm mb}^2}\right)\right\}. \tag{3.12}$$

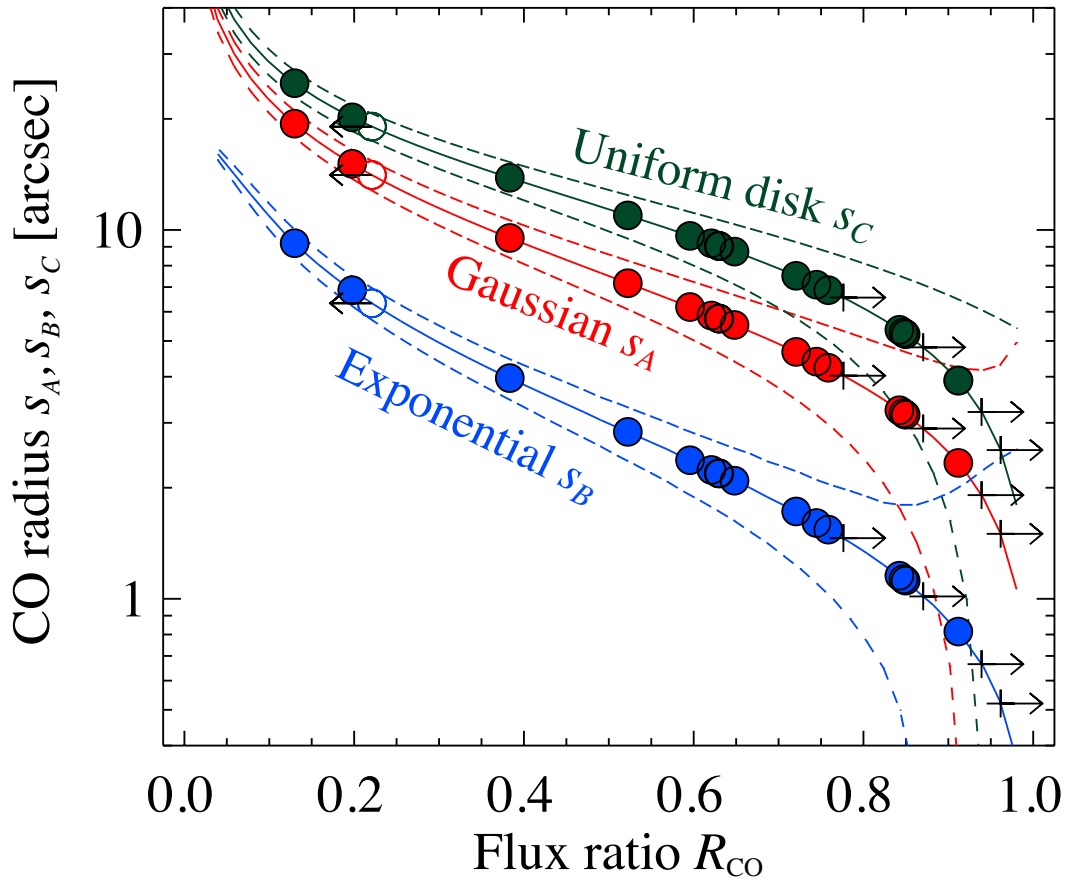

FIGURE 3.3: The angular CO radius s and the flux ratio (R_{CO}) of the sub-sample which can be estimated (see text). The CO radius s in y-axis represents s_A for the Gaussian model (Model A, red) and s_B for the exponential model (Model B, blue), and s_C for the radius for the uniform disk model (Model C, green). The solid and the dashed lines indicate the model curve of A, B and C, respectively. The right (left) arrow denotes the lower limit (upper limit) of R_{CO} and the upper limit (lower limit) of s.

The integration in Equation 3.10 was performed by using the IDL function `QROMO`.

3.3.2 The Estimate CO Size

Sizes of the CO distribution of a sub-sample are estimated using this method. The sub-sample is composed of 21 galaxies which have literature flux value of the 12 m or the 14 m telescopes and have the value of R_{CO} less than 1 within the 1σ uncertainty. For four galaxies with $R_{CO} \geq 1$ we cannot estimate s from R_{CO}

directly, and therefore we estimate only the 1σ upper limit of s by a way replacing $R_{\rm CO}$ in Equation 3.2 by $R_{\rm CO} - 1\sigma$. The flux ratio $R_{\rm CO}$ and the CO size s of the sub-sample are summarized in Table 3.1.

Figure 3.3 shows s as a function of $R_{\rm CO}$ for each of the models. The difference of s among three models increases from a factor of 2 around $R_{\rm CO}$ of 0.1, up to a factor of 5 near $R_{\rm CO}$ of 1. The error of the each model also increases with $R_{\rm CO}$, becoming greater than 100 % at $R_{\rm CO} \gtrsim 0.85$. The source IRASF 01417+1651 in all models, and IC 1623AB, NGC 0992 and NGC 7771S1 in Model B have the errors of more than 100 % in the estimated CO size. The accuracy of this method decreases rapidly for s of $\lesssim 2''$, $\lesssim 1''$ and $\lesssim 4''$ in Model A, B and C, respectively, because this method is not sensitive to CO distributions much smaller than the beam size of the single-dish observations.

The range of CO radii s of the sub-samples are range $2\farcs3$ – $19\farcs4$, $3\farcs7$ – $9\farcs8$ and $3\farcs9$ – $25\farcs0$ in Model A, B and C, respectively. Eight sources (38 % of the sub-sample) show compact distributions in Model B with $s_B \lesssim 1$. Figure 3.4 shows the CO radius on the physical scale S of the three models. The S ranges widely from 0.8 kpc to 11 kpc in Model A and from 1.3 kpc to 17 kpc in Model C. Meanwhile the all S_B in Model B settle within a narrow range from 0.3 kpc to 4 kpc. The median S of Model A, B and C are 2.6 kpc, 1.0 kpc and 4.1 kpc, respectively, excluding upper/lower limits. The majority of the sources, 14 sources (67 %) for Model A, 20 sources (95 %) for Model B, 13 sources (62 %) for Model C, have S of less than 4 kpc.

3.3.3 CO Size and Other Indicators

In order to verify this method to estimate the CO size, we compare s with sizes measured with interferometers. We summarize published interferometric data of CO (1–0) and CO (2–1) in Table 3.1. In 73 % of the objects, the estimated sizes in one or more models are consistent with interferometric measurements within the errors. The s_A is consistent with interferometric results for majority of the objects (64 %). This ensures the validness of this size-estimation. The sizes of two sources, NGC 4418 and IRAS F17207-0014, are inconsistent with the interferometric measurements. These sources have a very compact distribution of $< 1''$, for which our method is likely invalid.

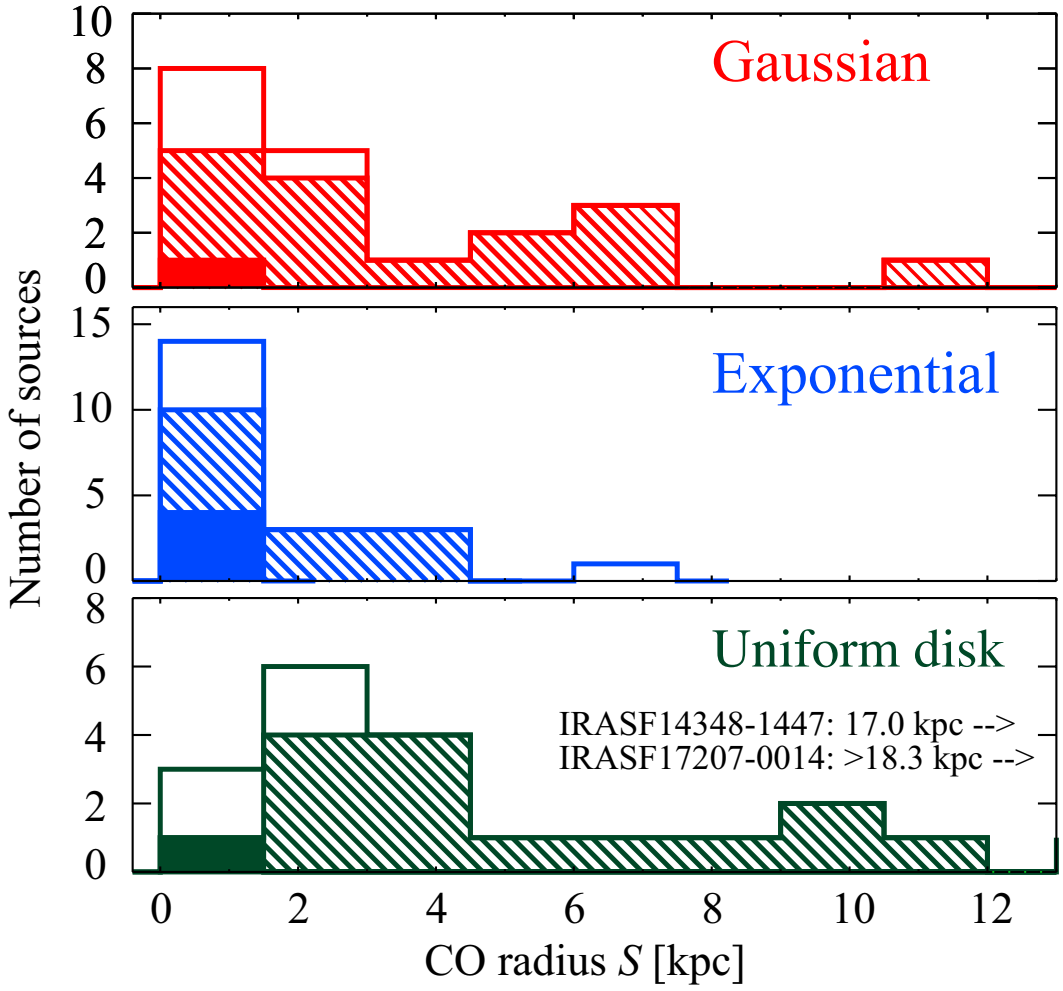

FIGURE 3.4: The CO radius S in unit of kpc of the sub-sample (see text). The three models are shown, the Gaussian model (the upper panel, red), the exponential model (the middle panel, blue), and the uniform disk model (the lower panel, green). The values of the upper limit and the lower limit are also shown by the bland box on the shaded box. The sources with the large error over 100 % are showed as the filled box. IRAS F14348-1447 and IRAS F17207-0014 are out of the range in the lower diagram of the uniform disk model due to their large radius of 17.0 kpc and > 18.3 kpc, respectively.

TABLE 3.1: The estimated CO size

Galaxies	R_{CO}	A: Gaussian		B: Exponential		C: Uniform disk		Literature
		s_A ($''$)	S_A (kpc)	s_B ($''$)	S_B (kpc)	s_C ($''$)	S_C (kpc)	s ($''$)
IC1623AB	0.847	3.18 ± 2.48	1.32 ± 1.03	1.13 ± 1.61	0.47 ± 0.67	5.26 ± 3.53	2.18 ± 1.46	$4^{a,1}$, $7.5{\times}4^{d,2}$
IRASF01417+1651	0.912	2.34 ± 3.15	1.35 ± 1.82	0.81 ± 2.8	0.47 ± 1.61	3.9 ± 4.05	2.25 ± 2.34	
NGC0695	< 0.939	< 1.91	< 1.29	< 0.67	< 0.45	< 3.21	< 2.16	
NGC0992	0.842	3.24 ± 2.45	0.91 ± 0.69	1.15 ± 1.53	0.32 ± 0.43	5.36 ± 3.49	1.51 ± 0.98	
UGC02238	0.621	5.86 ± 1.85	2.63 ± 0.83	2.23 ± 0.75	1.00 ± 0.33	9.20 ± 2.70	4.12 ± 1.21	$6.0^{j,3}$
IRASF03359+1523	0.522	7.17 ± 1.79	5.28 ± 1.32	2.84 ± 0.74	2.09 ± 0.54	11.0 ± 2.56	8.07 ± 1.89	
NGC2623	0.596	6.18 ± 1.58	2.52 ± 0.64	2.38 ± 0.64	0.97 ± 0.26	9.64 ± 2.27	3.93 ± 0.92	$0.9{\times}0.75^{g,4}$, $1.34^{j,3}$
IRASF10173+0828	0.648	5.53 ± 1.88	6.00 ± 2.04	2.09 ± 0.75	2.27 ± 0.82	8.73 ± 2.76	9.49 ± 3.00	$< 3.6^{c,5}$
IC2810W	0.383	9.51 ± 1.84	7.24 ± 1.40	3.96 ± 0.80	3.02 ± 0.61	13.9 ± 2.52	10.5 ± 1.91	
NGC4194	< 0.776	< 4.03	< 0.84	< 1.46	< 0.30	< 6.55	< 1.37	$2.1{\times}1.25^{h,6}$, $7.7^{j,3}$
NGC4418	0.721	4.67 ± 2.00	0.83 ± 0.35	1.73 ± 0.82	0.31 ± 0.15	7.51 ± 2.95	1.33 ± 0.52	$0.35^{i,7}$
UGC08387	< 0.87	< 2.89	< 1.54	< 1.01	< 0.54	< 4.80	< 2.56	$2.54^{j,8}$, $1.36^{f,9}$
Mrk273	0.745	4.39 ± 2.05	3.69 ± 1.72	1.61 ± 0.85	1.35 ± 0.71	7.11 ± 3.04	5.96 ± 2.55	$3.45{\times}1.7^{e,10}$, $< 1.1^{e,11}$, $0.58^{f,9}$
IRASF14348-1447	0.629	5.76 ± 1.85	10.8 ± 3.47	2.19 ± 0.75	4.11 ± 1.40	9.06 ± 2.72	17.0 ± 5.1	
CGCG049-057	< 0.962	< 1.50	< 0.48	< 0.52	< 0.16	< 2.53	< 0.80	$< 1.8^{c,5}$
Arp220	0.630	5.74 ± 1.86	2.45 ± 0.79	2.18 ± 0.75	0.93 ± 0.32	9.04 ± 2.72	3.85 ± 1.16	$0.7{\times}0.95^{b,11}$, $3.5{\times}2.5^{b,10}$, $1.4^{f,9}$
IRASF17207-0014	> 0.221	> 14.1	> 13.5	> 6.32	> 6.07	> 19.1	> 18.3	$< 1.0^{c,5}$, $0.7^{f,12}$
MCG+04-48-002S	0.198	15.1 ± 3.08	4.70 ± 0.96	6.86 ± 1.33	2.14 ± 0.41	20.2 ± 4.49	6.29 ± 1.4	
IC5298	0.759	4.23 ± 2.09	2.44 ± 1.21	1.54 ± 0.88	0.89 ± 0.50	6.86 ± 3.09	3.96 ± 1.78	
NGC7771S1	0.850	3.15 ± 2.16	0.94 ± 0.64	1.12 ± 1.25	0.33 ± 0.37	5.22 ± 3.08	1.55 ± 0.91	
Mrk331	0.130	19.4 ± 3.7	7.46 ± 1.40	9.20 ± 1.63	3.54 ± 0.63	25.0 ± 5.48	9.61 ± 2.11	
Average	0.627	6.59	3.78	2.69	1.51	9.81	5.73	
Median	0.639	5.66	2.63	2.14	1.00	8.89	4.12	
Minimum	0.130	2.34	0.83	0.82	0.31	3.91	1.33	
Maxmum	0.912	19.4	10.8	9.21	4.11	25.0	17.0	

The CO radius s is estimated from flux ratio R_{CO} between two observations with different telescopes. The galaxies with $R_{CO} < 1$ are listed. If $R_{CO} - \sigma < 1$ for those with $R_{CO} \geq 1$, their $R_{CO} - \sigma < 1$ are listed and are used to estimate the upper limit of s. The columns are (1): the galaxy name. (2): the flux ratio of one of this observation to one of the literature. (3), (4): the CO size s_A and S_A in the Gaussian model (Model A). (5), (6): the CO size s_B and S_B in the azimuthally symmetric exponential model (Model B). (7), (8): the CO size s_C and S_C in the uniform disk model (Model C). (9): the CO radius measured with interferometers. The alphabetical superscript represents the literature: a = Scoville et al. (1989), b = Scoville et al. (1991), c = Planesas et al. (1991), d = Yun et al. (1994), e = Yun & Scoville (1995), f = Downes & Solomon (1998), g = Bryant & Scoville (1999), h = Aalto & Hüttemeister (2000), i = Costagliola et al. (2013), j = Ueda et al. (2014). The notes for each interferometric radius is given as the superscript number: 1 = deconvolved source size, double sources, 2 = deconvolved source size, bar structure, 3 = CO(2-1), radius enclosing 80 % of the total flux, 4 = deconvolved core size, 5 = unresolved source, HWHM, 6 = extended component enclosing 33 % of the total flux, HWHM, 7 = CO(2-1), HWHM on circle-average Gaussian in the visibility, 8 = CO(3-2), radius enclosing 80 % of the total flux, 9 = CO(2-1), nuclear disk component, HWHM in Gaussian model fit, 10 = extended component, deconvolved radius, 11 = core component, deconvolved radius, 12 = HWHM in Gaussian model fit. The symbols of '<' and '>' indicate the upper or lower limit, respectively. The asterisk of Mrk 331 mean the uncertain CO fluxes as described in the note of Table 2.2. The statistics also is shown in the lower part except those with the upper/lower limit value.

For the Gaussian distribution, S_A corresponds to a radius where a half of total energy is included. The Galaxy has the 50 % of its molecular gas mass within the radius of ∼6 kpc (Sanders et al., 1984). The CO distributions of almost all of our sources are concentrated in a region more compact compared to the Galaxy. Young & Scoville (1982) report that the HWHM of two late-type spiral galaxies whose radial profile are fitted well by an exponential function which is similar to Model B is estimated to be approximately 4 kpc. Nishiyama et al. (2001) fit CO radial distributions in the outer disk regions of nearby spiral galaxies by an exponential function and estimate a HWHM of 2.3 ± 1.5 kpc on average. The median radius of S_B (1.0 kpc) is approximately a factor of 2-4 lower than spiral galaxies. The S_B of 17/21 sources are smaller than the spiral galaxies.

For sources whose interferometric data are unavailable, this estimate based on the Gaussian model predicts NGC 0992 and NGC 7771S1 to possess a compact distribution of the cold molecular gas ($\lesssim 1$ kpc). This could imply the presence of the nuclear molecular disk in these sources. Interferometric observations of some local LIRGs reveals that the molecular gas is concentrated towards the central 1 kpc (e.g., Downes & Solomon, 1998; Bryant & Scoville, 1999). On the other hand, our model also predicts that IRAS F03359+1523, IC 2810W, MCG+04-48-002S and Mrk 331 have molecular gas distribution extended over ~ 5 kpc.

Further we compare the estimated CO radius to the extent of the FIR continuum for model A. The FIR continuum traces the warm and cold dust in a galaxy. These dust grains are thought to be distributed globally in the same regions as the CO emitting molecular gas. We assess the extent of FIR continuum in the sub-sample from Spitzer/MIPS 70 μm images. We exclude IC 1623AB and IRAS F14348-1447 because the 70 μm images are not available. The HWHM of the point spread function (PSF) of the 70 μm image is 9″(MIPS Instrument Handbook version 3). The averaged HWHM are calculated for 19 sources whose 70 μm images are available. All of the sources except Mrk 273 have the HWHM larger than 9″, i.e., the dust is extended.

In order to compare the FIR extent with s as estimated using our method, we convolve s_A with a Gaussian function with the same HWHM as the PSF of the MIPS 70 μm. Figure 3.5 shows the the histogram of the ratio of the convolved s_A to the HWHM of the 70 μm of the 19 sources. All but three sources with a large ratio above 1.3 are distributed within the ratio of 1.0 ± 0.1. This implies that the accuracy of s estimation using this method is accurate to approximately ±10 %.

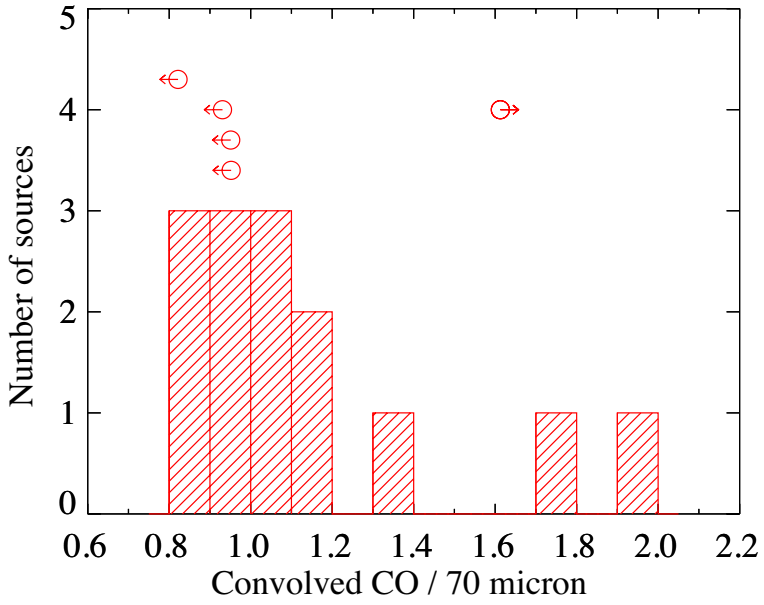

FIGURE 3.5: The histogram of the ratio of the convolved CO radius to the HWHM of MIPS 70 μm is shown. The CO radius s_A in the Gaussian model is used and is convolved by the Gaussian with the same FWHM as one of the PSF of MIPS 70 μm, 18″. The average ratio is 1.0 and the standard deviation is 0.1 except for IC2810W, MCG+04-48-002S and Mrk 331 whose ratios are larger than 1.3. Two sources, IC 1623AB and IRAS F14348-1447, are not included in the histogram because of no available data of MIPS 70 μm image. The upper or lower limits of the ratio are also plotted as the arrows above the histogram.

Very high CO-to-70 μm ratios observed in MCG +04-48-002S and Mrk 331 are likely due to uncertainties in the CO measurements. The upper limit of the ratios of the four sources with the upper limit of s are also plotted in the diagram. These sources seem to have the small distribution of the CO molecular gas compared to one of the warm/cold dust.

3.3.4 CO Size along Merger Sequence

In this sub-section, we examine the CO size S with the merger stage, which is the original objective. Figure 3.6 shows the CO size of the sources and its median values at each merger stage. Errors in the median values are calculated by standard errors divided by square roots of the numbers of sources. We also show the CO size normalized by a radius in K_s-band image, $S_{\rm n}$ in Figure 3.6b. The

K_s-band radius is the geometric mean of half-light radii between a major axis and a minor axis, which is taken from the 2MASS Extended Source Catalog (Skrutskie et al., 2006).

In all three models (Model A-C), the median values of S and $S_{\rm n}$ decrease by a factor of $\gtrsim 2$. S shrinks from 5.4 kpc at the early stage to 2.6 kpc at the late stage in Model A, from 2.2 kpc to 1.0 kpc in Model B, and from 7.9 kpc to 4.0 kpc in Model C. The time-averaged shrink velocity of the molecular gas distribution is estimated to be approximately $1 - 3\,{\rm km\,s^{-1}}$ from the early stage to the late stage. This trend still holds even if the sources with large errors in the CO size S (see Section 3.3.2) are removed from the sample in the diagram.

The result of the compact CO distribution in the late stage mergers is consistent with the trend of the merger-driven gas inflow discussed in the previous section. Therefore this trend may imply that the inflow of the molecular gas from the outer disk towards the central region is a common characteristic in merging LIRGs. The gas inflow and the consequent compact CO distribution may yield a nuclear starburst. This is consistent with local LIRGs at the late stage of mergers having a compact MIR distribution compared to those at the earlier stages (Díaz-Santos et al., 2010).

The CO size s of the non-mergers are the smallest among the three classes of mergers. In the molecular gas mass distributions, the KS test for the non-mergers shows p-values of 0.53 and 0.13 against the early stage mergers and the late stage mergers, respectively. It is not rejected that the non-mergers are from a same population of the early stage mergers and the late stage mergers. From our results, the non-mergers seem to have centrally concentrated, dense molecular gas. Haan et al. (2011) report that non-mergers in the GOALS galaxies with $L_{\rm IR} \geq 10^{11.4}\,L_{\odot}$ have the most luminous bulge, largest bulge radius and largest bulge Sérisic index compared to other merger stages. These non-merger LIRGs may be radiating their IR by a different mechanism from the merging LIRGs.

3.4 Summary of Chapter 3

The CO was observed with a single beam towards the central regions using NRO45 (Chapter 2). In this Chapter, using the obtained CO data, we address the question whether the gas inflow is common in merging LIRGs.

We propose a new method to estimate the extent of the CO distribution using our measurements of the molecular gas in the central region and the measurements of the total molecular gas. We assume three models of CO spatial distributions (Gaussian, exponential, and uniform disk). The median values of the CO radii are 2.6 kpc, 1.0 kpc and 4.1 kpc in the Gaussian, exponential and uniform disk models, respectively. The majority of the galaxies have the CO radii of $\lesssim 4$ kpc in all models. Despite the low spatial resolutions (FWHM=15″, 45″, 55″) of the single-dish telescopes used, the estimated CO sizes are consistent with interferometric measurements for most of the sources with available interferometric data. We note that our estimation is inaccurate for compact sources with $s \lesssim 1''$.

We examine the molecular gas mass in the central region of local LIRGs at each merger stage. We find that the median values of the molecular gas mass in the central region are constant from the early stage to the late stage of merger. This statistically supports a scenario where molecular gas inflow into the central region to replenish the molecular gas consumed by the starbursts is common in merging LIRGs. The CO size decreases from the early stage to the late stage of merger by a factor of $\geqq 2$. This might imply a gas inflow from the outer disk towards the central region. Assuming that the supply and the consumption of the molecular gas in the central region are balanced, the time-averaged inflow rate of the gas inflow into central kpc regions is roughly estimated to be $O(10)\,M_{\odot}\mathrm{yr}^{-1}$. The value is significantly larger than the inflow rate in barred spiral galaxies.

The observation of the molecular gas mass in the central region of local LIRGs shows signatures of merger-driven inflow of the molecular gas in merging LIRGs to be common. ALMA should enable detection of inflows and quantification through direct imaging.

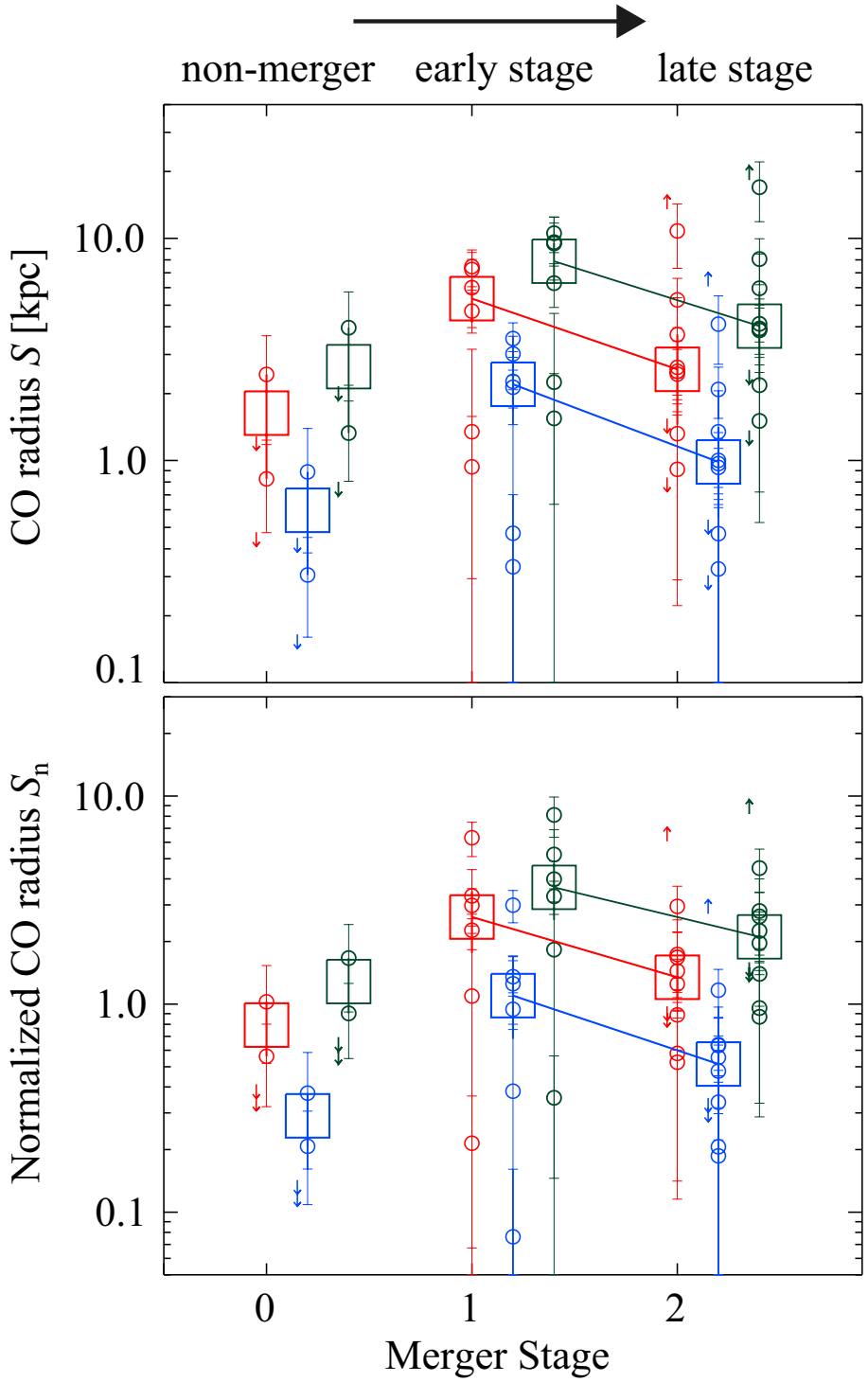

FIGURE 3.6: The CO size (a) and the normalized CO size (b) at the each merger stage of the sub-sample. The each of the CO size and the normalized CO size are colored the same color scheme as Figure 3.3 and are slightly shifted in one merger stage. The circles, fine vertical bars and arrows mean the data values, the errors and the upper/lower limit values, respectively. The squares and the vertical bold bars are the median values and its error, respectively.

Chapter 4

Star Formation along the Merger Sequence

4.1 Introduction

In this chapter, I investigate the relation between the star formation in the central region of local LIRGs and its merger stage. In the previous chapter, I discussed gas inflow, which can result in nuclear starbursts and possibly fuel the AGN. The central region of galaxies is the site of intense activities characterizing local LIRGs, such as nuclear SB and/or AGN. A substantial fraction of MIR radiation associated with nuclear SB or AGN originates from a compact, sub-kpc region (Soifer et al., 2000, 2001). Selectively observing the central regions can help to highlight these characteristics.

Many numerical simulations predict greatly varying SFR histories of merging galaxies along time (Barnes & Hernquist, 1996; Mihos & Hernquist, 1996; Cox et al., 2008). However, star formation along the merger sequence is observationally unclear, although there are some evidence constraining the star formation history of mergers. LIRGs are generally located at the two stages of the first passage and the final coalescence, while almost all ULIRGs are at the final coalescence stage (Murphy et al., 2001; Haan et al., 2011). The merging LIRGs at the late stage tend to have compact MIR emitting regions (Díaz-Santos et al., 2010) and concentrated regions of molecular gas (Downes & Solomon, 1998). Merging/interacting galaxies tend to have high IR luminosity compared to isolated galaxies with comparable molecular gas mass and also have high dust temperature (Young et al., 1986b,a; Young & Scoville, 1991). Sanders et al. (1991) find, in their sample with a wide IR luminosity range $10 \leqslant \log(L_{\rm IR}/L_{\odot}) \leqslant 12$, a trend of high $L_{\rm IR}/M_{\rm H_2}$ ratio in advanced mergers. However, Dopita et al. (2002) observe no trend between the SFR of local LIRGs and merger stage, and they conclude that is likely due to long-lasting, enhanced star formation in mergers. Their interpretation, however, is inconsistent with recent results of merger simulations, which simulate repeated spiky enhancements in SFR (Cox et al., 2008; Saitoh et al., 2009).

4.2 Star Formation Rate

In this section, I estimate the SFR within the CO beam size of $15''$, instead of total SFR estimated from the total IR luminosity in Chapter 2, in order to compare the SFR with the observed CO in the central regions.

For dusty galaxies such as local LIRGs, the IR photometric luminosity is the best tracer to estimate the SFR because almost all star-forming regions in such galaxies are obscured by rich dust, so that UV and optical emission from the regions suffer from heavy extinction. The contribution of far UV to the SFR in the GOALS galaxies is estimated from GALEX and Spitzer observations to be only $\sim 4\,\%$ on the average (Howell et al., 2010).

The monochromatic $24\,\mu$m luminosity is generally used as the tracer of SFR in dusty star-forming galaxies, and has an advantage of an easier measurement than the bolometric IR luminosity. The $24\,\mu$m luminosity is dominated by hot dust continuum produced from small dust grains heated by young stars. Such grains are transiently heated to higher temperature $\gtrsim 100\,\mathrm{K}$ (Draine, 2003). The $24\,\mu$m continuum is contaminated by old stars not involved in the current star formation and therefore is a good tracer to estimate current SFR of galaxies. This is one of the strong merits of on measuring the SFR using $24\,\mu$m at every merger stages, which can be as short as a few hundred Myr.

4.2.1 Extent of Mid Infrared Emitting Region

The Spitzer/MIPS $24\,\mu$m image allows us to estimate individual SFRs even in close galaxy pairs thanks to the high spatial resolution and the wide field of view compared to IRAS observations or other photometric bands ($70\,\mu$m and $160\,\mu$m) of MIPS. However, although we need to obtain the SFR within the central region in order to compare with the central molecular gas mass of our galaxies, it is difficult to extract the $24\,\mu$m flux enclosed by a circular aperture of the radius of the same as the CO beam, $r = 7.5''$, because the $24\,\mu$m image do not distinctly resolve galaxies. Fortunately, the $24\,\mu$m images of almost all sources seem to be point-like. Thus I estimate the central SFR after confirming that the MIR emitting regions in other nearly wavelengths are more compact than the CO beam size.

In order to examine the size of the MIR emitting regions of the sample, I use the size of the $13.2\,\mu$m continuum which is measured from the Spitzer/IRS spectrogram by Díaz-Santos et al. (2010). The MIR size is parameterized by the FWHM of Gaussian fits to the spectrogram in the direction of the slit, where the slit length is $57''$ and the spatial resolution is $3\farcs6$ at $13.2\,\mu$m. Of all 79 sources, 67 sources have available data of the MIR size in Díaz-Santos et al. (2010). The sizes in 21 of the 67 sources are indicated by upper limits because the spectrograms

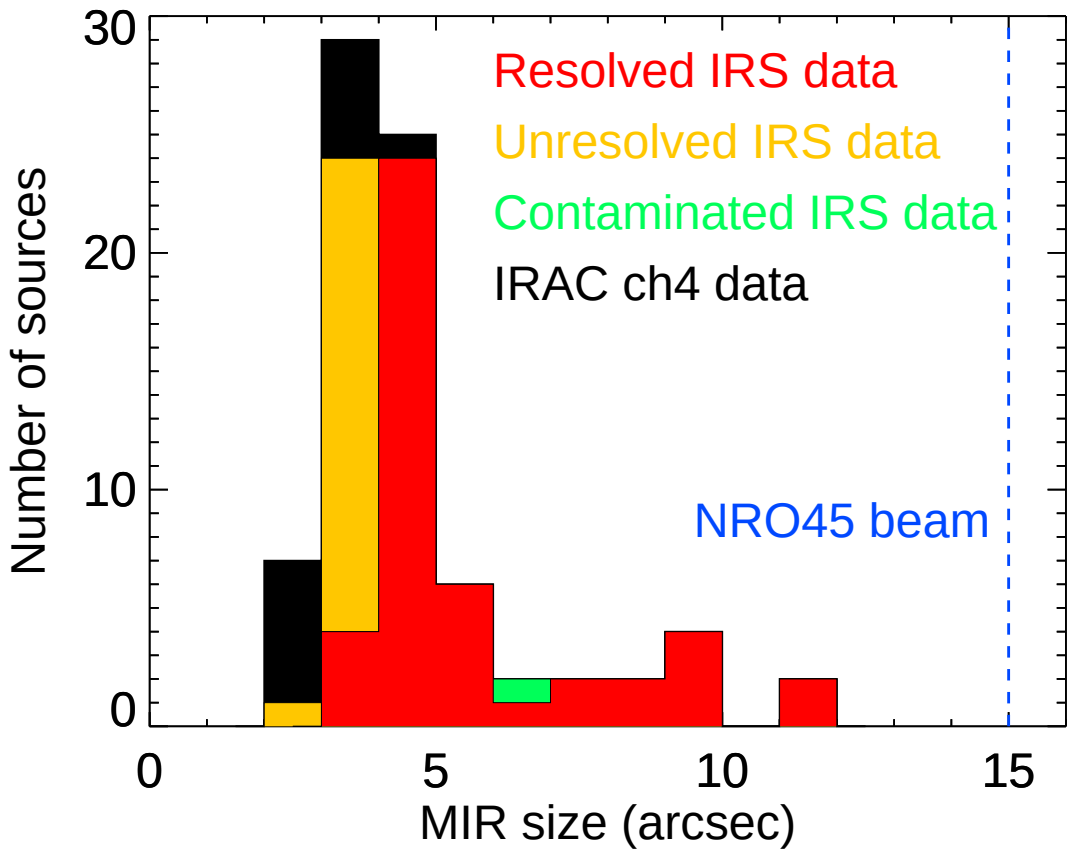

FIGURE 4.1: The size of MIR emitting regions of the sample. The size is taken from Díaz-Santos et al. (2010) and is parameterized by the FWHM of the Gaussian fitting to the Spitzer/IRS spectrogram at 13.2 μm continuum (red). Unresolved data on IRS and contaminated data by emissions from its companion galaxy are also shown (yellow and green, respectively). Spitzer/IRAC 8 μm photometric image (black) is used for those with no available IRS data to calculate the FWHM instead of IRS 13.2 μm size. The beam size of our CO observations is represented as the blue broken line at 15″. All MIR emitting regions of our sources are smaller than the CO beam.

do not resolve the sources. One galaxy is suspected of being contaminated by emission from its companion galaxy. Twelve galaxies do not have information of the MIR size. For these galaxies, I measure the FWHM from the Spitzer/IRAC 8 μm image instead of the IRS 13.2 μm size.

The MIR sizes of the sample are shown in Figure 4.1. The size ranges from 2.1″ to 11.6″, and the median and the average are 5.2″ and 4.6″, respectively. This confirms that all sources of the sample have a more compact MIR emitting region

than the CO beam size of 15″. This warrants the use of the total 24 μm luminosity of our sources to estimate the SFRs in the central regions.

4.2.2 Subtraction of AGN contribution to MIR radiation

On calculating the star formation rate of local LIRGs, the presence of AGN is not negligible. The AGN can contribute to the IR luminosity of galaxies and leads to overestimating the SFR when we derive the SFR of galaxies from the IR luminosity. In the GOALS project, Petric et al. (2011) investigate the AGN contribution to the total IR luminosity using the MIR atomic emission and the PAH emission, and report that 10 % of the GOALS sources have significant AGN contribution of more than 50 % to the total IR luminosity. Alonso-Herrero et al. (2012a) investigate the contribution in a complete volume-limited sample of local LIRGs using MIR spectra and model templates of AGN tori and star-forming regions. Their study shows that ~ 8 % of their sources has significant AGN contribution to the IR luminosity, which is consistent with the study by Petric et al. (2011). In ULIRGs, $\sim 40-50$ % of sources are AGN dominated galaxies (Veilleux et al., 2009).

Here I estimate the AGN contribution to the MIR radiation and subtract it from the 24 μm luminosity in our sample to derive the pure star formation rate. AGN-dominated galaxies in the sample are identified by the same method as used in Figure 2.4. This classification is based on the 6.2 μm PAH EQW, which is employed for IR galaxies (Armus et al., 2007; Petric et al., 2011; Stierwalt et al., 2013, e.g.,). Both emission of the PAH molecules and MIR continuum arise from the radiation field by starburst and/or AGN. Galaxies holding an AGN tend to have low 6.2 μm PAH EQW (Sturm et al., 2000; Desai et al., 2007). This is due to that high energy photons from AGN destroy PAH molecules and heat the surrounding dust. This effect can weaken or vanish the PAH emission, as well as making the MIR continuum prominent on the spectral energy distribution. While the low EQW ($\leqslant 0.27\,\mu$m) indicates AGN-dominated galaxies, the high EQW ($\geqslant 0.53\,\mu$m) indicates starburst-dominated galaxies and intermediate EQW vales ($0.27\,\mu\text{m} \leqslant \text{EQW} \leqslant 0.53$) mean composites of both. The AGN contribution to the MIR emission is estimated using MIR atomic fine-structure emission line ratio of [NeV]/[NeII]. This line-ratio diagnostics is also used for IR galaxies (e.g., Armus et al., 2007; Petric et al., 2011; Inami et al., 2013). The [NeV] emission

line at 14.3 μm is produced by Ne^{4+} ions with an ionization potential of 97.1 eV, which is too large to be produced by O stars. Therefore the detection of [NeV] emission line in a galactic nucleus indicates the presence of an AGN. On the other hand, the ionization potential of Ne^{+} which produces [NeII] emission line 12.8 μm is relatively low, 21.6 eV, and therefore the [NeII] emission line is prominently seen in starburst galaxies (Brandl et al., 2006). Thus the emission line ratio of [NeV]/[NeII] is generally used to identify the presence of an AGN and diagnose the radiation field (e.g., Armus et al., 2007; Petric et al., 2011). Armus et al. (2007) empirically show that the ratio of [NeV]/[NeII] $\geqslant 0.75$ indicate more than 50 % of the AGN contribution to the nuclear MIR emission, assuming a simple linear mixing model.

The PAH EQW and the [NeV]/[NeII] ratio are taken from Spitzer/IRS observations (Stierwalt et al., 2013; Inami et al., 2013). Of all the 79 galaxies, 65 galaxies have both the PAH EQW and the [NeV]/[NeII] ratio determined. Based on the PAH EQW, of the 65 galaxies, 31 are classified as non-starburst-dominated galaxies, i.e., the AGN-dominated and the composite galaxies (red and green circles in Figure 4.2, respectively). Six galaxies out of the non-starburst dominated galaxies show high ratio of [NeV]/[NeII] $\geqslant 0.015$, which corresponds to more than 10 % contribution to MIR emission from an AGN. Therefore I estimate the fraction of the AGN contribution to MIR emission from the [NeV]/[NeII] ratio for these six galaxies (red filled circle) with the AGN contribution of $\geqslant 10$ %. As a result, I calculate that the AGN contribution fractions $f_{\rm AGN}$ are 0.21, 0.33, 0.22, 0–0.11, 0.15 and 0.23 for NGC 0232N, UGC 02608, CGCG 468-002S, Mrk 231, Mrk273 and IC 5298. The SFRs of these six galaxies are corrected by multiplying the SFR derived from 24 μm luminosity by $(1 - f_{\rm AGN})$ in the following section.

4.2.3 Estimate of Star Formation Rate

Here using the 24 μm luminosity, I estimate the central SFR of the 65 sources which have gone through the diagnostics of the AGN contribution in the previous section. The estimation employs the Spitzer/MIPS 24 μm image and a calibration equation from the 24 μm luminosity to the SFR by Alonso-Herrero et al. (2006).

In order to obtain the luminosity, first, I measure the 24 μm flux of the sample from the MIPS 24 μm image (channel 1) which is acquirable from the

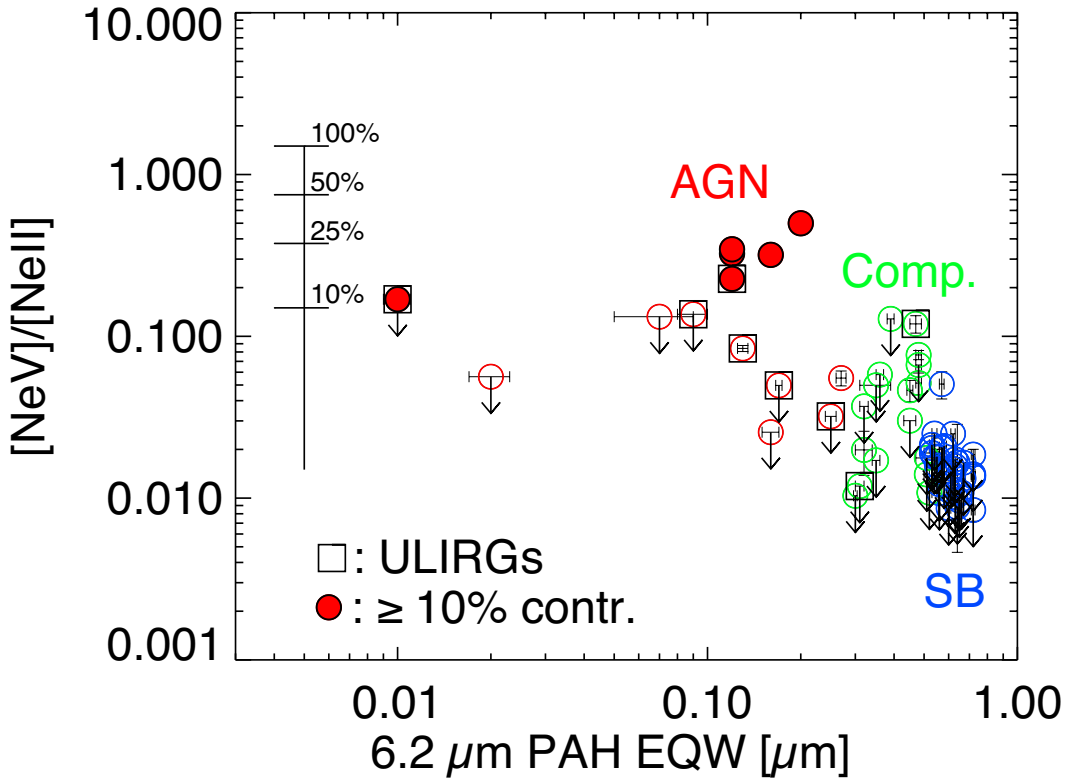

FIGURE 4.2: The 6.2 μm PAH EQW and mid-infrared [NeV]/[NeII] emission line ratio. The blue, green and red circles are the starburst-dominated, composites and AGN-dominated galaxies. The arrows indicate upper limits and the black squares indicate ULIRGs. The 1 σ errors are shown by bars but are mostly small compared to the symbols. The horizontal line along y-axis shows the fraction of the AGN contribution to MIR emission. The 100 % level is the mean value of [NeV]/[NeII] ratio among AGNs (Armus et al., 2007). The six red filled circles are the sources with the AGN contribution of $\geqslant$ 10 %.

GOALS webpage in the NASA/IPAC Infrared Science Archive[1]. The MIPS 24 μm image of all galaxies are available except for NGC 4194 whose flux is saturated (the documents of the GOALS Second Data Delivery). The flux is measured using a circular aperture with a radius of 35″ and a sky annulus from 40″ to 50″. A different sky annulus with a radius from 80″ to 100″ is applied to NGC 7752N in order to avoid its companion galaxy NGC 7752S. Two galaxy pairs, CGCG 468-002S/N and IRASF09111-1007W/E, are too close (their separations are 29″ and 37″, respectively) to measure their flux individually. For these galaxies, I allocate a total flux of two galaxies in a pair using their peak ratio of the 24 μm images.

[1] `http://irsa.ipac.caltech.edu/data/SPITZER/GOALS/`

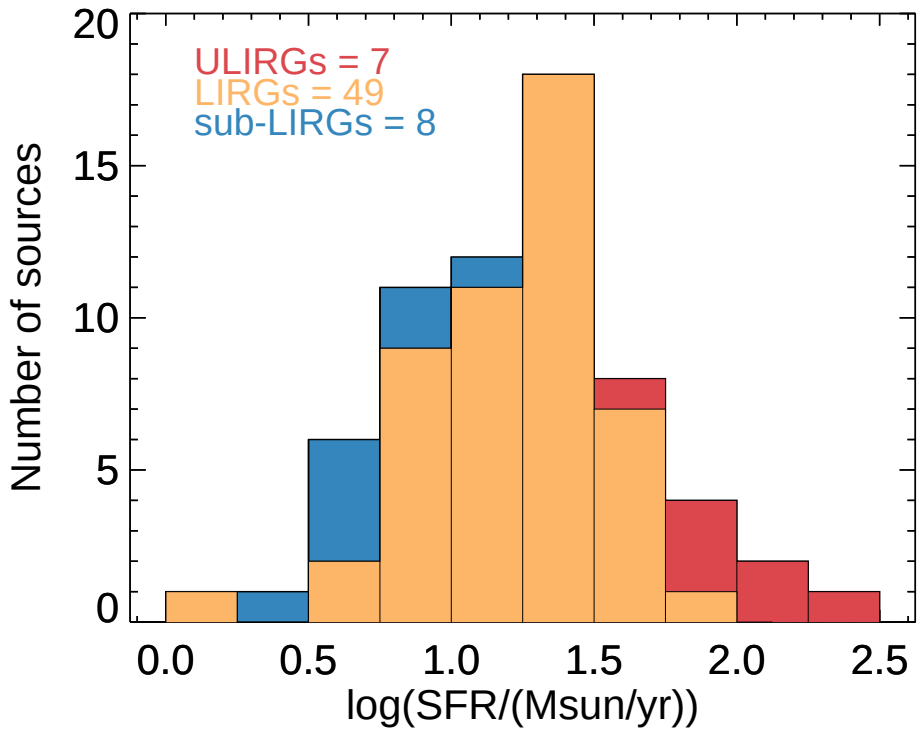

FIGURE 4.3: The SFR in the central region of the sample. The SFR is estimated from the 24 μm luminosity and the calibration by Alonso-Herrero et al. (2006) (Equation 4.3). The SFRs of sources with the AGN contribution of $\geqslant 10\,\%$ are corrected (see Section 4.2.2). NGC 4194 is not shown because no data of the 24 μm image are available. The galaxies of the ULIRG class (red), the LIRG class (orange) and the sub-LIRGs class (blue) are shown separately.

The measured flux is 0.87 Jy on the average with a median value of 0.64 Jy. The uncertainties in the flux are approximately 4 %, dominated by the calibration uncertainties of approximately 4 % (MIPS Instrument Handbook version 3). The sample galaxies are rather bright in the MIPS 24 μm so that uncertainties arising from the photometry are as small as $\sim 1\,\%$. Aperture correction is not applied for all sources because the emission are not ideal point sources, but extended compared to the point spread function. The correction is only 6 % in a case of the point source (MIPS Instrument Handbook version 3), so the correction does not significantly affect our study comparing the CO observation data.

The 24 μm luminosity, $L_{24\,\mu\mathrm{m}}$, of the galaxies is calculated from the 24 μm flux $f_{24\,\mu\mathrm{m}}$ using the following equation,

$$L_{24\,\mu\mathrm{m}} = 1.51 \times 10^{40}\, f_{24\,\mu\mathrm{m}}\, D_L^2, \tag{4.1}$$

where $L_{24\,\mu\mathrm{m}}$, $f_{24\,\mu\mathrm{m}}$ and D_L are in the unit of erg s^{-1}, Jy and Mpc, respectively. I also use the 24 μm luminosity in the unit of $L_\odot$ calculated from a following equation,

$$L_{24\,\mu\mathrm{m}} = 5.80 \times 10^{7}\, f_{24\,\mu\mathrm{m}}\, D_L^2. \tag{4.2}$$

The SFR is derived from the $L_{24\,\mu\mathrm{m}}$ using the equation [3] in Alonso-Herrero et al. (2006). They find a tight correlation between $L_{24\,\mu\mathrm{m}}$ luminosity and extinction-corrected Paschen α luminosity over star-forming regions in M51, normal galaxies, local LIRGs and ULIRGs. Using the correlation and a traditional conversion equation from Hα luminosity to SFR by Kennicutt (1998a), who assume a stellar evolutionally synthesis model including the solar abundance and the Salpeter IMF (Salpeter, 1955), they calibrate the following $L_{24\,\mu\mathrm{m}}$–SFR conversion,

$$\left(\frac{\mathrm{SFR}}{M_\odot \mathrm{yr}^{-1}}\right) = 8.45 \times 10^{-38} \left(\frac{L_{24\,\mu\mathrm{m}}}{\mathrm{erg\,s}^{-1}}\right)^{0.871}. \tag{4.3}$$

For the six sources with the AGN contributions over 10 %, the SFRs are derived after the 24 μm luminosity is corrected by multiplying by $(1 - f_{\mathrm{AGN}})$ (see the previous section). The derived SFR of the central region in the 64 galaxies is shown in Figure 4.3 and ranges from 1.6 $M_\odot$yr^{-1} for UGC 03410S to 238 $M_\odot$yr^{-1} for Mrk 231, and the median and the average are 29 $M_\odot$yr^{-1} and 18 $M_\odot$yr^{-1}, respectively. The statistics among only the LIRGs, namely galaxies with $L_{\mathrm{IR}} \geqslant 10^{11.0}\, L_\odot$, shows the SFR range of 1.6–238 $M_\odot$yr^{-1}, a median of 22 $M_\odot$yr^{-1} and the average of 32 $M_\odot$yr^{-1}.

4.3 Star Formation Efficiency

The SFR which I derived in the previous section represents the integrated magnitude of star formation of galaxies and depends on both the amount of molecular gas and the scale of the galaxy. On the other hand, the SFR normalized by the molecular gas mass, namely the ratio of the current SFR to the available molecular gas mass, SFR/$M_{\mathrm{H_2}}$, is a gauge of the strength of star formation of

galaxies without any dependences on the galaxy's scale. This normalized SFR (or $\mathrm{SFR}/M_{\mathrm{H_2}}$) is also considered as an efficiency of transformation from the gas mass to stars at the current SFR. The efficiency is called star formation efficiency (SFE) and is described as,

$$\mathrm{SFE}\,[\mathrm{yr}^{-1}] = \frac{\mathrm{SFR}\,[M_\odot \mathrm{yr}^{-1}]}{M_{\mathrm{H_2}}\,[M_\odot]}. \tag{4.4}$$

The active gas inflow towards the galactic center and the possibly resultant compact gas distribution in merging LIRGs (see Chapter 3) may prompt dense molecular gas to increase in the central region. The enhanced fraction of the dense gas may result in an efficient transformation from gas to stars, showing elevated SFE. Daddi et al. (2010a) and Genzel et al. (2010) report two sequences of star formation in the Kennicutt-Schmidt law, which are, the starburst mode showing a high $L_{\mathrm{IR}}/M_{\mathrm{H_2}}$ corresponding to a high SFE $\gtrsim 20 \times 10^{-9}\,\mathrm{yr}^{-1}$ and a disk star formation mode showing a modest $L_{\mathrm{IR}}/M_{\mathrm{H_2}}$ corresponding to a SFE $\sim 2 \times 10^{-9}\,\mathrm{yr}^{-1}$. The populations in the starburst mode contain local ULIRGs and submillimeter galaxies, while the disk star formation mode contains local spirals and distant normal star-forming galaxies (e.g., BzK galaxies Daddi et al., 2004, 2008, 2010b). The local ULIRGs and submillimeter galaxies are usually involved with major mergers and show compact star-forming regions. The local ULIRGs also have an obviously elevated fraction of dense gas to total gas (Gao & Solomon, 2004b). The global SFE of galaxies gently correlates with the dense gas fraction from less-IR luminous galaxies to ULIRGs (Gao & Solomon, 2004b).

An inverse of the SFE expresses a depletion timescale of the total gas mass at the current SFR. The gas depletion timescale τ_{dep} is described as,

$$\tau_{\mathrm{dep}}\,[\mathrm{yr}] = (\mathrm{SFE}[\mathrm{yr}^{-1}])^{-1}. \tag{4.5}$$

A high SFE means a short timescale of gas depletion. The starburst mode galaxies described above can exhaust the total molecular gas in less than 50 Myr, while the disk mode galaxies in ~ 500 Myr.

The SFE and the τ_{dep} of the central regions in our local LIRG sample are calculated using the SFR derived from the 24 μm luminosity and the molecular gas mass of our CO observation, and are shown in Figure 4.4 and 4.5. The SFE ranges from $1.8 \times 10^{-9}\,\mathrm{yr}^{-1}$ to $72 \times 10^{-9}\,\mathrm{yr}^{-1}$, with a median of $14 \times 10^{-9}\,\mathrm{yr}^{-1}$ and with a average of $19 \times 10^{-9}\,\mathrm{yr}^{-1}$. The τ_{dep} ranges from 14 Myr to 570 Myr, and the

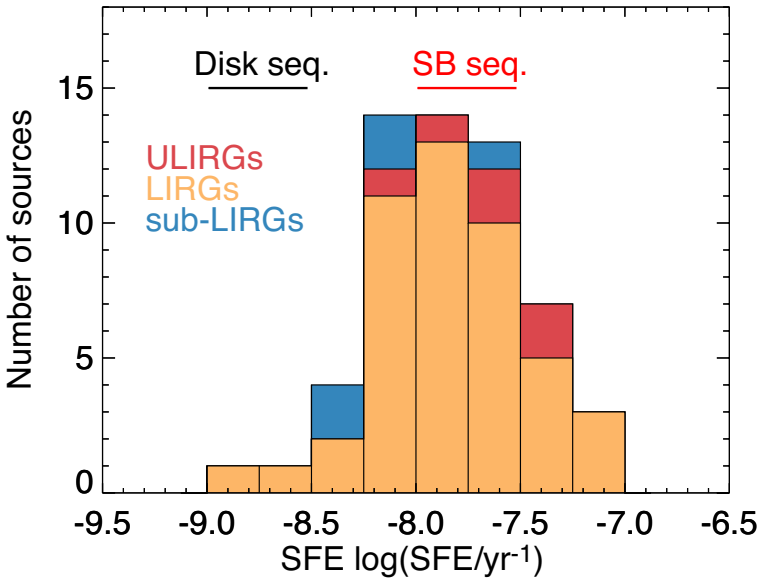

FIGURE 4.4: The SFE in the central regions of the sample. The SFE is defined in Equation 4.4. The SFR is estimated from the Equation 4.3 using the 24 μm luminosity and the AGN contributions are corrected. The molecular gas mass is from our CO observations. The ULIRGs, LIRGs and sub-LIRGs are shown by red, orange and blue boxes, respectively. The SFE ranges from $1.8 \times 10^{-9}\,\mathrm{yr}^{-1}$ to $72 \times 10^{-9}\,\mathrm{yr}^{-1}$, with a median of $14 \times 10^{-9}\,\mathrm{yr}^{-1}$ and with an average of $19 \times 10^{-9}\,\mathrm{yr}^{-1}$. The red and black solid lines represent the expected SFEs of a galaxy with a IR luminosity of $10^{11-13}\,L_{\odot}$ on the each modes of the starburst sequence and the disk star-formation sequence (Daddi et al., 2010a).

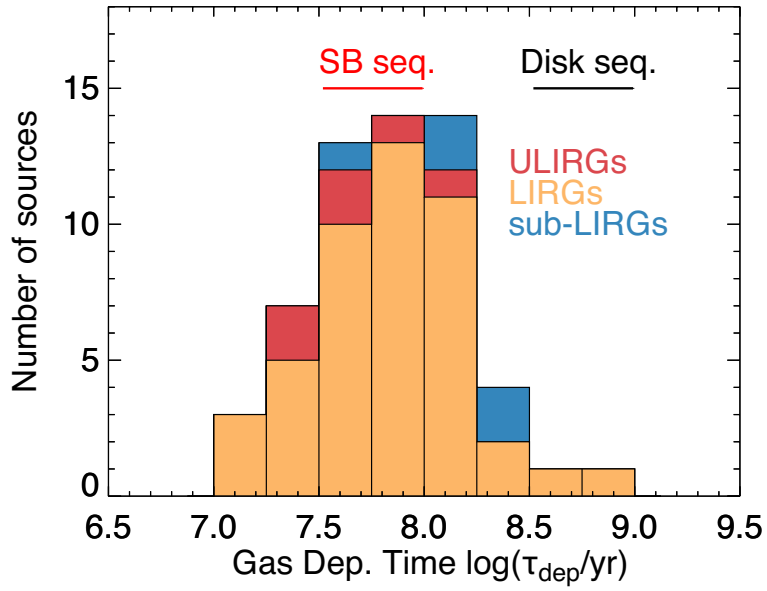

FIGURE 4.5: The gas depletion timescale of the sample, which is calculated using Equation 4.5. The color and pattern are the same as Figure 4.4. The τ_{dep} ranges from 14 Myr to 570 Myr. The median and the average are 70 Myr and 97 Myr, respectively. The red and black solid lines represent the expected τ_{dep} of a galaxy with a IR luminosity of $10^{11-13}\,L_{\odot}$ on the each modes of the starburst sequence and the disk star-formation sequence (Daddi et al., 2010a).

median and the average are 70 Myr and 97 Myr, respectively. Only for galaxies of LIRG class ($\log(L_{\rm IR}/L_{\odot}) \geqslant 11.0$), the SFE, the median and the average are $1.8 - 72 \times 10^{-9}\,{\rm yr}^{-1}$, $15 \times 10^{-9}\,{\rm yr}^{-1}$ and $20 \times 10^{-9}\,{\rm yr}^{-1}$, respectively. The $\tau_{\rm dep}$ for the LIRGs are 14 – 570 Myr, 66 Myr and 92 Myr, respectively. The SFE of the central regions of local LIRGs overlaps the SFE at the starburst sequence (Daddi et al., 2010a) (the red shaded area in Figure 4.4 and 4.5). The discussion of the star formation mode and the comparison of the SFE with other population are in Section 4.5.3.

Interestingly, most sub-LIRGs show comparable SFE to the LIRGs and belong to the starburst sequence. These sub-LIRGs are NGC 0232N, CGCG 465-012N, UGC 03410N, NGC 7771N and NGC7771S2, and have SFEs of more than $5 \times 10^{-9}\,{\rm yr}^{-1}$. All four sub-LIRGs are less-massive companions of major mergers except for NGC 7771S2 which is a less-massive companion in minor mergers. This high SFE in sub-LIRGs is likely due to that they may be effectively affected by the gravitational perturbation driving starburst from massive companions, which is predicted by simulations (Cox et al., 2008). In particular, a less-massive satellite galaxy, NGC 7771S2 (the stellar mass ratio ~ 0.1), shows the three times higher SFE than its massive companion NGC 7771S1. This galaxies are experiencing a galaxy-wide starburst induced by the interaction and may strip the gas from NGC 7771S1 (Alonso-Herrero et al., 2012b).

4.4 Star Formation and Merger Stage

In this section, I examine the behavior of the star formation along the merger process of local LIRGs. I classify the galaxies into five stages of merger using the morphological classification by Stierwalt et al. (2013): non-merger (stage 0), pre-merger (stage 1), early stage merger (stage 2), mid-stage merger (stage 3) and late stage merger (stage 4). The distribution of the merger stage is shown in Figure 2.3 in Chapter 2.

Figure 4.6 shows the evolution of the SFR on the merger sequence. The maximum and minimum SFRs at the each stage seems to increase towards advanced stages. However, both the median SFR of a combined sample (U/LIRGs) of LIRGs (orange circles) and ULIRGs (red circles) is constant within the errors

as a function of merger stage. This is consistent with the optical result by Dopita et al. (2002), who also do not observe any trend between the merger stage and the SFR estimated from Hα emission. It is reasonable to interpret that this constant SFR is due to sample-selection where I selectively observe galaxies at a luminous phase rather than a continuous starburst. Recent simulations predict a short timescale of starburst (20 – 300 Myr; Saitoh et al., 2009; Cox et al., 2008), which is shorter than the intervals between the stages used here. At the late stage (stage 4), LIRGs are coexistent with ULIRGs and have lower SFR than ULIRGs. The LIRGs at the late stage may be galaxies prior to a ultraluminous starburst, namely ULIRGs, or immediately after experiencing the ULIRG phase. This interpretation is consistent with a dynamical study by Murphy et al. (2001).

Molecular gas mass is also constant along merger stage, which is the same as Figure 3.1 in Chapter 3 but here the merger stage is subdivided from three to five. In Chapter 3, I have already discussed this constant trend and I concluded that this is likely due to the global gas inflow towards the galaxy center. While the molecular gas therein is consumed by the violent starburst (SFR $\gtrsim 10\,M_{\odot}\mathrm{yr}^{-1}$) rapidly at the timescale of $\lesssim 100$ Myr, the central several kpc region is replenished by the gas which is likely from the outer disk. Here, in addition to that discussion, I further mention a similar fluctuation in $M_{\mathrm{H_2}}$ to the merger stage as seen in SFR (Figure 4.6). In particular, the peaks of the SFR and $M_{\mathrm{H_2}}$ both appear at the early stage (stage 2) and the late stage (stage 4). These stages, respectively, correspond to the first passage phase and the final coalescence of the nuclei, where the maximum starbursts can occur owing to the strong gas inflow (Cox et al., 2008).

Figure 4.8 shows the SFE at the each merger stage of the sample. The SFE of the U/LIRGs do not vary with advancing merger stage and is always as high as the starburst sequence $\gtrsim 10^{-8}\,\mathrm{yr}^{-1}$. LIRGs are observed selectively, so galaxies which are at the luminous starburst phase around the peaks of the star formation history of the merger sequence. Although there are somewhat variations of the SFR and the $M_{\mathrm{H_2}}$ during the merger sequence, no variation of the efficiency is seen in the merger sequence. This means that the same relational expression of the transformation from the molecular gas to the stars between each stages, whose intervals are approximately a few hundred Myr, is dominant through all stages. The scatters of SFE at each stage are reduced compared to the SFR and $M_{\mathrm{H_2}}$. This strengthens the common gas-SFR relation in merging LIRGs. At the late stage

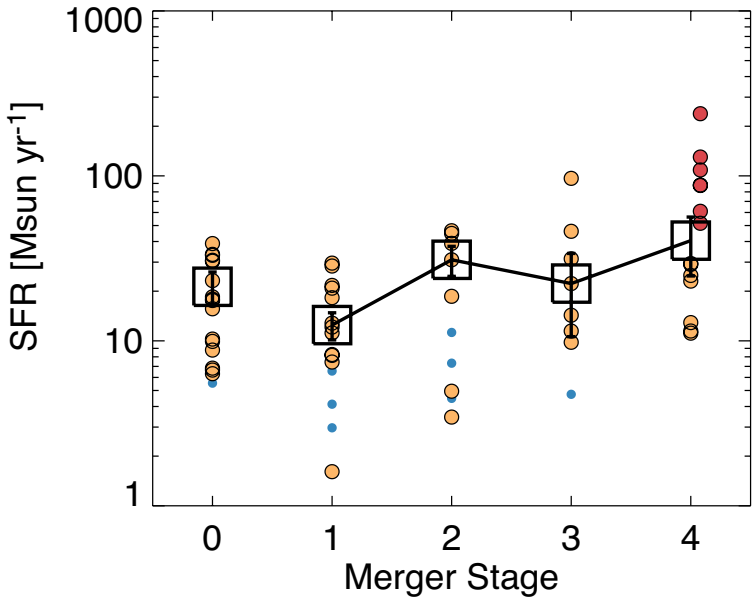

FIGURE 4.6: The SFR as a function of merger stage. The merger stage is taken from Stierwalt et al. (2013). The ULIRGs, LIRGs and sub-LIRGs are plotted as the red, orange and blue circles. The median values are shown by the black squares for the combined sample of both the LIRGs and the ULIRGs.

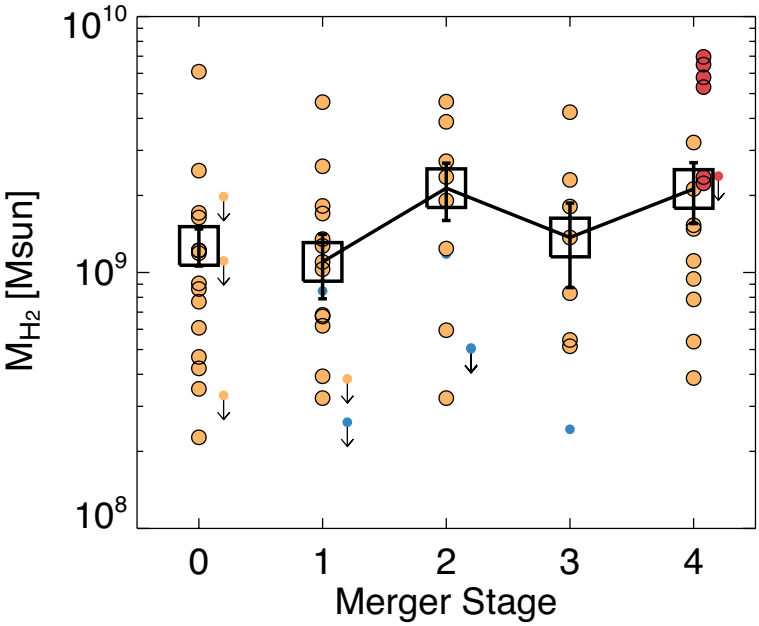

FIGURE 4.7: The molecular gas mass as a function of merger stage. The symbols represent the same as Figure 4.6, but the arrows mean the upper limits of $M_{\mathrm{H_2}}$.

(stage 4), the SFEs of LIRGs and ULIRGs are $1.7 \times 10^{-8}\,\mathrm{yr}^{-1}$ and $2.3 \times 10^{-8}\,\mathrm{yr}^{-1}$, and the errors are $0.3 \times 10^{-8}\,\mathrm{yr}^{-1}$ and $0.5 \times 10^{-8}\,\mathrm{yr}^{-1}$, respectively. Within the error margins, there are no difference of the SFE between LIRGs and ULIRGs at the late stage, unless α_{CO} of ULIRGs is systematically two times small/large compared with LIRGs at the late stage. No discrepancies of the gas-SFR relation are observed in the Kennicutt-Schmidt law (Figure 4.9).

The results about $M_{\mathrm{H_2}}$ (Figure 4.7) and SFE (Figure 4.8) along the merger sequence depend on whether there is a systematic variation of α_{CO} along the merger stages, although the random scatter in α_{CO} of a factor ~ 3 (see the discussion in Chapter 1.3.2) would not change the conclusions of these results. Narayanan et al. (2011) investigate a variation in the CO-H_2 conversion factor along the merger sequence, and find that the CO-H_2 conversion factor decreases at a starburst phase with an enhanced SFR. This is caused by increases in the gas velocity dispersion and the gas temperature at the starburst phase. If all the LIRGs at on-going merger stages are at the starburst phase in the merger sequence, their α_{CO} at all merger stages should no differ systematically and be equally lower than the Galactic value. This is expected from that the median SFR of our sample is constant along the merger stages (Figure 4.6). Inami et al. (2013) find that [NeIII]/[NeII] ratios, which reflects the hardness of the radiation field, are constant throughout the merger stages of the GOALS LIRGs. This means that the radiation fields at all the merger stages are always dominated by young and massive stars such as products from starbursts. Therefore, merging LIRGs are starbursting at any merger stages.

4.5 Discussion

4.5.1 Do LIRGs Evolve to ULIRGs?

Merging LIRGs are likely to be mergers residing at the peaks of the merger-induced star formation on the merger sequence. LIRGs have high SFR ($32\,M_{\odot}\,\mathrm{yr}^{-1}$ on the average) compared to isolated spiral galaxies and less IR luminous interacting galaxies (Tinney et al., 1990). Such high SFR cannot be maintained continuously over all stages because the total gas mass $\sim 10^{9-10}\,M_{\odot}$ is rapidly consumed

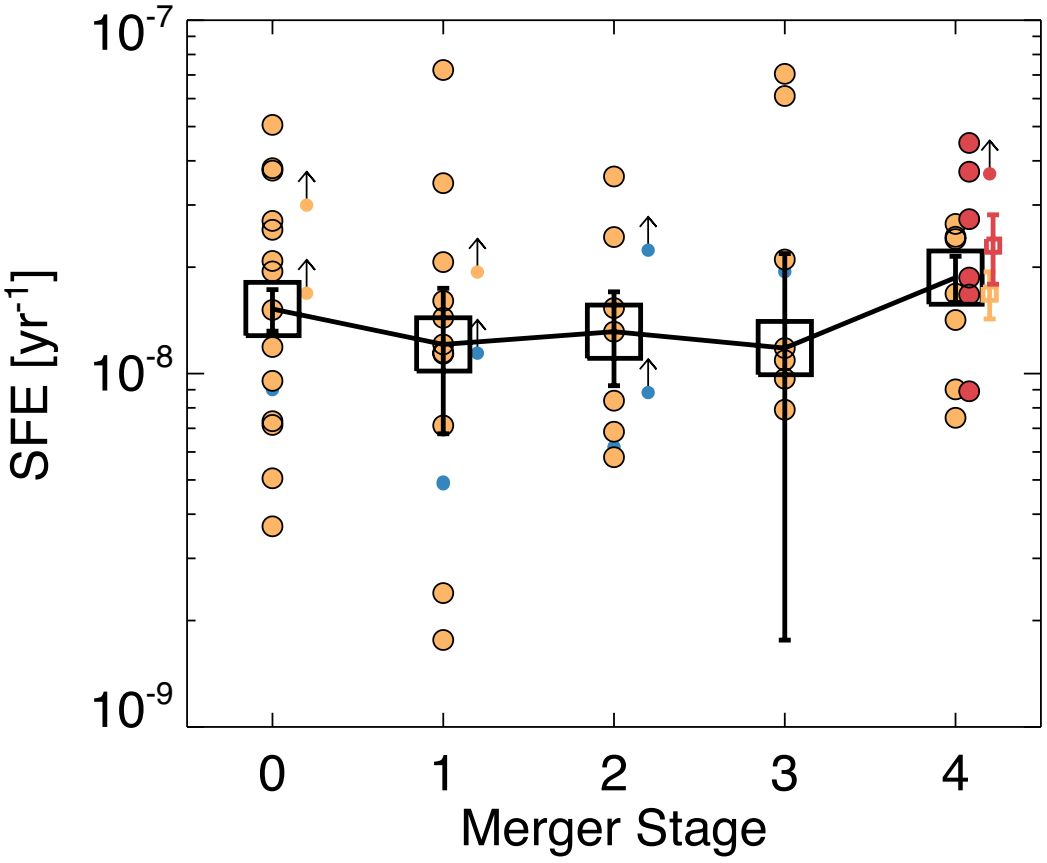

FIGURE 4.8: The SFE as a function of merger stage. The symbols represent the same as Figure 4.7, but the orange and red squares indicate median values of LIRGs and ULIRGs at the stage 4, respectively.

at the high SFR in the short time depletion timescale of less than a few hundred Myr. Simulations support the instantaneous bursts on the merger evolution (e.g., Cox et al., 2006). Dynamical studies by Murphy et al. (2001) and Haan et al. (2011) find that local LIRGs show bimodal distributions in merger time. The two distributions are comparable to the stage after the perigalactic passage and the final stage of the nuclear coalescence. Therefore the luminous starbursting mergers on the merger sequence are probably preferentially selected as the merging LIRGs in the sample.

The LIRGs are found over the full stages of mergers, while all the ULIRG in the sample belong to the late stage (stage 4). This seemingly implies that ULIRGs are the end product of the evolutionary sequence of mergers. However, there are

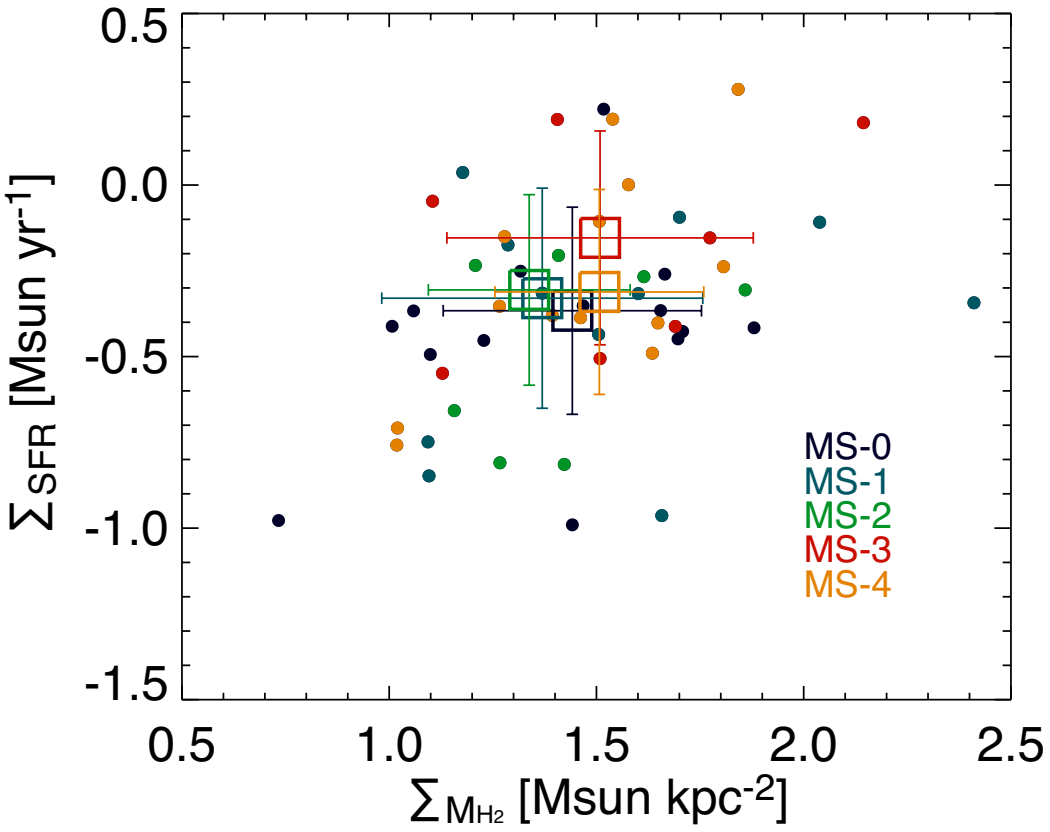

FIGURE 4.9: The Kennicutt-Schmidt law by the merger stage. The colors show the merger stages: non-merger (stage 0, black), pre-merger (stage 1, blue), early stage merger (stage 2, green), mid-stage merger (stage 3, red) and late stage merger (stage 4, orange). The squares indicate the median values which are calculated for the combined sample of both the LIRGs and the ULIRGs.

also seven LIRGs at the late stage (stage 4) in the sample, whereas seven others are ULIRGs. These late stage LIRGs have relatively low SFR and $M_{\rm H_2}$ (Figure 4.6 and 4.7). Considering merger simulations which predict the peaky starbursts and the steep rise up to and decline from ULIRG phase in SFR predicted by merger simulations, this result suggests that the late stage LIRGs are mergers prior to (pre-ultraluminous starburst) or immediately after the short ultraluminous starburst phase, or (pre-/post-ultraluminous starbursts). Their gas has only just begun to supply towards the central region or the large amount of the molecular gas has been exhausted by the final starburst. Because these late stage LIRGs have either already ignited their starburst, which leads to the ULIRG phase, or have not settled to a quiescent phase yet after the ULIRG phase, they are starbursting with

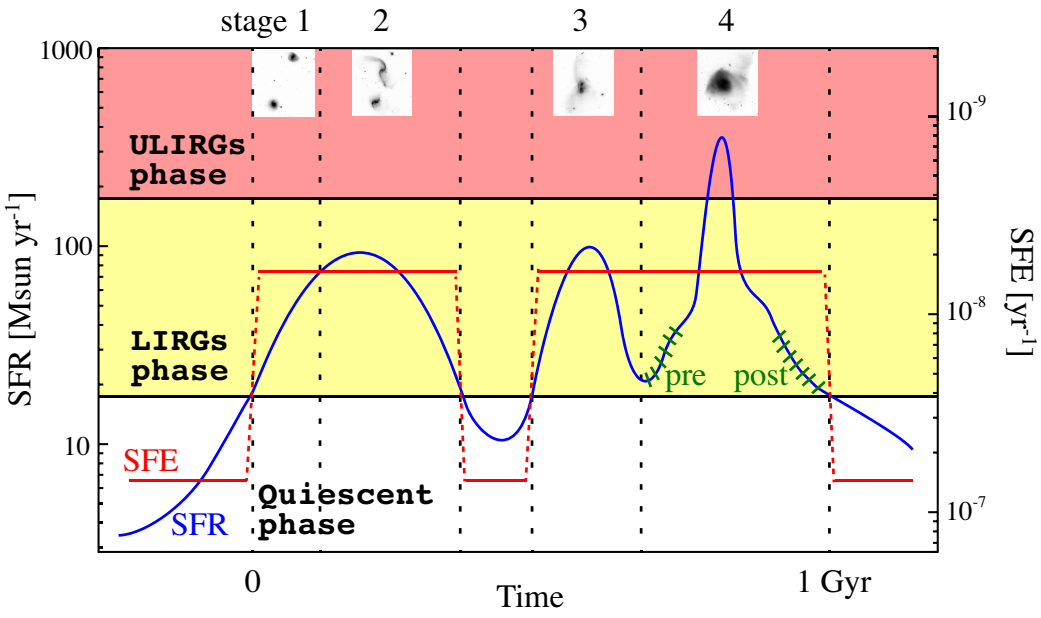

FIGURE 4.10: This is a schematic view of the time variation of the SFR and SFE in merger. The blue curve and red line represent the SFR history and the constant SFE along the merger sequence. The broken lines delimitate each merger stages from pre-merger (stage 1) to late stage (stage 4). The optical images of four stages are shown. The LIRG and ULIRG phases are shown by the shaded areas with yellow and red, respectively. The green shaded line indicate the pre-/post-ultraluminous starburst phases.

the similar SFE. This description of the evolutionary connection between LIRGs and ULIRGs is consistent with the dynamical study (Murphy et al., 2001). They also argue the similar scenario from their bimodal time distribution. As inspired by their study, a schematic of the evolutionary history of LIRGs and ULIRGs is illustrated in Figure 4.10.

Whether galaxies become LIRGs or ULIRGs is determined only by the amount of molecular gas in the central regions, thus there are possibilities that the late stage LIRGs are galaxies that do not undergo the ULIRG phase due to the progenitors having insufficient gas content or galaxies run out of a large amount of the gas at the early stage. Some early stage ULIRGs paired with companions have been observed (Dinh-V-Trung et al., 2001; Murphy et al., 2001) although are not included in the sample of this study. This means that even at the early stage, ultraluminous starbursts can be realized and a large amount of the gas

can be exhausted early. Mergers of bulgeless galaxies or retrograde mergers often show maximum SFR at the early stage in simulations (Mihos & Hernquist, 1994, 1996). The initial orbit of interacting galaxies may largely affect the timing and magnitude of early stage starburst (Di Matteo et al., 2007).

4.5.2 Star Formation in Local LIRGs

The SFE is found to be constant throughout the all merger stages in merging starburst LIRGs. This suggests that the conversion from gas to stars is driven by a common relation regardless of the merger stage. The SFR is represented by,

$$\mathrm{SFR} = \epsilon \frac{M_{\mathrm{gas}}}{\tau_{\mathrm{sf}}}, \tag{4.6}$$

where ϵ is the efficiency of the star formation which is less than unity, and τ_{SF} is the star formation timescale. Substituting Equation 4.6 into Equation 4.4, the SFE is rewritten as,

$$\mathrm{SFE} = \frac{\epsilon}{\tau_{\mathrm{sf}}}. \tag{4.7}$$

Here the SFE is represented as the efficiency per star formation timescale. For clouds in nearby galaxies, ϵ falls within a narrow range of several 10^{-2} (Wilson & Matthews, 1995; Taylor et al., 1999). To realize a constant SFE between all the merger stages of the starburst LIRGs, the star formation timescale also needs to be constant throughout all the stages. The dominant timescale controlling star formation maintaining constant SFE is assessed out of three possible star formation timescales: the free-fall timescale (the star formation due to the spontaneous gravitational instability), the cloud-cloud collision timescale (the cloud-cloud collision star formation) and the dynamical timescale (the star formation dominated by large-scale dynamics of the galaxies).

If star formation is regulated by the the spontaneous gravitational instability of the molecular clouds, the star formation timescale is limited by the free-fall timescale τ_{ff}. The free-fall timescale is proportional to $\rho^{-1/2}$ where ρ is the volume gas density. Recent simulations predict small changes in the probability distribution function of gas density ρ between the early stage and the late stage (Teyssier et al., 2010). Therefore, τ_{ff} can be assumed to be constant throughout the duration of the merger process. The peak gas densities are around $10^{3-4}\,\mathrm{cm}^{-3}$ at both the early and late stages (Teyssier et al., 2010), so τ_{ff} is approximately $0.5 - 1.6\,\mathrm{Myr}$.

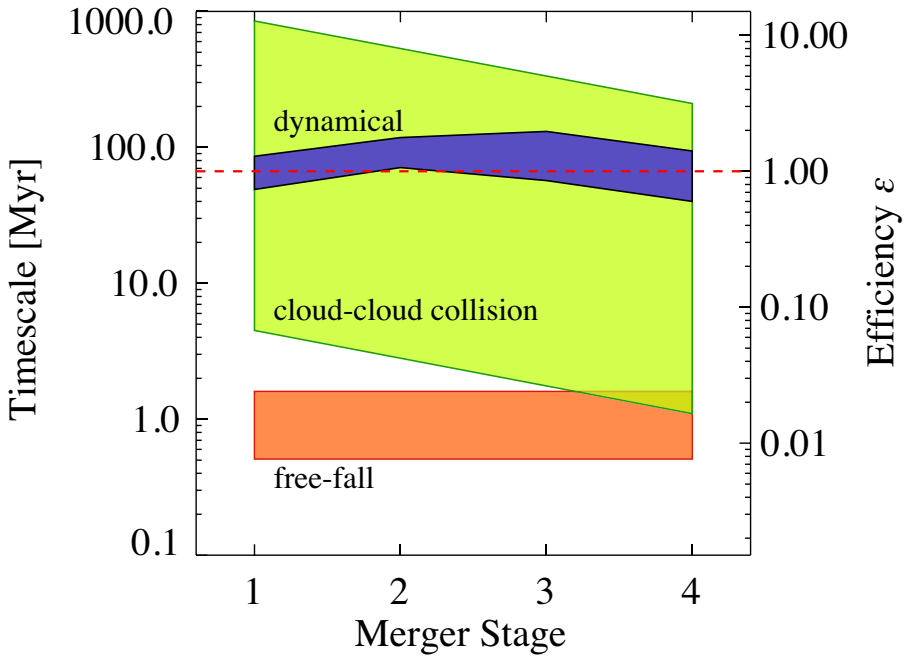

FIGURE 4.11: The three timescales and the efficiency ϵ at each merger stage (see text). Three colored zones are the possible values of the free-fall timescale $\tau_{\rm ff}$ (orange), the cloud-cloud collision timescale $\tau_{\rm ccc}$ (green) and the dynamical timescale $\tau_{\rm dyn}$ (blue), respectively. The red broken line indicate the limit of $\epsilon \leqslant 1$.

Using Equation 4.7 and the median SFE of $1.5 \times 10^{-8}\,{\rm yr}^{-1}$ in merging U/LIRGs, ϵ is calculated to be $\sim 0.008 - 0.02$, which is realistic in galaxies (Wilson & Matthews, 1995; Taylor et al., 1999). Hereafter ϵ is calculated using this method and the same SFE.

If cloud-cloud collision is the predominant trigger of star formation of the merging LIRGs, the star formation is regulated by the timescale of the cloud-cloud collision $\tau_{\rm ccc}$. According to a simple model in Komugi et al. (2006), $\tau_{\rm ccc}$ equals $(\sqrt{2}\,N D \sigma_{\rm c})^{-1}$, where N is the surface number density of molecular clouds, $\sigma_{\rm c}$ is the the cloud-cloud velocity dispersion and D is the diameter of a cloud. Assuming that the mass of a cloud ($m_{\rm C}$) is $10^{6-7}\,M_\odot$ (Teyssier et al., 2010), from the median $M_{\rm H_2}$ in the merging U/LIRGs ($1.5 \times 10^9\,M_\odot$), N is estimated to be $\sim (2 - 20) \times 10^{-6}\,{\rm pc}^{-2}$ within the beam. According to the mass-radius relation of clouds (Larson, 1981; Solomon et al., 1987), clouds of $m_{\rm C} = 10^{6-7}\,M_\odot$ have a diameter D of $86 - 270\,{\rm pc}$. In nearby galaxies, A typical $\sigma_{\rm c}$ is $6\,{\rm km\,s}^{-1}$ (Wilson

et al., 2011). (Furukawa et al., 2009; Torii et al., 2011; Fukui et al., 2014) find possible evidence of the star formation triggered by cloud-cloud collisions, and report relative velocity between colliding clouds to be 10–20 kms^{-1}. This is likely applicable to mergers, because the observed velocity dispersion between clusters in a prototype merger at the mid-stage, the Antennae galaxies, is less than 10 $\mathrm{km\,s}^{-1}$ (**?**). Therefore a conservative range of the velocity dispersion of $5 - 30\,\mathrm{kms}^{-1}$ are assumed here. Thus the timescale τ_{ccc} is estimated to be 5–850 Myr, and ϵ becomes 0.07–13. As discussed in Chapter 3, the CO radius decreases by a factor of ~ 2 from the early stage to the late stage. This results in N elevated by a factor of four at the late stage, and thus leads to a shorter τ_{ccc} of 1–210 Myr at the late stage compared to the early stage. At this time ϵ is 0.02–3, which is a reasonable value.

When the SFE of the starburst is determined by the disk instability, the orbital timescale of the disk or the dynamical timescale can control the star formation (Silk, 1997; Kennicutt, 1998b). The dynamical timescale τ_{dyn} is defined as $2\pi R/V(R)$, where R is a radius of the star-forming region and $V(R)$ is a rotation velocity of the disk (Kennicutt, 1998b). Using the CO velocity width and the CO beam radius of the CO observations, τ_{dyn} is calculated at the each merger stage. From stage 1 to stage 4, the τ_{dyn} are $49 - 86$ Myr, $71 - 120$ Myr, $57 - 130$ Myr and $40 - 94$ Myr, respectively, in consideration of the errors calculated by the standard deviation divided by the square root of the number of sources. The τ_{dyn} varies along the merger stage and becomes large at the stages 2 and 3. When the merging LIRGs form stars with these dynamical timescales, ϵ exceeds the limit of 1.0 at the most cases, and thus the dynamical timescale is not reasonable for limiting the star formation in these galaxies. Note that τ_{dyn} at the stages 3 and 4 may be overestimated because of overestimates of R due to the used CO beam size, because the CO radius decreases to 1–4 kpc at the late stage. In this case, the dynamical timescale become to be acceptable for only galaxies at stages 3 and 4.

The three estimated timescales are shown in Figure 4.11. The free-fall timescale is likely to be constant at a reasonable efficiency during merger, and is always shorter than the other timescales except for the late stage where a narrow range of parameters ($m_{\mathrm{C}} \sim 10^6\,M_\odot$, $\sigma_{\mathrm{C}} \sim 30\,\mathrm{kms}^{-1}$) may shorten τ_{CCC} to be nearly equal to τ_{ff}. Therefore the constant timescale of free-fall may be reasonable for explaining the observed constant SFE and thus spontaneous star formation may be dominating the luminous starburst in merging LIRGs. However, in the case of

the cloud-cloud collision, the timescale can beconstant at the lower efficiency than unity, although the timescale is larger than the free-fall timescale. Therefore the cloud-cloud collision may contribute to star formation as a secondary mechanism.

Another factor, an effect by the spatial averaging, or the beam smearing effect, may cause a constant SFE to be observed. The regions where the luminous starbursts take place may be clumpy and compact (Teyssier et al., 2010). In such starbursts, we observe only the average of SFE distribution of the clumps within the single-dish beam. Even if the SFE distribution varies along the merger sequence, unless the average significantly changes, a constant SFE will be observed.

4.5.3 Global Merger Evolution

The merging LIRGs show constant SFE, suggesting a common conversion relation from gas to stars in the luminous starburst phase, which is likely due to a constant timescale of star formation, represented by the free-fall timescale. In this section, in order to describe the evolutionary picture with respect to the merger-driven star formation, the merging LIRGs are put on the frame of the relation between the surface gas density and the star formation rate density, namely the KS law. The mechanism of star formation of galaxies is often discussed using the KS law. The $\Sigma_{\rm gas}$ and $\Sigma_{\rm SFR}$ relation of the starburst-dominated galaxies of the sample are shown in Figure 4.12 together with other galaxy populations, local normal spiral galaxies (Kennicutt, 1998b), high-z star-forming galaxies, submillimeter galaxies (Genzel et al., 2010) and local LIRGs/ULIRGs (Kennicutt, 1998b).

These populations are divided into two sequences of the starburst and the disk star-forming modes (Komugi et al., 2005; Daddi et al., 2010a; Genzel et al., 2010). The merging LIRGs show $\Sigma_{\rm SFR}$ higher by more than 1 dex compared to the spiral galaxies, although the $\Sigma_{\rm gas}$ is only $\sim$ 0.5 dex higher. This jump in $\Sigma_{\rm SFR}$ may result from the enhanced starburst in mergers. Komugi et al. (2006) find a threshold $\Sigma_{\rm gas}$ for the transition from star formation due to the spontaneous gravitational instability to the cloud-cloud collision-induced star formation at $\log \Sigma_{\rm gas}^{\rm crit}[M_\odot\,{\rm pc}^{-2}] \sim 1.8 - 2.9$. The $\Sigma_{\rm gas}$ jump of the LIRGs may be associated with the transition of the dominant star formation process, although the found $\Sigma_{\rm gas}^{\rm crit}$ is slightly higher than the $\Sigma_{\rm gas}$ of the LIRGs.

All merging LIRGs from the pre-merger stage (stage 1) to the late stage (stage 4) are located on the same region on the starburst sequence (see also Figure 4.4 and 4.9). The ULIRGs have the same SFE as starburst-dominated LIRGs, but occupy much higher $\Sigma_{\rm SFR}$ and $\Sigma_{\rm gas}$ region on the starburst sequence. These ULIRGs are observed to be the final stage mergers.

In order to explain the connection between these populations on the KS diagram, a theoretical prediction for a merger between two gas-rich galaxies (Teyssier et al., 2010) is also shown in Figure 4.12 by the large circles. Teyssier et al. (2010) demonstrate enhanced SFR and gas density of mergers and show the evolution along the merger sequence on the KS law. The pre-merger before the first pericentric passage is near the normal spirals on the disk star-forming sequence. After the first passage the on-going merger jumps to the starburst sequence, whose $\Sigma_{\rm SFR}$ and $\Sigma_{\rm gas}$ are comparable to the LIRGs. At the maximum SFR phase, both of the $\Sigma_{\rm SFR}$ and $\Sigma_{\rm gas}$ are temporarily enhanced more than one order of magnitude. Finally, the merger returns to the region between the spirals and the LIRGs. Because the on-going merger of the simulation evolves along the starburst sequence, the simulation implies unchanged SFE during the merger. The galaxies at the pre and post maximum SFR phase are not distinguished distinctly on the $\Sigma_{\rm SFR}$–$\Sigma_{\rm gas}$ relation. The locations on the KS law of the non-interacting spiral galaxies, our merging LIRGs and the ULIRGs of Kennicutt (1998b) are surprisingly consistent with the evolution of the mergers in the simulation. This describes an evolutionary sequence of gas-rich mergers that are observed as gas-rich spirals rapidly evolve towards local merging LIRGs, and then mergers spend as LIRGs for most of the life time, then at the late stage a temporary evolution from LIRGs to ULIRGs accompanies the ultra-luminous starburst, and finally the ULIRGs return to LIRGs.

4.6 Summary of Chapter 4

In this chapter, the star formation of merging LIRGs was discussed. Using CO data of our survey and 24 μm photometry, the SFR and SFE are examined along the merger sequence.

The spatial extent of the MIR dust continuum are taken from the literature which uses the Spitzer/IRS spectrogram and are also measured for some sources from the MIPS/IRAC 8 μm images. The MIR extents are confirmed to be smaller

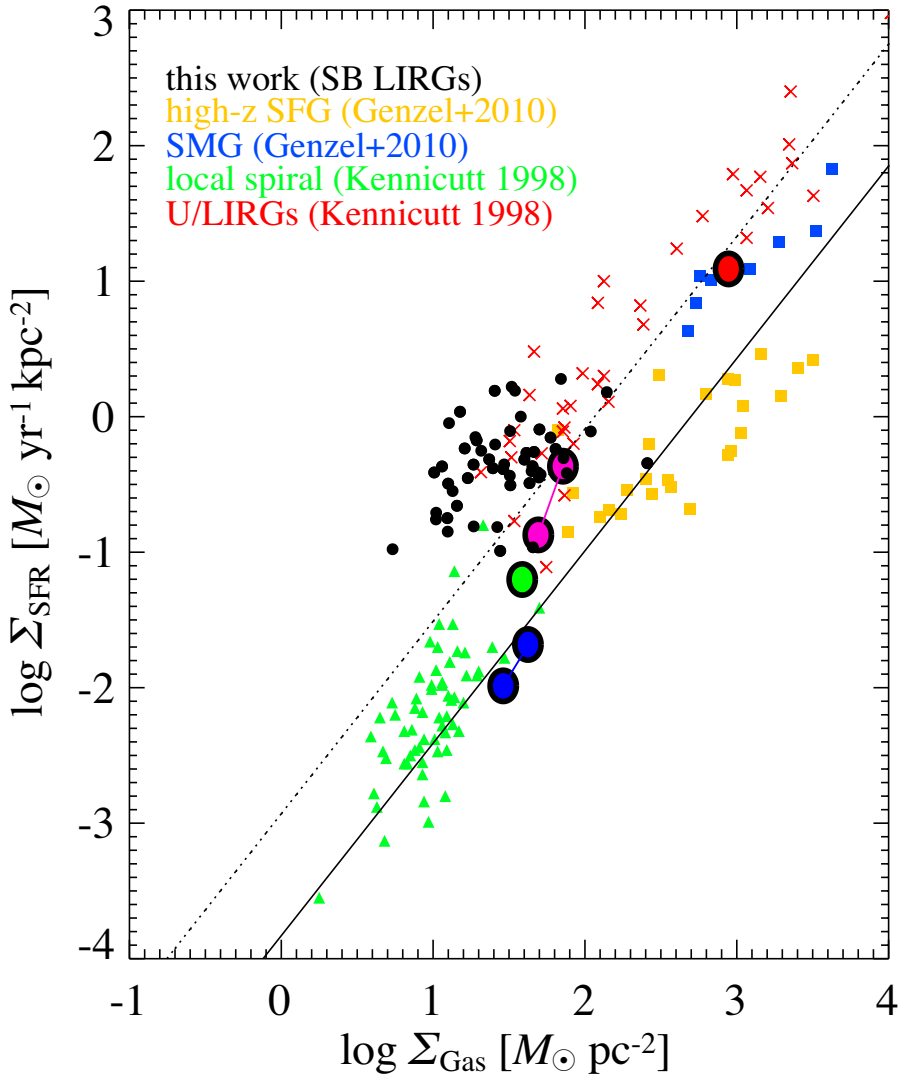

FIGURE 4.12: The SFR density and the gas surface density for various galaxy populations and of the merging LIRGs in our sample (black circle). The populations are taken from Genzel et al. (2010) for the high-z star-forming galaxies (yellow square) and the SMG (blue square) and Kennicutt (1998b) for the local spiral galaxies (green triangle) and the local LIRGs and ULIRGs (red cross). The solid and broken lines represent the two sequence of star formation, the normal disk mode and the starburst mode (Daddi et al., 2010a). The predicted surface density of the gas and the star formation rate density of two gas-rich mergers are overploted by large circles (Teyssier et al., 2010). The colors indicate the merger age and corresponds to pre-merger (blue), early stage merger (magenta), late stage merger (red) and remnant (green).

than the CO beam for all sample sources. The SFR is derived from the 24 μm photometry. The AGN contributions to MIR luminosities are estimated for non-starburst-dominated galaxies using MIR [NeV]/[NeII] emission line ratios, and the SFRs are corrected. The SFR ranges from 1.6 $M_{\odot}\mathrm{yr}^{-1}$ to 238 $M_{\odot}\mathrm{yr}^{-1}$, the median value is 22 $M_{\odot}\mathrm{yr}^{-1}$ and the average is 32 $M_{\odot}\mathrm{yr}^{-1}$ for the LIRGs. Combining the SFR and $M_{\mathrm{H_2}}$, the SFE and the the molecular gas depletion timescale are derived, which show $1.8 - 72 \times 10^{-9}\mathrm{yr}^{-1}$ and 14–570 Myr, respectively. This high SFE is comparable to the starburst sequence on the KS law.

Along the merger sequence, the median values of the SFR and $M_{\mathrm{H_2}}$ of U/LIRGs are found to be nearly constant. The high SFR in all the stages is likely due to a sample-selection rather than a continuous starburst. The merging LIRGs are likely galaxies in a luminous starburst at each merger stage. The LIRGs are coexistent with ULIRGs at the late stage, and have lower SFR than ULIRGs. This suggests that the LIRGs at the late stage are galaxies prior to ULIRGs (pre-ultraluminous starburst) or or immediately after experiencing the short ULIRGs phase (post-ultraluminous starburst). The SFE of the merging LIRGs is constant throughout all the merger stages. This constancy of SFE implies that the conversion from gas to stars is driven by a common relation regardless of the merger stage. The constant star formation timescale represented by either the free-fall timescale or the cloud-cloud collision timescale may be maintained during the luminous starburst phase of mergers and therefore produce the constant SFE. On the KS diagram, the merging LIRGs are located between the normal spiral galaxies and local ULIRGs. This may suggest an evolutionary sequence from the gas-rich spirals, LIRGs to ULIRGs and again back to LIRGs.

Chapter 5

Summary and Conclusion

5.1 Summary of This Thesis

This thesis presents the results of a new and the largest CO survey of local LIRGs to date, investigating the variation of molecular gas and star formation along the merger sequence. Here the thesis is summarized.

- In order to understand star formation associated with the starburst in the local LIRGs, the molecular gas mass in the central several kpc were obtained from the CO observation of the 76 galaxies in 62 local LIRGs using the Nobeyama 45 m telescope. The target sample consists of the northern subsample of the GOALS LIRGs, and the properties are similar to the parent GOALS LIRGs, covering the full ranges of the IR luminosity, the merger stage and the AGN activity. The CO emission was detected in 68 galaxies, giving a detection rate of 86 %. The molecular gas mass is estimated to be $2.2 \times 10^8 - 7.0 \times 10^9\,M_\odot$, adopting an $\alpha_{\rm CO}$ of $0.6\,M_\odot(\mathrm{K\,km\,s^{-1}\,pc^{-2}})^{-1}$. (Chapter 1 & 2)

- I present a new method to estimate the extent of the CO distribution using single-dish observations with two different beam-sizes. The estimated CO size are consistent with interferometric measurements for most of the sources with available interferometric data. The majority of the galaxies have CO radii of $\lesssim 4$ kpc. (Chapter 3)

- In LIRGs, the median values of the molecular gas mass in the central region are constant from the early stage to the late stage of merger. The CO size decreases from the early stage to the late stage of merger by a factor of $\geqq 2$. This statistically supports a scenario where the global gas inflows into the central region to replenish the molecular gas consumed by the starbursts. The inflowing gas may come from the outer disk towards the central region. The time-averaged inflow rate is roughly estimated to be $O(10)\,M_\odot\mathrm{yr}^{-1}$, which is significantly larger than the inflow rate in barred spiral galaxies. (Chapter 3)

- Along the merger sequence, the median values of the SFR and $M_{\rm H_2}$ of the merging LIRGs are found to be nearly constant, suggesting that the merging LIRGs are sources found around short and peaky luminous starburst phases. The LIRGs are coexistent with ULIRGs at the late stage, and have lower SFR than ULIRGs. Considering merger simulations which predict the peaky

starbursts and the steep rise up to and decline from ULIRG phase in SFR predicted by merger simulations, this suggests that the LIRGs at the late stage are galaxies prior to or immediately after the short ULIRG phase. (Chapter 4)

- The SFE and the molecular gas depletion timescale are $1.8 - 72 \times 10^{-9}\mathrm{yr}^{-1}$ and 14–570 Myr, respectively. This high SFE is comparable to the starburst sequence on the KS law. Throughout all the merger stages, the SFE of the merging LIRGs is also constant, implying the conversion from gas to stars is driven by a common relation regardless of the merger stage. The constant timescale of the free-fall or the cloud-cloud collision may be maintained during the luminous starburst phase of mergers and therefore produce the constant SFE. On KS law, the merging LIRGs are located between the normal spiral galaxies and local ULIRGs. This may suggest the evolutionary sequence from the gas-rich spirals, LIRGs to ULIRGs and again back to LIRGs. (Chapter 4)

5.2 Future Prospects

The study in this thesis is the first step to reveal the evolution of the star formation mechanism and the behavior of molecular gas in merging LIRGs. It is statistically shown that the global gas inflow is common in merging LIRGs. From the discussion of the star formation efficiency in the central regions at each merger stage, a hypothesis about the evolution of the merging LIRGs and the dominant process of the merger-driven star formation is proposed. There are additional studies and questions to prove in order to completely understand the issues raised in this thesis.

Global Gas Inflow: Observations of Total Molecular/Atomic Gas

It is shown that the molecular gas in the central several kpc region of merging LIRGs is constant along the merger sequence. This supports that the global gas inflow is common in merging LIRGs. This conclusion is based on the observational and theoretical facts that the merger-driven star formation decreases the total gas mass along the merger sequence while the global gas inflow increases the gas within

the central several region. Therefore my conclusion of the global gas inflow can be strengthened by a comparison of total molecular gas mass at each merger stage using our sample. With this view, observations with small-aperture telescopes (e.g., the Arizona Radio Observatory 12 m telescope) should be conductged to obtain the total molecular gas mass of our sample. This future observation also enables us to increase the sample size to estimate the CO size.

On the discussion about the increase and decrease of the gas in merging LIRGs, the neutral atomic gas (HI) is not included. In the central regions of local LIRGs, the HI column density is less than $1\,M_{\odot}\mathrm{pc}^{-2}$ (**?**), while the H_2 column density is 10–100 $M_{\odot}\mathrm{pc}^{-2}$ (see Figure 4.9 and 4.12). The atomic gas fraction in the central region is low enough to negligible. Thus, if the HI gas is considered in the discussion of the increase and decrease of gas in the central region, the conclusion is not affected. However, the atomic gas fraction whole a galaxy increases up to 50 % (**?**). When the total gas whole a galaxy is examined along the merger sequence, the atomic gas may not be negligible. The processes of the formation and dissociation between HI and H_2 gas during mergers should be considered. Therefore, the total atomic gas should be observed, as well as the total molecular gas.

Global Gas Inflow: Spatially Resolved Observation

The single-dish observations have advantages in survey speed and measurements of the total gas mass. Meanwhile, they cannot provide the spatially resolved information of the gas in galaxies. The long-baseline interferometers allow us to study the well resolved distributions of the molecular gas, the trigger of the starbursts and the star formation in mergers. The global gas inflows in mergers can be detected and quantified by direct imaging of the molecular gas. The merger-driven starburst can be studied well at the GMC scales. Recent and upcoming interferometric arrays such as the Atacama Large Millimeter/submillimeter Array (ALMA), the Square Kilometre Array (SKA) and the NOrthern Extended Millimeter Array (NOEMA) have the powerful potential to conduct a large survey of mergers with the high resolution and sensitivity.

Star Formation History of Mergers: Low-SFR Mergers

In this thesis we discussed the merger evolution and argued the pulse-like starburst on the merger sequence to explain the observational results showing always high SFR and SFE of merging LIRGs. To establish this scenario, we need to examine the SFR and the molecular gas of quiescent phase galaxies with lower SFR but along the same merger sequence as that studied in this thesis. Firstly, a sample composed of mergers with lower SFR comparable stellar mass and impact factor of collision to merging LIRGs must be established. Furthermore, an extended CO survey and a catalog search from UV to IR for the sample should be conducted. Then it will be examined whether the SFR and SFE of the lower-SFR sample coincide with the hypothesis which predicts that the quiescent phase mergers have lower SFR and SFE compared to starburst phase LIRGs.

Star Formation of Non-Mergers

This thesis focuses on merging LIRGs. However, interesting results are found in regard to non-mergers of stage-0. The galaxies that do not show any features of interactions/mergers in the optical images are classified as non-mergers. Therefore it is thought that the star formation of non-mergers are not influenced by interactions, although the IR radiation is as large as starbursting LIRGs involved with interactions. The mechanism of their high IR radiation is unclear. Of GOALS LIRGs, 20–40 % are belong to non-mergers (Stierwalt et al., 2013). Therefore, revealing the star formation in non-mergers is essential to totally understand the star formation of local LRIGs. Haan et al. (2011) show that non-mergers in the GOALS LIRGs have the most luminous bulge compared with other merger stages, and therefore argue that non-merger LIRGs are likely to be a consequence of a selection effect for more intrinsically luminous galaxies. Recently, **?** report that HI observations of non-merger LIRGs show extended features with morphologies and kinematics consistent with ongoing tidal interaction. This may suggest that non-mergers actually have experienced tidal perturbations which do not largely distort stellar morphologies.

Our study shows that non-mergers have the small CO size comparable to the late stage mergers, and the $M_{\mathrm{H_2}}$ and SFE are as high as merging LIRGs. The behavior of molecular gas in non-mergers is similar to the late stage mergers. In

further studies for non-merger LIRGs, the CO size, $M_{\mathrm{H_2}}$ and SFE will be compared with a sample of optically-selected normal spiral galaxies with comparable stellar mass and bulge mass to non-mergers. This comparison will judge whether the star formation of the non-merger LIRGs is enhanced compared to the normal spiral galaxies. If the enhancement of the star formation activity is not observed, the non-merger LIRGs may be the result of the selection effect, where the IR radiation may result from rich dust and abundant old stars. On the other hand, if the enhancements is observed, there may be a perturbator to induce the high star formation activity, e.g., minor mergers.

Acknowledgements

This thesis could not have been written without the supports from many people. I would like to thank all of them. First and foremost, I would like to express my deepest gratitude to my supervisor, Hideo Matsuhara for giving me the opportunity to work on this study and his continuous encouragement. He gave me a lot of invaluable experiences and precious advice about both this study and the direction of my research. I am deeply grateful to Shinya Komugi for the fruitful discussion and supports since this study started. I learned a lot of things from him: the technique of radio observations, the way to research, writing, and the posture as an astronomer. This work would not have been possible without his support.

I would like to thank the GOALS CO members, Lee Armus, Hanae Inami, Daisuke Iono, Junko Ueda, Ko Arimatsu, Kotaro Kohno, Sabrina Stierwalt and Aaron Evans. I would like to thank the LIRA members, Takao Nakagawa, Yamamura Issei, Mitsunobu Kawada, Norio Ikeda, Fumi Egusa, Nagisa Oi, Satoshi Takita, Yoshiki Toba, Toshiaki Arai, Satoko Sorahana, Kanae Haze, Kazumi Murata, Ken'ichi Yano, Shuhei Koyama and Hitomi Kimura. I am greatly thankful to Satoru Iguchi, Ken'ichi Tatematu, Daisuke Iono, Toshiki Saito, Kyoko Onishi, Satoshi Ohashi, Kazuhiro Kiyokane, Yuta Kato, Minju Lee, Tomonari Michiyama, Takuya Kurahashi and the staff and students at the ALMA Building at Mitaka.

I would like to thank the staff at Nobeyama Radio Observatory for their support on our observations. Nobeyama Radio Observatory is a branch of the National Astronomical Observatory of Japan, National Institutes of Natural Sciences. I acknowledges the financial support from the Global Center of Excellence Program by MEXT, Japan through the "Nanoscience and Quantum Physics" Project of the Tokyo Institute of Technology. This research has made use of the NASA/IPAC Extragalactic Database (NED) and the Infrared Science Archive (IRSA) which are operated by the Jet Propulsion Laboratory, California Institute of Technology, under contract with the National Aeronautics and Space Administration. Data analysis were in part carried out on common use data analysis computer system at the Astronomy Data Center, ADC, of the National Astronomical Observatory of Japan.

最後に、これまで私の長い学生生活をあらゆる面で支えてくださいました父、山下正信、母、山下ひとみに心より感謝を申し上げます。また、私の研究生活をどのような時も暖かく支え、応援してくださいました佐藤文美さんに心から感謝します。

Appendix A

Notes on Notable Sources

We describe here the characteristics of four sources which have excessively large or small flux ratio ($R_{\rm CO} \gtrsim 1.9$ or $R_{\rm CO} \lesssim 0.2$), and one source which may have CO intensity distributions that possibly deviate from our assumed models.

NGC 1275

This object is a cD galaxy at the center of the Perseus cluster. A Strong radio continuum comes from Perseus A (3C 084) located in the center of NGC 1275. The cold molecular gas is associated with filament structures seen in Hα (Salomé et al., 2006, 2008b,a). The NRO45 observation of the 15″ beam shows that this source has 98.2 Jy km s^{-1}, which is 75 % larger than 35.7 Jy km s^{-1} given in Young et al. (1995) by the 45″ beam, and therefore has a high $R_{\rm CO}$ of 2.75 (see Section 2.4). The flux towards the center of NGC 1275 measured in other studies differ much. Lazareff et al. (1989) reported a flux of 123 ± 4 Jy km s^{-1} with the 21″ beam at IRAM 30 m. Mirabel et al. (1989) obtained a flux of 65.8 Jy km s^{-1} with the the 55″ beam at NRAO 12 m, and Evans et al. (2005) measured the flux to be 104 ± 1 Jy km s^{-1} with 55″ beam at the Kitt Peak 12 m Telescope. An observation by Salomé et al. (2008a) reported the central flux of NGC 1275 to be 26.7 ± 5.8 Jy km s^{-1} with IRAM 30 m. This undetermined flux may be due to instabilities of the baseline in the spectra due to the strong radio continuum.

We note that $\Delta V_{\rm FWHM}$ we measure may be overestimated because of the low S/N ratio. In the velocity range with the high S/N ratio the $\Delta V_{\rm FWHM}$ is estimated to be 240 km s^{-1}. Lazareff et al. (1989), Mirabel et al. (1989), Evans et al. (2005) and Salomé et al. (2008a) estimate $\Delta V_{\rm FWHM}$ to be 200 – 300 km s^{-1}.

UGC 05101

This ULIRG shows a high flux ratio of $R_{\rm CO} = 1.87$. The flux is $141.4 \pm 9.7\,{\rm Jy\,km\,s^{-1}}$ based on the NRO45 observation, while $75.5\,{\rm Jy\,km\,s^{-1}}$ based on the IRAM 30 m observation (Gao & Solomon, 2004a). Solomon et al. (1997) obtained $77.2\,{\rm Jy\,km\,s^{-1}}$ with the IRAM 30 m. The velocity widths of Gao & Solomon (2004a) and Solomon et al. (1997), which are located in the heliocentric velocity range from $11500\,{\rm km\,s^{-1}}$ to $12000\,{\rm km\,s^{-1}}$, are consistent with each other, as well as the flux. Our spectrum presented here shows an additional redshifted component $+500$ ${\rm km\,s^{-1}}$ and consequently the broad velocity width of $840\,{\rm km\,s^{-1}}$. Due to this redshifted feature, our measurement of the flux is larger than those by Gao & Solomon (2004a) and Solomon et al. (1997). Thus the higher $R_{\rm CO}$ than 1 is likely due to the low S/N ratio in our measurement.

Mrk 231

For this ULIRG, the flux measurements by NRO45 and SSS91 show $110.8 \pm 5.0\,{\rm Jy\,km\,s^{-1}}$ and $56.0\,{\rm Jy\,km\,s^{-1}}$, respectively. Therefore Mrk 231 has a high flux ratio of 1.98. Our measurement is consistent with the IRAM 30 m observation with $22''$ beam, which give $S_{\rm CO}\Delta V = 109\,{\rm Jy\,km\,s^{-1}}$ (Solomon et al., 1997). Additionally the CO spectrum by SSS91 shows two peaks, while the spectrum of our observation and Solomon et al. (1997) show a single peak. Thus the measurement by SSS91 may be doubtful. The S/N ratio of the observation by SSS91 appear to be lower compared to our observation and the observation by Solomon et al. (1997).

MCG+04-48-002S (NGC 6921, MCG +04-48-001)

This is a less-IR luminous object ($L_{\rm IR} = 10^{10.68}\,L_\odot$), accompanying a luminous companion galaxy MCG +04-48-002N (MCG +04-48-002, $L_{\rm IR} = 10^{11.06}\,L_\odot$) offset on the sky by $1.5'$. Our flux measurement shows $37.1 \pm 5.8\,{\rm Jy\,km\,s^{-1}}$. GS04 obtain a flux of $188\,{\rm Jy\,km\,s^{-1}}$ with a $22''$ beam observation. Thus a flux ratio $R_{\rm CO}$ is as low as 0.2. Young et al. (1986b, 1995) reported a larger flux of $312\,{\rm Jy\,km\,s^{-1}}$. Both observations of GS04 and Young et al. (1986b, 1995), however, suffer from baseline uncertainties due to relatively narrow bandwidths. Moreover, the line profiles are quite different between GS04 and Young et al. (1986b). The flux from GS04 is consistent with a flux estimated from the $M_{\rm H_2}$ – $L_{\rm IR}$ relation for the starburst galaxies in Daddi et al. (2010a).

NGC 7771S1

This object is an edge-on galaxy companying two galaxies NGC 7771N (NGC 7769) and NGC 7771S2 (NGC 7770). The 24 μm peak is located at the galactic center, while the two additional components of 24 μm are seen at both edges of the galaxy (see Figure 2.5). Interferometric observation of the galaxy shows an elongated CO distribution towards the east edge (Dale et al., 2005). Therefore the CO spatial structure might not match any of models to estimate the CO extent in Section 3.3.2.

The line profile has showing three distinct peaks (see Figure 2.5). This three-peak profile is also seen in the 14 m observation (SSS91; Young et al. 1995). The confirmation by the smaller 15″ beam observation indicates that the origin of the profile is within the central 2.2 kpc. There may be a rotating molecular ring around the galactic nucleus, producing the secondary peaks and concentrated molecular clouds which emerge as the central peak in the spectrum. The rotating molecular ring might be directly associated with the starburst ring existing around the nucleus (Smith et al., 1999).

Mrk 331

This object is a disk galaxy at the pre-merger stage (Haan et al. 2011; ST13). The CO we obtain shows a much lower flux $45.0 \pm 8.8\,\mathrm{Jy\,km\,s^{-1}}$ than the 12 m observation $346.4\,\mathrm{Jy\,km\,s^{-1}}$ (GS04). The flux ratio 0.13 is the lowest in our sample. Other flux measurements of Mrk 331 report $371\,\mathrm{Jy\,km\,s^{-1}}$ with the IRAM 30 m (Solomon et al., 1997) and $392\,\mathrm{Jy\,km\,s^{-1}}$ with the FCRAO 14 m (Young et al., 1995). The flux of our measurements may be underestimated likely due to the uncertainty of the baseline.

Appendix B

Rotational Transition of CO Molecule

The kinetic energy of rotation of a molecule is represented as,

$$H_{\text{rot}} = \frac{1}{2} I\omega^2 = \frac{\boldsymbol{L}^2}{2\Theta}, \tag{B.1}$$

where I is the moment of inertia of the molecule, ω is the angular frequency of the rotation, and $\boldsymbol{L}$ is the angular momentum. For a rigid diatomic molecule, the moment of inertia is

$$I = \mu r^2 \tag{B.2}$$

where μ is the reduced mass and r is the effective radius of the molecule, and the angular momentum is

$$\boldsymbol{L} = I\boldsymbol{\omega}. \tag{B.3}$$

The angular momentum is perpendicular to the axis connecting the two nuclei.

From the solution of the Schrödinger equation, this eigenvalue for the rotational energy is

$$E_J = \frac{\hbar^2}{2I} J(J+1) = hBJ(J+1) \tag{B.4}$$

where B is the rotational constant

$$B = \frac{\hbar}{4\pi I} \tag{B.5}$$

and J is the quantum number of angular momentum, which has

$$J = 0, 1, 2, ... \tag{B.6}$$

When the diatomic molecule emits the light, the electric dipole-allowed radiation is dominant. In this case, the allowed transitions are

$$\Delta J = \pm 1. \tag{B.7}$$

The frequency of the transition $J + 1 \rightarrow J$ is

$$\nu_{J+1 \rightarrow J} = \frac{E_{J+1} - E_J}{h} = 2B(J + 1). \tag{B.8}$$

The rotational constant B depends on molecules. Typically, B of molecules has approximately 10–100 GHz and therefore the frequencies of the rotational transitions of molecules are located at the wavelength ranges of centimeter/millimeter/submillimeter. These frequencies are several orders of magnitude lower than the electric transitions, because the effective radius of a molecule is 10^5 times larger compared with the radius of an atomic nucleus, and thus the moment of the inertia is 10^{10} times larger than an atom with the same mass. In case of the $J = 1 \rightarrow 0$ transition of $^{12}C^{16}O$ molecule, B is determined to be 57.6 GHz (Gilliam et al., 1950), and thus $\nu_{1 \rightarrow 0}$ is 115 GHz.

Bibliography

Aalto, S., & Hüttemeister, S. 2000, A&A, 362, 42

Alonso-Herrero, A., Pereira-Santaella, M., Rieke, G. H., & Rigopoulou, D. 2012a, ApJ, 744, 2

Alonso-Herrero, A., Rieke, G. H., Rieke, M. J., et al. 2006, ApJ, 650, 835

Alonso-Herrero, A., Rosales-Ortega, F. F., Sánchez, S. F., et al. 2012b, MNRAS, 425, L46

Armus, L., Charmandaris, V., Bernard-Salas, J., et al. 2007, ApJ, 656, 148

Armus, L., Mazzarella, J. M., Evans, A. S., et al. 2009, PASP, 121, 559

Barnes, J. E., & Hernquist, L. 1996, ApJ, 471, 115

Bolatto, A. D., Wolfire, M., & Leroy, A. K. 2013, ARA&A, 51, 207

Brandl, B. R., Bernard-Salas, J., Spoon, H. W. W., et al. 2006, ¥apj, 653, 1129

Bryant, P. M., & Scoville, N. Z. 1999, AJ, 117, 2632

Casey, C. M. 2012, MNRAS, 425, 3094

Cazzoli, S., Arribas, S., Colina, L., et al. 2014, A&A, 569, A14

Cicone, C., Maiolino, R., Sturm, E., et al. 2014, A&A, 562, A21

Costagliola, F., Aalto, S., Sakamoto, K., et al. 2013, A&A, 556, A66

Cox, T. J., Jonsson, P., Primack, J. R., & Somerville, R. S. 2006, MNRAS, 373, 1013

Cox, T. J., Jonsson, P., Somerville, R. S., Primack, J. R., & Dekel, A. 2008, MNRAS, 384, 386

Curran, S. J., Aalto, S., & Booth, R. S. 2000, A&AS, 141, 193

Daddi, E., Cimatti, A., Renzini, A., et al. 2004, ApJ, 617, 746

Daddi, E., Dannerbauer, H., Elbaz, D., et al. 2008, ApJ, 673, L21

Daddi, E., Elbaz, D., Walter, F., et al. 2010a, ApJ, 714, L118

Daddi, E., Bournaud, F., Walter, F., et al. 2010b, ApJ, 713, 686

Dale, D. A., Sheth, K., Helou, G., Regan, M. W., & Hüttemeister, S. 2005, AJ, 129, 2197

Dame, T. M., Hartmann, D., & Thaddeus, P. 2001, ApJ, 547, 792

Desai, V., Armus, L., Spoon, H. W. W., et al. 2007, ApJ, 669, 810

Di Matteo, P., Combes, F., Melchior, A.-L., & Semelin, B. 2007, A&A, 468, 61

Díaz-Santos, T., Charmandaris, V., Armus, L., et al. 2010, ApJ, 723, 993

—. 2011, ApJ, 741, 32

Díaz-Santos, T., Armus, L., Charmandaris, V., et al. 2013, ApJ, 774, 68

Dickman, R. L., Snell, R. L., & Schloerb, F. P. 1986, ApJ, 309, 326

Dinh-V-Trung, ., Lo, K. Y., Kim, D.-C., Gao, Y., & Gruendl, R. A. 2001, ApJ, 556, 141

Dopita, M. A., Pereira, M., Kewley, L. J., & Capaccioli, M. 2002, ApJS, 143, 47

Downes, D., & Solomon, P. M. 1998, ApJ, 507, 615

Downes, D., Solomon, P. M., & Radford, S. J. E. 1993, ApJ, 414, L13

Draine, B. T. 2003, ARA&A, 41, 241

Elfhag, T., Booth, R. S., Hoeglund, B., Johansson, L. E. B., & Sandqvist, A. 1996, A&AS, 115, 439

Evans, A. S., Mazzarella, J. M., Surace, J. A., et al. 2005, ApJS, 159, 197

Fukui, Y., Ohama, A., Hanaoka, N., et al. 2014, ApJ, 780, 36

Furukawa, N., Dawson, J. R., Ohama, A., et al. 2009, ApJ, 696, L115

Gao, Y., & Solomon, P. M. 1999, ApJ, 512, L99

—. 2004a, ApJS, 152, 63

—. 2004b, ApJ, 606, 271

García-Burillo, S., Usero, A., Alonso-Herrero, A., et al. 2012, A&A, 539, A8

García-Burillo, S., Combes, F., Usero, A., et al. 2014, A&A, 567, A125

Gehrz, R. D., Roellig, T. L., Werner, M. W., et al. 2007, Review of Scientific Instruments, 78, 011302

Genzel, R., Tacconi, L. J., Gracia-Carpio, J., et al. 2010, MNRAS, 407, 2091

Genzel, R., Tacconi, L. J., Combes, F., et al. 2012, ApJ, 746, 69

Gilliam, O. R., Johnson, C. M., & Gordy, W. 1950, Phys. Rev., 78, 140

Glover, S. C. O., & Mac Low, M.-M. 2011, MNRAS, 412, 337

Goldsmith, P. F., Heyer, M., Narayanan, G., et al. 2008, ApJ, 680, 428

Haan, S., Surace, J. A., Armus, L., et al. 2011, AJ, 141, 100

Haan, S., Armus, L., Surace, J. A., et al. 2013, MNRAS, 434, 1264

Ho, L. C. 2008, ARA&A, 46, 475

Howell, J. H., Armus, L., Mazzarella, J. M., et al. 2010, ApJ, 715, 572

Inami, H., Armus, L., Surace, J. A., et al. 2010, AJ, 140, 63

Inami, H., Armus, L., Charmandaris, V., et al. 2013, ApJ, 777, 156

Iono, D., Yun, M. S., & Ho, P. T. P. 2005, ApJS, 158, 1

Iono, D., Yun, M. S., & Mihos, J. C. 2004, ApJ, 616, 199

Iono, D., Saito, T., Yun, M. S., et al. 2013, PASJ, 65, L7

Israel, F. P., Tilanus, R. P. J., & Baas, F. 2006, A&A, 445, 907

Iwasawa, K., Sanders, D. B., Evans, A. S., et al. 2009, ApJ, 695, L103

Iwasawa, K., Sanders, D. B., Teng, S. H., et al. 2011, A&A, 529, A106

Kamazaki, T., Okumura, S. K., Chikada, Y., et al. 2012, PASJ, 64, 29

Kapferer, W., Knapp, A., Schindler, S., Kimeswenger, S., & van Kampen, E. 2005, A&A, 438, 87

Kaviraj, S., Cohen, S., Windhorst, R. A., et al. 2013, MNRAS, 429, L40

Kennicutt, Jr., R. C. 1998a, ARA&A, 36, 189

—. 1998b, ApJ, 498, 541

Kim, D.-C., Evans, A. S., Vavilkin, T., et al. 2013, ApJ, 768, 102

Komugi, S., Sofue, Y., & Egusa, F. 2006, PASJ, 58, 793

Komugi, S., Sofue, Y., Nakanishi, H., Onodera, S., & Egusa, F. 2005, PASJ, 57, 733

Lacey, C., & Cole, S. 1993, MNRAS, 262, 627

Larson, R. B. 1981, MNRAS, 194, 809

Lazareff, B., Castets, A., Kim, D.-W., & Jura, M. 1989, ApJ, 336, L13

Leroy, A. K., Evans, A. S., Momjian, E., et al. 2011, ApJ, 739, L25

Lotz, J. M., Jonsson, P., Cox, T. J., & Primack, J. R. 2010a, MNRAS, 404, 590

—. 2010b, MNRAS, 404, 575

Magnelli, B., Saintonge, A., Lutz, D., et al. 2012, A&A, 548, A22

Mazzarella, J. M., Graham, J. R., Sanders, D. B., & Djorgovski, S. 1993, ApJ, 409, 170

Medling, A. M., U, V., Guedes, J., et al. 2014, ApJ, 784, 70

Mihos, J. C., & Hernquist, L. 1994, ApJ, 431, L9

—. 1996, ApJ, 464, 641

Mirabel, I. F., Booth, R. S., Johansson, L. E. B., Garay, G., & Sanders, D. B. 1990, A&A, 236, 327

Mirabel, I. F., Sanders, D. B., & Kazes, I. 1989, ApJ, 340, L9

Murakami, H., Baba, H., Barthel, P., et al. 2007, PASJ, 59, 369

Murphy, Jr., T. W., Soifer, B. T., Matthews, K., & Armus, L. 2001, ApJ, 559, 201

Nakajima, T., Sakai, T., Asayama, S., et al. 2008, PASJ, 60, 435

Nakajima, T., Kimura, K., Nishimura, A., et al. 2013, PASP, 125, 252

Nakanishi, H. 2005, PhD thesis, The University of Tokyo, Tokyo, Japan

Nakanishi, H., & Sofue, Y. 2006, PASJ, 58, 847

Narayanan, D., Krumholz, M., Ostriker, E. C., & Hernquist, L. 2011, MNRAS, 418, 664

Neugebauer, G., Habing, H. J., van Duinen, R., et al. 1984, ApJ, 278, L1

Nishiyama, K., & Nakai, N. 2001, PASJ, 53, 713

Nishiyama, K., Nakai, N., & Kuno, N. 2001, PASJ, 53, 757

Ownsworth, J. R., Conselice, C. J., Mortlock, A., et al. 2014, MNRAS, 445, 2198

Papadopoulos, P. P., van der Werf, P., Xilouris, E., Isaak, K. G., & Gao, Y. 2012, ApJ, 751, 10

Petric, A. O., Armus, L., Howell, J., et al. 2011, ApJ, 730, 28

Pilbratt, G. L., Riedinger, J. R., Passvogel, T., et al. 2010, A&A, 518, L1

Pineda, J. E., Caselli, P., & Goodman, A. A. 2008, ApJ, 679, 481

Planesas, P., Mirabel, I. F., & Sanders, D. B. 1991, ApJ, 370, 172

Privon, G. C., Barnes, J. E., Evans, A. S., et al. 2013, ApJ, 771, 120

Saintonge, A., Kauffmann, G., Kramer, C., et al. 2011, MNRAS, 415, 32

Saitoh, T. R., Daisaka, H., Kokubo, E., et al. 2009, PASJ, 61, 481

Sakamoto, K., Aalto, S., Combes, F., Evans, A., & Peck, A. 2014, ArXiv e-prints

Sakamoto, K., Okumura, S. K., Ishizuki, S., & Scoville, N. Z. 1999, ApJ, 525, 691

Salomé, P., Combes, F., Revaz, Y., et al. 2008a, A&A, 484, 317

Salomé, P., Revaz, Y., Combes, F., et al. 2008b, A&A, 483, 793

Salomé, P., Combes, F., Edge, A. C., et al. 2006, A&A, 454, 437

Salpeter, E. E. 1955, ApJ, 121, 161

Sanders, D. B., Mazzarella, J. M., Kim, D.-C., Surace, J. A., & Soifer, B. T. 2003, AJ, 126, 1607

Sanders, D. B., & Mirabel, I. F. 1985, ApJ, 298, L31

—. 1996, ARA&A, 34, 749

Sanders, D. B., Scoville, N. Z., & Soifer, B. T. 1991, ApJ, 370, 158

Sanders, D. B., Scoville, N. Z., Young, J. S., et al. 1986, ApJ, 305, L45

Sanders, D. B., Solomon, P. M., & Scoville, N. Z. 1984, ApJ, 276, 182

Scoville, N. Z., Sanders, D. B., Sargent, A. I., Soifer, B. T., & Tinney, C. G. 1989, ApJ, 345, L25

Scoville, N. Z., Sargent, A. I., Sanders, D. B., & Soifer, B. T. 1991, ApJ, 366, L5

Scoville, N. Z., Yun, M. S., Sanders, D. B., Clemens, D. P., & Waller, W. H. 1987, ApJS, 63, 821

Silk, J. 1997, ApJ, 481, 703

Skrutskie, M. F., Cutri, R. M., Stiening, R., et al. 2006, AJ, 131, 1163

Smith, D. A., Herter, T., Haynes, M. P., & Neff, S. G. 1999, ApJ, 510, 669

Soifer, B. T., Neugebauer, G., Matthews, K., et al. 2000, AJ, 119, 509

—. 2001, AJ, 122, 1213

Solomon, P. M., Downes, D., Radford, S. J. E., & Barrett, J. W. 1997, ApJ, 478, 144

Solomon, P. M., Rivolo, A. R., Barrett, J., & Yahil, A. 1987, ApJ, 319, 730

Solomon, P. M., & Vanden Bout, P. A. 2005, ARA&A, 43, 677
Stierwalt, S., Armus, L., Surace, J. A., et al. 2013, ApJS, 206, 1
Stierwalt, S., Armus, L., Charmandaris, V., et al. 2014, ApJ, 790, 124
Strong, A. W., & Mattox, J. R. 1996, A&A, 308, L21
Sturm, E., Lutz, D., Tran, D., et al. 2000, A&A, 358, 481
Surace, J. A. 1998, PhD thesis, Institute for Astronomy University of Hawaii 2680 Woodlawn Dr. Honolulu, HI 96822
Tacconi, L. J., Genzel, R., Smail, I., et al. 2008, ApJ, 680, 246
Taylor, C. L., Hüttemeister, S., Klein, U., & Greve, A. 1999, A&A, 349, 424
Teyssier, R., Chapon, D., & Bournaud, F. 2010, ApJ, 720, L149
Tinney, C. G., Scoville, N. Z., Sanders, D. B., & Soifer, B. T. 1990, ApJ, 362, 473
Torii, K., Enokiya, R., Sano, H., et al. 2011, ApJ, 738, 46
U, V., Sanders, D. B., Mazzarella, J. M., et al. 2012, ApJS, 203, 9
Ueda, J., Iono, D., Yun, M. S., et al. 2014, ApJS, 214, 1
Vardoulaki, E., Charmandaris, V., Murphy, E. J., et al. 2014, ArXiv e-prints
Veilleux, S., Kim, D.-C., Sanders, D. B., Mazzarella, J. M., & Soifer, B. T. 1995, ApJS, 98, 171
Veilleux, S., Rupke, D. S. N., Kim, D.-C., et al. 2009, ApJS, 182, 628
Walter, F., Weiss, A., & Scoville, N. 2002, ApJ, 580, L21
Wilson, C. D., & Matthews, B. C. 1995, ApJ, 455, 125
Wilson, C. D., Warren, B. E., Irwin, J., et al. 2011, MNRAS, 410, 1409
Wolfire, M. G., Hollenbach, D., & McKee, C. F. 2010, ApJ, 716, 1191
Xu, C. K., Cao, C., Lu, N., et al. 2014, ApJ, 787, 48
—. 2015, ApJ, 799, 11
Yao, L., Seaquist, E. R., Kuno, N., & Dunne, L. 2003, ApJ, 588, 771
Young, J. S., Kenney, J., Lord, S. D., & Schloerb, F. P. 1984, ApJ, 287, L65
Young, J. S., Kenney, J. D., Tacconi, L., et al. 1986a, ApJ, 311, L17
Young, J. S., Schloerb, F. P., Kenney, J. D., & Lord, S. D. 1986b, ApJ, 304, 443
Young, J. S., & Scoville, N. 1982, ApJ, 258, 467
Young, J. S., & Scoville, N. Z. 1991, ARA&A, 29, 581
Young, J. S., Xie, S., Kenney, J. D. P., & Rice, W. L. 1989, ApJS, 70, 699
Young, J. S., Xie, S., Tacconi, L., et al. 1995, ApJS, 98, 219
Yuan, T.-T., Kewley, L. J., & Sanders, D. B. 2010, ApJ, 709, 884
Yun, M. S., & Scoville, N. Z. 1995, ApJ, 451, L45
Yun, M. S., Scoville, N. Z., & Knop, R. A. 1994, ApJ, 430, L109
Zhao, Y., Lu, N., Xu, C. K., et al. 2013, ApJ, 765, L13